

Dissertation
submitted to the
Combined Faculty of Natural Sciences and Mathematics
of the Ruperto Carola University Heidelberg, Germany
for the degree of
Doctor of Natural Sciences

Presented by

Fabian Merkel, M. Sc.

born in Schweinfurt

Oral examination: 17.12.2020

Structure of the condensin holo complex

Referees: Prof. Dr. Sylvia Erhardt

Dr. Alba Diz-Muñoz

All major results from this thesis are published in:

Byung-Gil Lee*, **Fabian Merkel***, Matteo Allegretti, Markus Hassler, Christopher Cawood, Léa Lecomte, Francis J. O'Reilly, Ludwig R. Sinn, Pilar Gutierrez-Escribano, Marc Kschonsak, Sol Bravo, Takanori Nakane, Juri Rappsilber, Luis Aragon, Jan Löwe, Christian Haering. Cryo-EM structures of holo condensin reveal a subunit flip-flop mechanism. *Nat Struct Mol Biol.* 2020;27(8):743-751.

*shared first authors

Additional contributions:

Marc Kschonsak, **Fabian Merkel**, Shveta Bisht, Jutta Metz, Vladimir Rybin, Markus Hassler, Christian H. Haering. Structural Basis for a Safety-Belt Mechanism That Anchors Condensin to Chromosomes. *Cell.* 2017;171(3):588-600.

Markus Hassler, Indra A Shaltiel, Marc Kschonsak, Bernd Simon, **Fabian Merkel**, Lena Thaerichen, Henry J Bailey, Jakub Macošek, Sol Bravo, Jutta Metz, Janosch Hennig, Christian Haering. Structural Basis of an Asymmetric Condensin ATPase Cycle. *Mol Cell.* 2019;74(6):1175-1188.

So much universe and so little time.

~Terry Pratchett

Table of Contents

Abstract

Zusammenfassung

1. Introduction	2
1.1 The cell cycle.....	2
1.2 Organizing chromosomes	2
1.2.1 The interphase chromosome.....	2
1.2.2 The mitotic chromosome	4
1.3 Loop-extrusion as the driving force behind chromosome compaction	6
1.4 The condensin complex.....	7
1.4.1 Localization of condensin	8
1.4.2 Interaction with DNA and chromatin.....	9
1.4.3 <i>In vitro</i> activities of condensin	10
1.4.4 Subunit composition of condensin	12
1.4.5 Structural studies of the condensin holo complex.....	15
1.5 Goal of this work	17
2. Results	20
2.1 Purification of <i>S. cerevisiae</i> condensin	20
2.2 Initial structure of the apo state of condensin	20
2.2.1 The arm segment in absence of ATP.....	25
2.2.2 The head segment in absence of ATP.....	26
2.3 Improved structure of the apo state of condensin.....	28
2.3.1 Structure of the entire particle	31
2.3.2 Focused refinement of the arm segment	32
2.3.3 Focused refinement of the head segment.....	34
2.4 High-resolution structures of condensin in absence of ATP.....	36
2.5 Comparison of the zipped and bridged apo states.....	38
2.6 Structure of condensin in the presence of ATP.....	39

2.6.1 The condensin arm segment in presence of ATP	42
2.6.2 The condensin head segment in presence of ATP	43
2.7 Functional analysis of the Smc2-Ycg1 interaction	47
2.8 Ycs4 and Ycg1 binding is mutually exclusive	49
2.9 Crosslinking mass spectrometry of condensin	52
3. Discussion	55
3.1 Summary of the results.....	56
3.2 The role of the condensin arm segment.....	56
3.3 The role of the SMC head domains of condensin	58
3.4 The condensin HEAT-repeat subunits switch position	60
3.5 Possible modes of DNA binding by the condensin complex	61
3.6 A model for the condensin ATPase cycle.....	64
4. Material and Methods.....	67
4.1 Materials	68
4.1.1 Software	68
4.1.2 Strains	69
4.1.3 Plasmids	71
4.1.4 Buffers and media	71
4.1.5 Antibodies.....	72
4.1.6 Data availability	73
4.2 Methods	73
4.2.1 Protein expression and purification	73
4.2.2 Analytical size-exclusion chromatography	75
4.2.3 <i>In vivo</i> crosslinking	75
4.2.4 SDS-PAGE	76
4.2.5 Coomassie staining	77
4.2.6 Western blot	77
4.2.7 Yeast viability test.....	77
4.2.8 Yeast expression test	78

4.2.9 Sequence alignment.....	78
4.3 Cryo-EM techniques.....	79
4.3.1 Cryo-EM sample preparation	79
4.3.2 Data acquisition	80
4.3.3 Data analysis	80
4.3.4 Model building	84
5. Contributions.....	85
6. References.....	86
7. Supplementary Information.....	98
7.1 Abbreviations	98
7.2 List of Figures	99
7.3 List of Tables	100
8. Acknowledgements.....	101

Abstract

Division of one mother cell into two daughter cells resides at the very core of living organisms. To ensure that the cell's genetic material is equally segregated into both daughter cells, cells undergo a sophisticated succession of highly controlled events. One of these events is the packaging of chromatin fibers into mitotic chromosomes that can be transported by spindle microtubules. The key factor for this chromosome condensation process is the five-subunit condensin complex. Condensin is thought to shape chromosomes by actively extruding large chromatin loops, yet how condensin can create such loops has remained largely unknown. To shed light onto the mechanism of condensin-mediated chromatin condensation, insights into the structure of the complex will be indispensable. While X-ray crystallography proved efficient in providing said information for individual parts of the complex, the architecture of the entire complex remained unknown. The aim of the work described in this PhD thesis was to close this crucial gap in knowledge by elucidating the condensin holo complex structure. I employed cryogenic electron microscopy to first solve the structure of the *Saccharomyces cerevisiae* condensin holo complex in its apo and nucleotide-bound states. In the absence of nucleotide, condensin adopts a rod-like conformation. The HEAT-repeat subunit Ycs4 stably interacts with the ATPase head domains of closely aligned Smc2 and Smc4 subunits, while the Ycg1 HEAT-repeat subunit is flexibly tethered to the rest of the complex through the Brn1 subunit. Instead of forming a fully stretched rod, the Smc2–Smc4 coiled-coil arm segment contains a kink that results in the hinge folding back onto the coiled coils. In a second apo state, the Smc2 and Smc4 heads are bridged by Ycs4, which splits apart the Smc2–Smc4 coiled coils from the head to the joint regions. Addition of ATP induces a drastic structural rearrangement. The ATPase heads engage, which results in an increase in flexibility and opening of the coiled coils. Furthermore, Ycg1 and Ycs4 swap positions as ATP releases Ycs4 from the Smc4 ATPase head, which in turn provides access for Ycg1 to directly bind the Smc2 ATPase head domain.

These data provide a structural framework for the condensin ATPase cycle and suggest that an ATP-driven exchange of the Ycs4 and Ycg1 subunits interconverts DNA binding sites that might form the core of the condensin DNA loop-extruding activity.

Zusammenfassung

Die Zellteilung einer Mutterzelle in zwei Tochterzellen ist eine fundamentale Grundlage lebender Organismen. Um sicherzustellen, dass beide Tochterzellen mit demselben genetischen Material ausgestattet werden, durchlaufen Zellen eine Abfolge hochgradig kontrollierter zellulärer Ereignisse. Einer dieser Prozesse ist das Verpacken des fadenförmigen Chromatins in eine transportfähige Struktur – das mitotische Chromosom. Diese sogenannte Chromosomenkondensation wird maßgeblich von dem fünf Untereinheiten umfassenden Condensin Komplex bewerkstelligt. Dabei wird davon ausgegangen, dass Condensin aktiv Chromatinschleifen bildet und auf diese Weise Chromosomen generiert. Wie Condensin auf mechanistische Weise massive strukturelle Veränderungen des Chromatins hervorrufen kann, ist nur unzureichend verstanden. Um den Mechanismus von Condensin und letztendlich der Chromosomenkondensation aufzuklären, sind Einblicke in die Struktur von Condensin unerlässlich. Während sich Röntgenkristallografie als effizient erwies, solche Informationen für Teile des Komplexes zu liefern, blieb die Struktur des Holokomplexes unbekannt. Aus diesem Grund war das Ziel meiner Doktorarbeit die Aufklärung der Struktur des Condensin Holokomplexes. Ich nutzte kryogene Elektronenmikroskopie, um die Struktur des *S. cerevisiae* Condensin Holokomplexes mit und ohne ATP zu lösen. In Abwesenheit von ATP nimmt Condensin eine stabförmige Gestalt an. In dieser Form interagiert die *HEAT-repeat* Untereinheit Ycs4 mit dem SMC Kopf Segment, welches aus nah aneinander liegenden Smc2- und Smc4 ATPase Domänen besteht. Die *HEAT-repeat* Untereinheit Ycg1 dagegen, ist nur flexibel durch die Interaktion mit Brn1 an den Komplex angebunden. Anstatt einen vollständig gestreckten Stab zu bilden, enthält das Armsegment einen Knick, der dazu führt, dass die *hinge* Domäne auf die SMC *coiled coils* zurückfaltet. In einer weiteren Condensin Struktur ohne ATP sind die Smc2 und Smc4 ATPase Domänen von Ycs4 getrennt, was dazu führt, dass sich die *coiled coils* von den SMC Kopf Domänen bis zur *joint* Region trennen. Zugabe von ATP induziert drastische Änderungen in der Condensin Struktur. Zum einen dimerisieren die ATPase Domänen, was zu erhöhter Flexibilität führt und die ursprünglich direkt aneinander liegenden *coiled coils* teilweise voneinander trennt. Zum anderen dissoziiert ATP Ycs4 von der Smc4 ATPase Domäne, wodurch Ycg1 direkt die

ATPase Domäne von Smc2 binden kann. Dies resultiert in einem ATP anhängigen Austausch von Ycs4 und Ycg1.

Diese Daten bieten einen strukturellen Rahmen für den ATPase Zyklus von Condensin und implizieren, dass ein ATP abhängiger Austausch von Ycg1 und Ycs4 DNA innerhalb des Condensin Komplexes befördert. Dies könnte die Grundlage dafür bilden, wie Condensin Chromatinschleifen ausbildet.

1 Introduction

1.1 The cell cycle

The cell cycle, during which a mother cell divides into two daughter cells, is the common denominator of proliferation and growth in all living organisms on this planet. In eukaryotes the cell cycle can be divided into two distinct phases, the I-phase (interphase) and the M-phase (mitotic). Interphase includes two metabolic and growth phases – G1 and G2 – that sandwich the S-phase. During S-phase, the genetic material of the cell is duplicated by DNA replication to create two identical copies named sister chromatids. During M-phase, the sister chromatids are then segregated, followed by the division of the entire cell to generate two genetically identical daughter cells.

As straight forward as this process appears, the cell has to overcome a major obstacle before faithful segregation of the genetic material can occur. This obstacle becomes apparent when considering the dimensions of the DNA content of a cell. In a human somatic cell, ~6.3 giga-base pairs (bp) are distributed over 23 chromosome pairs. Attached end to end, the DNA of the 23 chromosome pairs would add up to a length of more than 2 m (Piovesan et al., 2019), while the nucleus has a diameter of only ~10 μm . The sheer mismatch of these dimensions and the fact that each daughter cell requires exactly one copy of every chromosome illustrates the need of a sophisticated system to organize, disentangle and condense the genetic material.

1.2 Organizing chromosomes

1.2.1 The interphase chromosome

Early studies demonstrated that the first step of DNA organization in the nucleus is the association of DNA with histones (Olins and Olins, 1974). This was later confirmed by a crystal structure of 146 bp DNA wrapped around an octamer of histones giving rise to the nucleosome (Luger et al., 1997). Nucleosomes are positioned every ~200 bp, resulting in the 'beads-on-a-string' appearance for a stretched 11-nm chromatin fiber (**Fig. 1.1A**) (Rattner and Hamkalo, 1978). It was suggested that this 11-nm fiber then forms a higher-order solenoid of nucleosomes, resulting in a 30-nm fiber. *In vitro*, the formation of a 30-nm fiber was confirmed by several different structural and biochemical approaches (Finch and Klug, 1976; Robinson et al., 2006; Staynov,

2000). The existence of such a structure *in vivo*, however, is still under debate. Both, isolated chromatin as well as *in situ* studies combined with cryo-EM, failed to reveal any higher-ordered chromatin fiber (Cai et al., 2018; McDowall et al., 1986). From the results of these studies, chromatin could be rather described as a dynamic chain with a width between 5 and 25 nm (Ou et al., 2017).

In interphase nuclei, chromosomes were initially assumed to form an entangled mass void of major organizational layers (Wischnitzer, 1973). Fluorescence *in situ* hybridization (FISH) proved this assumption wrong by demonstrating that chromosomes occupy distinct territories within a nucleus (Bolzer et al., 2005). In addition, chromosome conformation capture (3C) methods in combination with deep sequencing (Hi-C) uncovered additional levels of organization (Dekker et al., 2002).

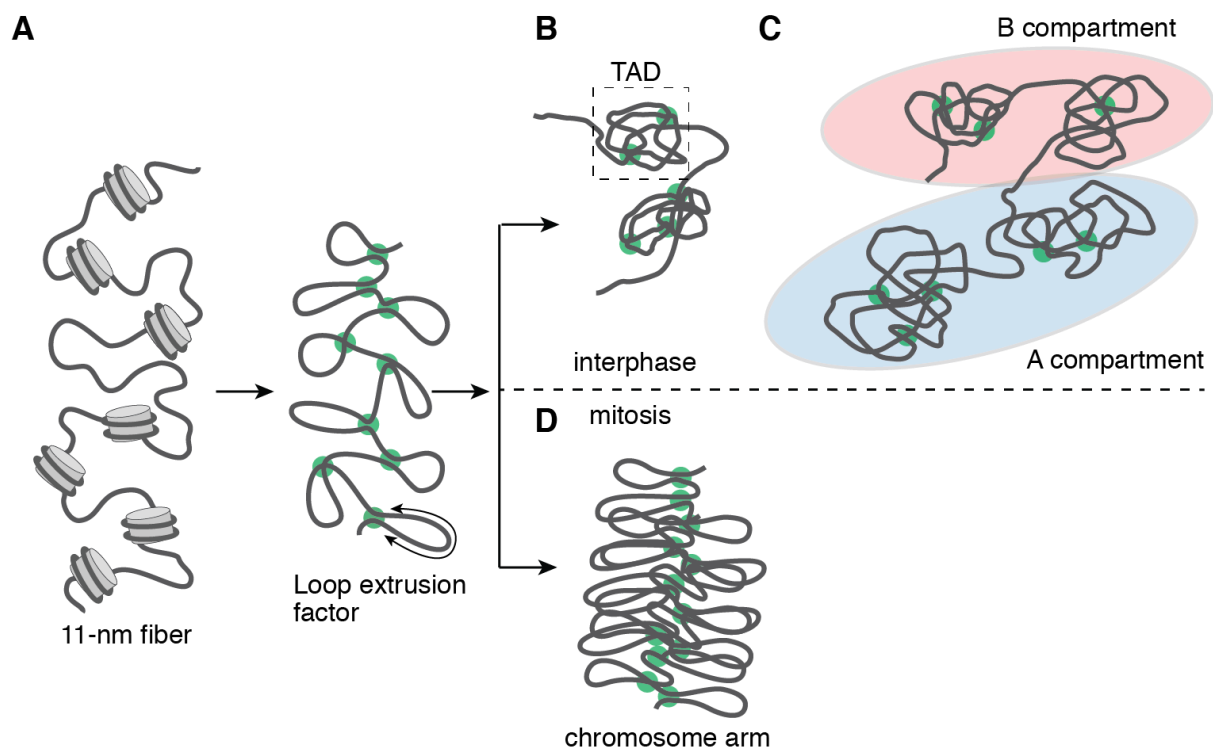


Figure 1.1: 3D organization of chromosomes. (A) The first step in organizing the genetic material of a cell is the wrapping of DNA around histone octamers resulting in the 11-nm fiber. Loop-extrusion factors (green dots) are thought to shape chromatin by interacting with DNA and actively extruding loops. (B) In interphase nuclei, loop-extrusion results in the formation of topology-associated domains (TADs) defined by an increased interaction frequency of loci within the TAD. (C) Chromatin in a cell can be divided into two major entities. An active A compartment and an inactive B compartment. (D) In mitosis, loop-extrusion factors were suggested to condense interphase chromatin into mitotic chromosomes by stacking chromatin loops on top of each other (adapted from Kschonsak and Haering, 2015).

These studies revealed topology associated domains (TADs), chromosomal regions defined by a two-fold increase in interactions of loci within the TAD compared to

interaction frequencies with regions outside the TAD (**Fig. 1.1B**) (Chang et al., 2020; Dixon et al., 2012; Nora et al., 2012). Hi-C also demonstrated that, at the mega-base pair scale, chromatin is in general divided into two compartments, named A and B compartments. Similar to TADs, interaction frequencies were higher within a compartment than across compartments. In addition, compartments A and B could not only be separated by their contact frequencies, but also by their overall genomic activity. Compartment A was associated with active, open chromatin, while compartment B contained mostly closed, inactive chromatin (**Fig. 3.1C**) (Lieberman-Aiden et al., 2009).

Despite of this sophisticated spatial organization during interphase, chromosomes need to be even further packed into dense mitotic chromosomes that can be faithfully segregated during mitosis.

1.2.2 The mitotic chromosome

The drastic structural rearrangements that lead from interphase chromosomes to mitotic chromosomes have been studied for more than 140 years (Flemming, 1882). Forming a total of 46 X-shaped mitotic chromosomes out of 92 chromatin fibers in human cells requires two essential and interlinked processes: Individualization and condensation.

Individualization

The semiconservative mode of replication requires unwinding of the DNA double helix, which in turn creates torsional stress and ultimately results in intertwinings between newly synthesized sister chromatids (Meselson and Stahl, 1958; Peter et al., 1998). Individualization is necessary to prevent persisting intertwinings (catenanes) between sister chromatids during anaphase which could result in DNA breaks (Spell and Holm, 1994). This task is further complicated by the fact that the cell has to keep sister chromatids close together to 'know' which chromatids are sisters that need to be separated during anaphase.

The protein complex responsible for linking sister chromatids until anaphase is named cohesin (reviewed in Nasmyth, 2001). Individualization of chromosomes is supported by the topoisomerase (Topo) family of proteins (reviewed in Champoux, 2001). There are two types of topoisomerases. Type I creates and re-anneals single strand DNA (ssDNA) breaks. Type II creates a double strand break and passes a second double-stranded DNA (dsDNA) region through this gap. While Topo I is important to relieve torsional stress during replication and transcription (Promonet et al., 2020; Tuduri et al., 2009), it is Topo II that resolves sister chromatid catenanes (Holm et al., 1985; Sundin and Varshavsky, 1981; Uemura et al., 1987). Surprisingly, *in vitro*, the activity of Topo II equally likely introduces catenanes as it resolves them (Kreuzer and Cozzarelli, 1980). The balance can only be shifted towards decatenation by changing the local concentration of DNA strands (Kreuzer and Cozzarelli, 1980). It was proposed that this is the reason why Topo II decatenates efficiently only when sister chromatids become slightly separated from each other during the onset of mitotic chromosome condensation (Holm, 1994; Uemura et al., 1987). An alternative way of regulating Topo II is through the geometry of its DNA substrate. This notion is supported by the finding that the topology of centromeric plasmids shifted towards positive supercoiling when progressing through mitosis, which specifically induced their decatenation (Baxter et al., 2011).

Condensation

Packing an ~85-mm long DNA duplex (*Hs* chromosome 1) into a 10- μ m long and 2- μ m wide cylindrical body is a daunting task. Wrapping the DNA around histone octamers to create the 11-nm fiber shortens the DNA six-fold and can thus not explain the entire condensation process on its own (Marko, 2008). The additional wrapping of the 11-nm fiber into a hypothetical 30-nm fiber would result in a 30-fold compaction compared to naked DNA, which, even if there were evidence for a 30-nm fiber in mitotic chromosomes, is still insufficient to explain the size of a mitotic chromosome (Marko, 2008). This simple calculation led to the postulation of another layer of folding of 30-nm fibers into a hollow super-solenoid of 400 nm (hierarchical model for chromosome folding) (Bak et al., 1977).

In contrast, when Lämmli and colleagues isolated metaphase chromosomes depleted of histones, they discovered a structure that appeared to be a central proteinaceous scaffold with loops of DNA emanating from said scaffold (Earnshaw and Laemmli, 1983; Paulson and Laemmli, 1977). In later experiments, Poirier and Marko incubated newt chromosomes with a restriction enzyme that cleaved frequently. Surprisingly, the cleaved chromosome disintegrated, which argued against the idea of a continuous proteinaceous scaffold that shapes mitotic chromosomes. Instead, their findings suggested that the mechanical stability of chromosomes is conferred by the chromatin itself (Poirier and Marko, 2002).

Irrespective of its caveats, the rigid scaffold model shifted the focus from nucleosome-nucleosome based folding mechanisms to the presence of non-nucleosomal proteins that might create some form of a chromosome axis. Apart from histones, the most abundant protein components of mitotic chromosomes are the above mentioned Topo II as well as a protein complex termed condensin (Gasser et al., 1986; Lewis and Laemmli, 1982; Maeshima and Laemmli, 2003). Condensin complexes had initially been discovered in *Xenopus laevis* egg extracts and in genetic screens in yeast. They were named for their influence on chromosome condensation (Hirano et al., 1997; Hirano and Mitchison, 1994; Saitoh et al., 1994; Strunnikov et al., 1995). This key role of condensin was further supported by the fact that a condensin genetic knock-out in mice abolished chromosome condensation completely (Houlard et al., 2015). An additional line of evidence for the essential role of condensin in chromosome compaction came recently from experiments by Hirano and colleagues, who succeeded in reconstituting mitotic-like chromatids *in vitro* with only core histones, three histone chaperones, Topo II and condensin (Shintomi et al., 2015). Other factors, like RCA, Kif4A, Pin1 and histone modifications, have also been implicated in chromosome condensation, but their roles remain largely elusive (Takata et al., 2018; Vagnarelli et al., 2006; Xu and Manley, 2007)

1.3 Loop-extrusion as the driving force behind chromosome compaction

DNA loop-extrusion can be defined as a gradual process in which one or several proteins actively reel in DNA from one or both sides, giving rise to a growing loop of

DNA. Since the discovery of DNA loops that emanated from a central protein scaffold in EM micrographs, DNA looping was proposed as a model for chromosome condensation by several authors (Guacci et al., 1993; Nasmyth, 2001; Paulson and Laemmli, 1977; Riggs et al., 1990). Theoretical models agreed that molecular machines could in principal compact a chromatin fiber into a rod by extruding loops (Alipour and Marko, 2012).

The idea of DNA loops as the building blocks of mitotic chromosomes was also supported by 3C methods. Dekker and colleagues used a 3D polymer simulation to show that it was possible to explain the changes in interaction maps of chromosomes upon entry into mitosis by the formation of loops of 80-120 kb in size, while A and B compartmentalization, as well as TADs, were strongly reduced (Naumova et al., 2013). Later studies also came to the conclusion that the collective effort of loop-extruding factors alone is sufficient to compact and disentangle chromosomes (Goloborodko et al., 2016). The SMC protein family, with its members condensin and cohesin, had been proposed to have the DNA motor activity that would be required for active loop-extrusion (Guacci et al., 1993; Nasmyth, 2001; Peterson, 1994). Indeed, recent work in cultured cells that entered mitosis in a highly synchronized manner suggested that chromosomes are made of loops stacked helically on top of each other, with condensin sitting at the bases of such loops (Gibcus et al., 2018).

1.4 The condensin complex

The condensin complex was discovered and named by Hirano and colleagues, although some of its subunits had already been identified earlier (Hirano et al., 1997; Hirano and Mitchison, 1994; Strunnikov et al., 1995). Condensin consists of five subunits: Smc2 and Smc4, a kleisin subunit and two HEAT-repeat proteins (**H**untingtin, **e**longation factor 3, **p**rotein **p**hosphatase **2A**, **T**or1) (**Fig. 1.2**). Together with cohesin and the Smc5/6 complex, condensin completes the family of eukaryotic SMC proteins. Condensin is highly conserved throughout the entire eukarya kingdom and most eukaryotes express two distinct complexes, condensin I and II. Both complexes share the Smc2 and Smc4 subunits but differ in their non-SMC subunit composition (Ono et al., 2003; Yeong et al., 2003).

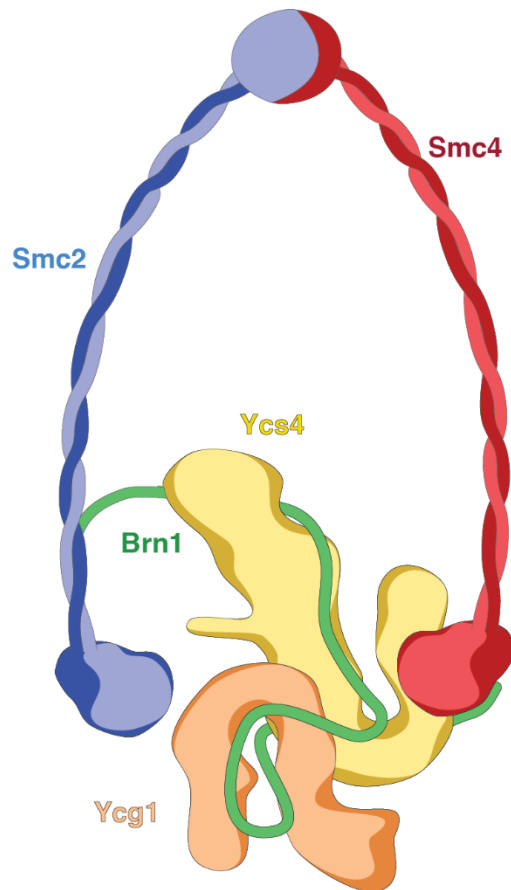


Figure 1.2: The condensin complex. Condensin consists of two members of the SMC (structural maintenance of chromosomes) protein family, Smc2 and Smc4. Both interact directly with each other through the hinge domain at the end of their coiled-coil arm segment and with the kleisin subunit Brn1 at their ATPase head domains giving rise to the model of a tripartite ring. The complex is completed by two HEAT-repeat rich subunits, Ycg1 and Ycs4 (Adapted from Hassler et al., 2019)

It is assumed that the last eukaryote common ancestor (LECA) possessed both complexes and that complex II was independently lost several times during evolution (Hirano, 2012). The *Saccharomyces cerevisiae* genome, for example, only encodes a single condensin complex, and several insect species have lost different subunits of condensin II, while evolutionary pressure apparently maintained the remaining subunits (King et al., 2019).

1.4.1 Localization of condensin

Early fluorescence microscopy data revealed that condensin complexes occupy the central axis of human chromosomes with alternating condensin I and II foci (Ono et al., 2003; Saitoh et al., 1994). Furthermore, ChIP-seq studies showed that condensin

is highly enriched at specific chromosomal loci, like centromeres, telomeres and the highly repetitive rDNA locus (Ciosk et al., 2000; Wang et al., 2005). Walther and colleagues have produced a quantitative map of condensin I and II in HeLa cells, using endogenously tagged condensin subunits. FCS (fluorescence correlation spectroscopy) calibrated live-cell imaging revealed that about 35,000 condensin II complexes and 195,000 condensin I complexes stably bind to chromosomes throughout mitosis. Interestingly, super-resolution microscopy indicated that condensin II localizes to the central axis of the chromosome, while condensin I surrounds the space occupied by condensin II (Walther et al., 2018). This result is also in line with Hi-C data of synchronized chicken DT40 cells, where condensin II creates the spiral staircase architecture in ~400-kb loops, while condensin I subdivides these loops into smaller loops of an average size of ~80 kb (Gibcus et al., 2018).

One possible explanation for the differences between condensin I and II can be found in the residence time of condensin on chromosomes. Fluorescence recovery after photobleaching (FRAP) experiments demonstrated that condensin II binds to chromosomes over long time periods, while condensin I has a more dynamical mode of interaction (Gerlich et al., 2006). It is also conceivable that the localization of condensin I and II throughout the cell cycle influences their position and function on chromosomes. While condensin II is nuclear during interphase and is hence always in vicinity of chromatin, condensin I displays a cytoplasmic localization during interphase. For this reason, condensin I can access chromatin only upon nuclear envelope breakdown (NEBD) during prometaphase, whereas condensin II shows chromatin localization already during prophase, when condensation starts (Hirota et al., 2004).

1.4.2 Interaction with DNA and chromatin

The fundamental prerequisite for condensin's genome organizing activity is its interaction with chromatin. Early studies identified putative DNA interaction sites in several subunits. Full-length Smc2 and Smc4 were reported to bind DNA, as well as the isolated Smc2–Smc4 hinge domain (Sakai et al., 2003a; Stray and Lindsley, 2003). Surprisingly, the hinge domain showed a preference for ssDNA (Griese et al., 2010; Piazza et al., 2014). In addition, the non-SMC subunits have been implied in DNA binding (Piazza et al., 2014).

These studies suggest that condensin interacts with DNA without any additional loading factors. This is in contrast to cohesin, where a separate Scc2–Scc4 complex is thought to serve as a chromosome loader (Ciosk et al., 2000). The Scc2–Scc4 complex and TFIIC were also implied in condensin loading, mainly due to the finding that their peaks overlapped in ChIP-Sep experiments. TFIIC has been reported to bind condensin, but these results could not be confirmed by experiments with purified protein complexes (Sakai et al., 2003a; Yuen et al., 2017). Albeit not entirely excluding the existence of a condensin loader, the fact that in *Xenopus* neither Scc2–Scc4 nor TFIIC are necessary for chromosome condensation argues against an essential role of said factors in chromosome compaction (Shintomi et al., 2015).

In a recent study, Kschonsak and colleagues reported the crystal structure of the HEAT-repeat subunit Ycg1 and the kleisin subunit Brn1 in complex with DNA (Kschonsak et al., 2017). In this structure, DNA binds in a positively charged groove of Ycg1. Brn1 wraps around the DNA in an arrangement that resembles a safety belt, holding on to DNA (**Fig. 1.3C**). Mutation of this binding interface resulted in a loss of condensin's chromosome association *in vivo*. In addition to such a direct protein-DNA interaction, condensin was also proposed to interact with DNA in a topological embrace, entrapping strands of DNA within its putative ring-like structure (Cuylen et al., 2011). A similar mode of action was previously suggested for cohesin (Nasmyth, 2001).

1.4.3 *In vitro* activities of condensin

Multiple catalytic activities of the condensin holo complex were suggested to serve as a mechanistic basis for chromosome compaction.

DNA supercoiling

A specific *in vitro* activity was first described for condensin I complexes immunopurified from *Xenopus laevis* egg extracts. In the presence of ATP, condensin was shown to introduce positive supercoils into closed circular plasmids (Kimura and Hirano, 1997). Such an activity could be explained by the complex moving along DNA (Tsao et al.,

1989). A follow-up study revealed that this activity was most likely caused by a single condensin molecule, arguing against a cooperative activity between different condensin complexes (Bazett-Jones et al., 2002).

DNA re-annealing

A study using purified *Schizosaccharomyces pombe* Smc2–Smc4 dimers or condensin holo complexes found that Smc2–Smc4 dimers possess the ability to promote the re-annealing of ssDNA into dsDNA, whereas the holo complex did not show this activity. Curiously, even truncating the head domain of one SMC protein within the heterodimer resulted in DNA re-annealing (Sakai et al., 2003b). How this activity relates to organizing mitotic chromosomes remains unknown. There is evidence, however, for an increase in the fraction of ssDNA during mitosis compared to interphase, revealed by elevated susceptibility of mitotic chromatin to the ssDNA nuclease S1 (Juan et al., 1996).

DNA compaction

Strick and colleagues found that purified *Xenopus laevis* condensin complexes compact a linear piece of dsDNA attached on one end to a glass surface and on the other end to a magnetic bead. Importantly, while this reaction required ATP, binding of the complex to DNA itself was ATP independent (Strick et al., 2004). Similar results were obtained in magnetic tweezers studies with budding yeast condensin, which revealed two different DNA binding modes: The first electrostatic interaction with DNA was ATP-independent. The second, processive interaction in terms of DNA compaction, required ATP and involved topological entrapment of DNA (Eeftens et al., 2017). In contrast, another magnetic tweezers study concluded that condensin adopts monomeric and oligomeric states and that only the condensin oligomer can compact DNA in the presence of ATP, taking 600-bp steps (Keenholtz et al., 2017). Along these lines, a similar type of experiment with the bacterial SMC-like protein MukB also led to DNA compaction in a highly cooperative process, albeit in the absence of ATP (Cui et al., 2008).

DNA loop-extrusion

Although DNA loop-extrusion was put forth as a potential mechanism to compact chromosomes (see chapter 1.3), direct evidence for such an activity remained elusive. Using DNA curtains and purified *Saccharomyces cerevisiae* condensin revealed that condensin is an ATP-dependent DNA translocase (Terakawa et al., 2017). Consistent with this conclusion, ATPase mutants failed to translocate along DNA and translocation did not proceed in presence of non-hydrolysable ATP analogs. Importantly, condensin was able to bind to a second DNA fragment and move it relative to the one it translocated on (Terakawa et al., 2017). In a follow-up study, DNA molecules were bound to a surface without being fully extended (Ganji et al., 2018). This allowed the observation of asymmetric DNA loop-extrusion by single condensin complexes, as judged from their photobleaching patterns. The asymmetry was explained by two distinct 'domains' in the complex, an anchor that grabs and holds on to DNA and a 'motor' that reels in DNA step-wise (Ganji et al., 2018). A similar activity was also recently described for cohesin, albeit it reeled in DNA in a symmetric manner (Davidson et al., 2019; Kim et al., 2019).

1.4.4 Subunit composition of condensin

Smc2 and Smc4

Smc2 and Smc4 are members of the structural maintenance of chromosomes protein family. The structure of these proteins can be divided into three parts. Amino- and carboxy-terminal ends interact closely with each other and form a globular 'head' domain. The central part of the protein gives rise to another globular half 'hinge' domain. Both helical strands between amino- and carboxy-termini and hinge adopt an extended anti-parallel coiled-coil (**Fig. 1.3A**) (Haering et al., 2002). Smc2 and Smc4 can interact with each other via their hinge domains, giving rise to a heterodimer (Schmiesing et al., 1998). In addition, each 'head' domain contains an ATPase site that consists of a Walker A motif in the amino-terminal end and a Walker B motif in the carboxy-terminal end (Saitoh et al., 1994). Reminiscent of ATP binding cassette (ABC) type of transporters, SMC proteins have composite catalytic sites (Hopfner, 2016). Upon ATP binding, both head domains engage by sandwiching two molecules of ATP between their Walker A motifs in one head and so-called signature motifs located just

amino-terminal of the Walker B motif on the opposite head (**Fig. 1.3B**) (Haering et al., 2004; Muir et al., 2020). This suggests an ATPase cycle where ATP binding results in engagement of two SMC heads followed by ATP hydrolysis and release, which disengages the heads again.

To study this simplified model in more detail, mutations of the ATP binding site have been analyzed. Surprisingly, the ATPase sites of Smc2 and Smc4 were found to be asymmetric in their activity, leading to a specific order of events. First, ATP binds to Smc4, which results in a partially engaged state where the heads dimerize through the Smc4 ATP binding site alone (further discussed below). Only thereafter can ATP bind to Smc2 and give rise to a fully engaged Smc2–Smc4 dimer (Hassler et al., 2019).

Brn1

In addition to their interaction interfaces at the hinge and head domains, the two SMC subunits are also connected by a kleisin subunit (Haering et al., 2002). Brn1, the condensin kleisin, was first discovered in a *Drosophila* screen for genes affecting nervous system development (Kania et al., 1995). Like all kleisin subunits, Brn1 interacts with the Smc2 and Smc4 subunits in fundamentally different ways. The interaction interface between Brn1 and Smc4 is located at the base of the Smc4 head domain and is mediated by a winged-helix domain (WHD) of Brn1 (**Fig 1.3C**) (Hassler et al., 2019). This interface appears to bind constitutively throughout the entire reaction cycle. At the other end, Brn1 contacts the coiled coils just above the Smc2 head domain via its amino-terminal helical domain (**Fig. 1.3C**). This interaction is at least temporarily disrupted by ATP binding (Hassler et al., 2019). The architecture of the SMC dimer connected by a kleisin led to the hypothesis that SMC protein complexes form tripartite rings and that this ring-like structure is at the base of their mechanism (Cuylen et al., 2011; Gruber et al., 2003; Haering et al., 2008; Onn et al., 2007). In addition to binding the SMC head domains with their WHD and helical domains, kleisins serve as unstructured linkers between the SMC subunits and the HEAT-repeat subunits.

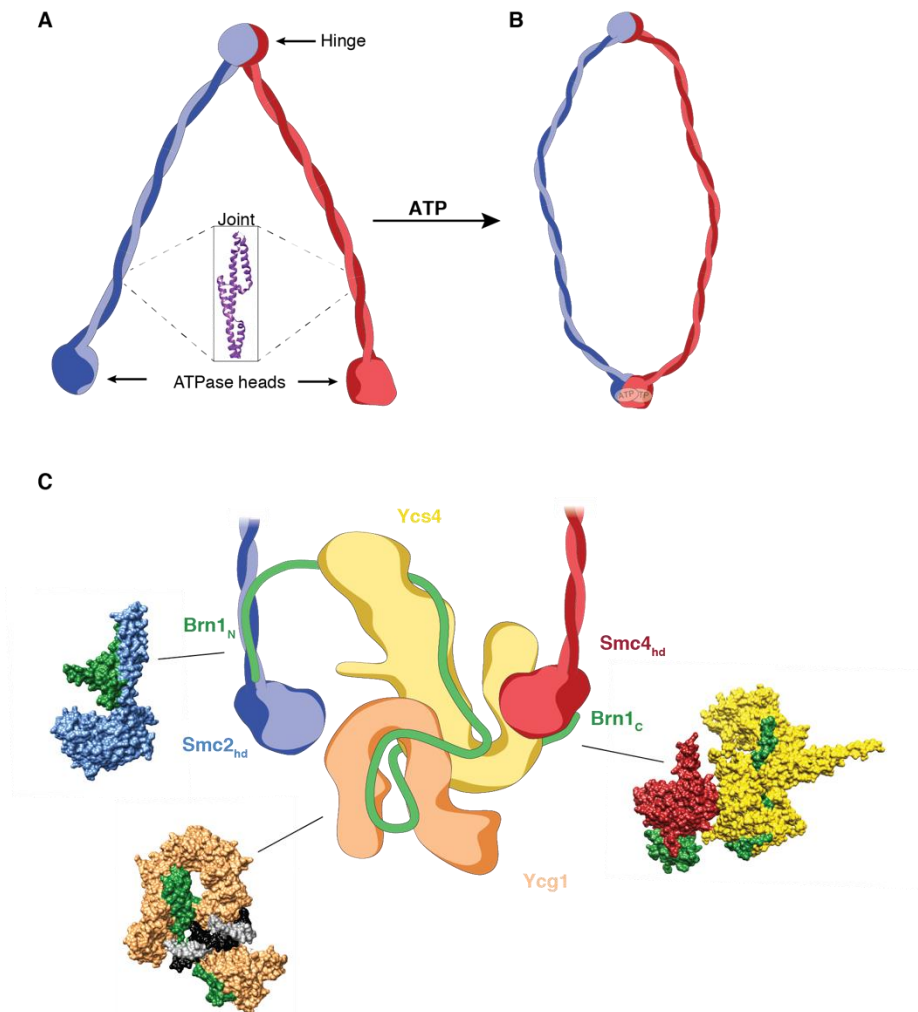


Figure 1.3: Subunit composition of condensin. (A) Smc2 and Smc4 form extended anti-parallel coiled coils with their amino and carboxy termini creating the 'head' domains. A globular central part forms the hinge domain upon constitutive heterodimerization. The head domains contain ATP binding sites. The joint region is a disruption in the otherwise mostly helical coiled coils (PDB: 5XEI). (B) Smc2 and Smc4 head domains can engage upon binding of two ATP molecules. (C) The amino-terminal Brn1_N interacts with the Smc2 neck region. Ycg1, together with its interacting Brn1_{Ycg1} fragment was shown to bind DNA (black/white). The carboxy-terminal winged-helix-domain (WHD) of Brn1 (Brn1_C) interacts with the Smc4 head domain. Ycs4 interacts constitutively with Brn1_{Ycs4} and in an ATP regulated manner with the Smc4 head domain (PDBs from left to right: Model of 6QJ1 with 6QE6, 5OQP, 6QJ4).

Ycg1 and Ycs4

The condensin complex is completed by two HEAT-repeat subunits, Ycg1 and Ycs4. As their name implies, the predominant feature of Ycs4 and Ycg1 of condensin and their functional orthologs in cohesin is the high number of HEAT-repeat motifs. HEAT-repeats are composed of a pair of alpha helices connected via a short linker. Although

conservation is weak on a sequence level, HEAT-repeat proteins often form solenoids with varying flexibility, properties that have also been shown for Ycg1 and Ycs4 (Hassler et al., 2019; Kschonsak et al., 2017; Manalastas-Cantos et al., 2019). Pulldown experiments with Brn1 fragments confirmed that Ycg1 binds in the carboxy-terminal part, while Ycs4 binds in the amino-terminal part of Brn1. Importantly, the two HEAT-repeat subunits bind to the kleisin independently of each other (Onn et al., 2007; Piazza et al., 2014). The so-called non-SMC complex that consists of Ycg1, Ycs4 and Brn1 was also found to interact with DNA (discussed below; Piazza et al., 2014). Currently, there is no evidence that the Brn1–Ycs4 and Brn1–Ycg1 interactions are regulated.

Ycs4 not only binds to Brn1, but also directly to Smc4 at the head domain (**Fig. 1C**). As a consequence of structural rearrangements within the Smc4 head domain upon ATP binding, this interaction is lost. The physiological relevance of this interaction remains unknown, but mutational analysis revealed that the Ycs4–Smc4 interaction is essential in yeast and abolishes chromatin association of condensin in human cells (Hassler et al., 2019).

1.4.5 Structural studies of the condensin holo complex

The architecture of a bacterial SMC homodimer was first described by Melby and colleagues using rotary-shadowing EM. Rotary shadowing is a special form of negative staining where the sample is dried on a mica surface. The sample is then coated with a mixture of platinum and carbon (Fowler and Erickson, 1979). Rotary-shadowed SMC dimers revealed a high degree of flexibility in the coiled coils, ranging from entirely zipped up rods to ring-like structures (Melby et al., 1998). In a follow-up study, similar experiments were carried out with purified human and *Xenopus laevis* condensin holo complexes. Micrographs depicted a similar range from rod-like to ring-like shapes (Anderson et al., 2002). The same results were obtained with condensin complexes purified from *S. cerevisiae* (**Fig. 1.4**). A high degree of flexibility was also suggested by studies applying atomic force microscopy (AFM) on Smc2–Smc4 dimers, where several different conformations with completely open coiled coils or head-hinge colocalizations were reported (Eeftens et al., 2016). In contrast, applying a combination of X-ray crystallography and crosslinking mass spectrometry, Diebold-

Durand and colleagues concluded that the bacterial condensin Smc–ScpAB complex adopts a stiff rod-like structure (Diebold-Durand et al., 2017).

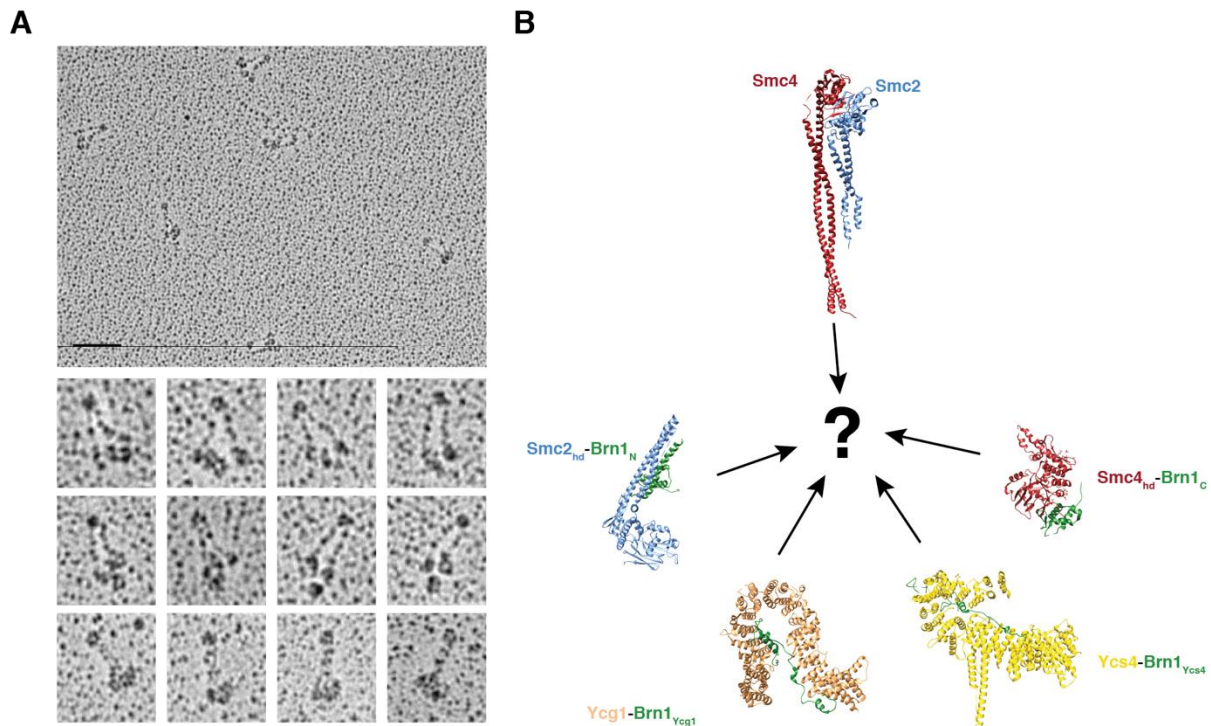


Figure 1.4: Architecture of the condensin holo complex. (A) Rotary shadowing of *S. cerevisiae* condensin revealed ring-shaped and rod-shaped particles (from Terakawa et al. 2017). The particles display density at the base of the complex likely corresponding to the ATPase domains and the HEAT-repeat subunits Ycs4 and Ycg1. Globular density at the end of the particles likely corresponds to the hinge domain. (B) Although structural information of single subunits (PDBs from left to right: Model of 6QJ1 and 6Q6E, 5OQQ, 4RSI, 6QJ2, 6QJ3) is available, it remained unclear how the single parts come together to form the holo complex of condensin.

1.5 Goal of this work

The activity of DNA loop-extrusion is widely regarded as the basic mechanism for the organization of mitotic chromosomes by condensin and of interphase chromatin by cohesin. How the condensin complex mechanistically performs DNA loop-extrusion or any of the other above-mentioned activities, however, remains entirely unknown. To shed electrons onto this 20-year old mystery, it will be essential to understand the 3D architecture of the condensin holo complex.

Due to its challenging size, shape and biochemical properties of the condensin complex, high-resolution information had so far been limited to single subunits or smaller subcomplexes (Griese et al., 2010; Hara et al., 2019; Hassler et al., 2019; Kschonsak et al., 2017).

The aim of my PhD thesis was to understand how these single parts come together to form the condensin holo complex (**Fig. 1.4B**). To achieve this, I used single particle analysis cryo-EM with purified *S. cerevisiae* condensin complexes. Based on the obtained structures, I intended to further our understanding of the dynamic changes in the architecture of the complex that presumably drive DNA loop-extrusion.

2 Results

2.1 Purification of *S. cerevisiae* condensin

To determine the structure of the entire condensin complex, the *Saccharomyces cerevisiae* condensin holo complex was overexpressed in *S. cerevisiae* and purified following a three-step purification protocol as previously described (Terakawa et al., 2017). The final size exclusion chromatography purification displayed a single major peak with a small shoulder that presumably corresponds to a small degree of complex aggregation (**Fig. 2.1A**). Fractions of the main peak were pooled and analyzed by SDS-PAGE, which confirmed the presence of all five condensin subunits (**Fig. 2.1B**). Condensin complexes purified in this manner were routinely used for biochemical and biophysical assays, like EMSA, single-molecule imaging and measurement of ATPase activity (not part of this study) and were thus deemed functional complexes.

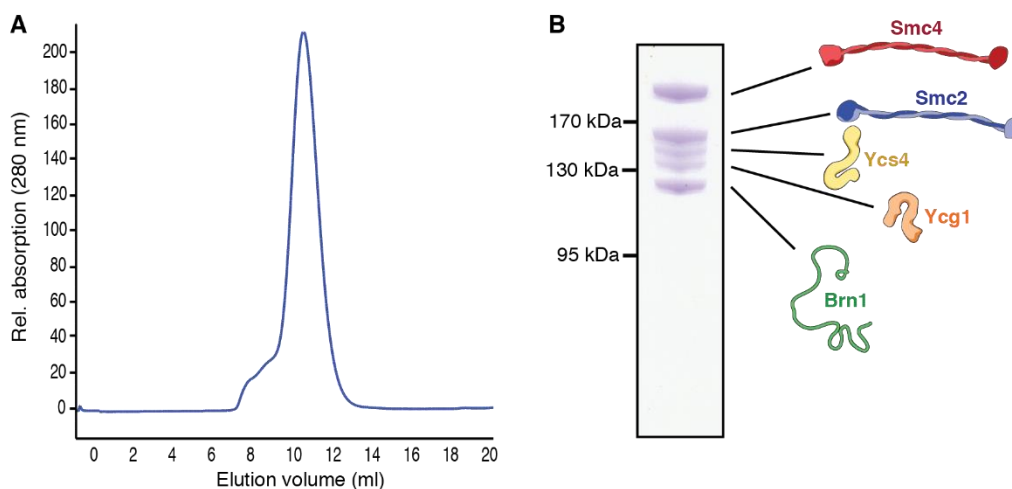


Figure 2.1: Purification of the *S. cerevisiae* condensin holo complex. (A) Size exclusion chromatography of *S. cerevisiae* condensin displaying a single major peak. (B) Coomassie stained SDS-PAGE gel of a representative peak fraction from size exclusion chromatography confirming the presence of all five condensin subunits. Purification experiments were performed by Maria Sol Bravo.

2.2 Initial structure of the apo state of condensin

After screening a range of different conditions, I acquired a first dataset of condensin holo complexes in absence of ATP on a Talos Arctica electron microscope. The dataset consisted of 2,755 movies. In these movies, condensin complexes displayed rod-like shapes (**Fig. 2.2A**), as opposed to the suggested ring-like structure of SMC protein complexes (Gligoris and Löwe, 2016; Gruber et al., 2003). In addition, with a

length of ~40 nm, the complexes were shorter than the 50-nm complexes that had been reported previously for rotary-shadowed specimen (Terakawa et al., 2017).

Compared to a globular protein, a rod-shaped particle creates very different 2D projections, which could result in a bias during template-based particle picking. To address this issue, I set the autopicking threshold low enough so that most features of increased contrast were selected (**Fig. 2.2B**). As expected, this led not only to the selection of clean particles, but also included many broken or partial particles, high-contrast contaminations or beam fringes, which were evident from the first round of template-free 2D classification (**Fig. 2.2C**). To avoid removing rare orientations, I discarded only particles that resulted in obvious “junk” 2D classes and subjected the remaining particles to further rounds of 2D classifications until a sufficiently clean set of particles had been identified (**Fig. 2.2D**).

Most of the 2D class averages adopted clear rod-like shapes that presumably consisted of the Smc2 and Smc4 coiled coils. Additional density at the base most likely corresponded to the non-SMC subunits. Surprisingly, the end of the coiled coils displayed no globular density of the hinge domain as was shown by rotary shadowing EM (Terakawa et al., 2017). Further, a minority of 2D class averages contained only a single hook-shaped density (**Fig. 2.2D**). It is conceivable that some complexes disintegrated, resulting in the presence of single subunits instead of only complete complexes. The fuzzy density around this hook-shaped particle could also indicate that this part is only flexibly tethered to the rod-shaped complex.

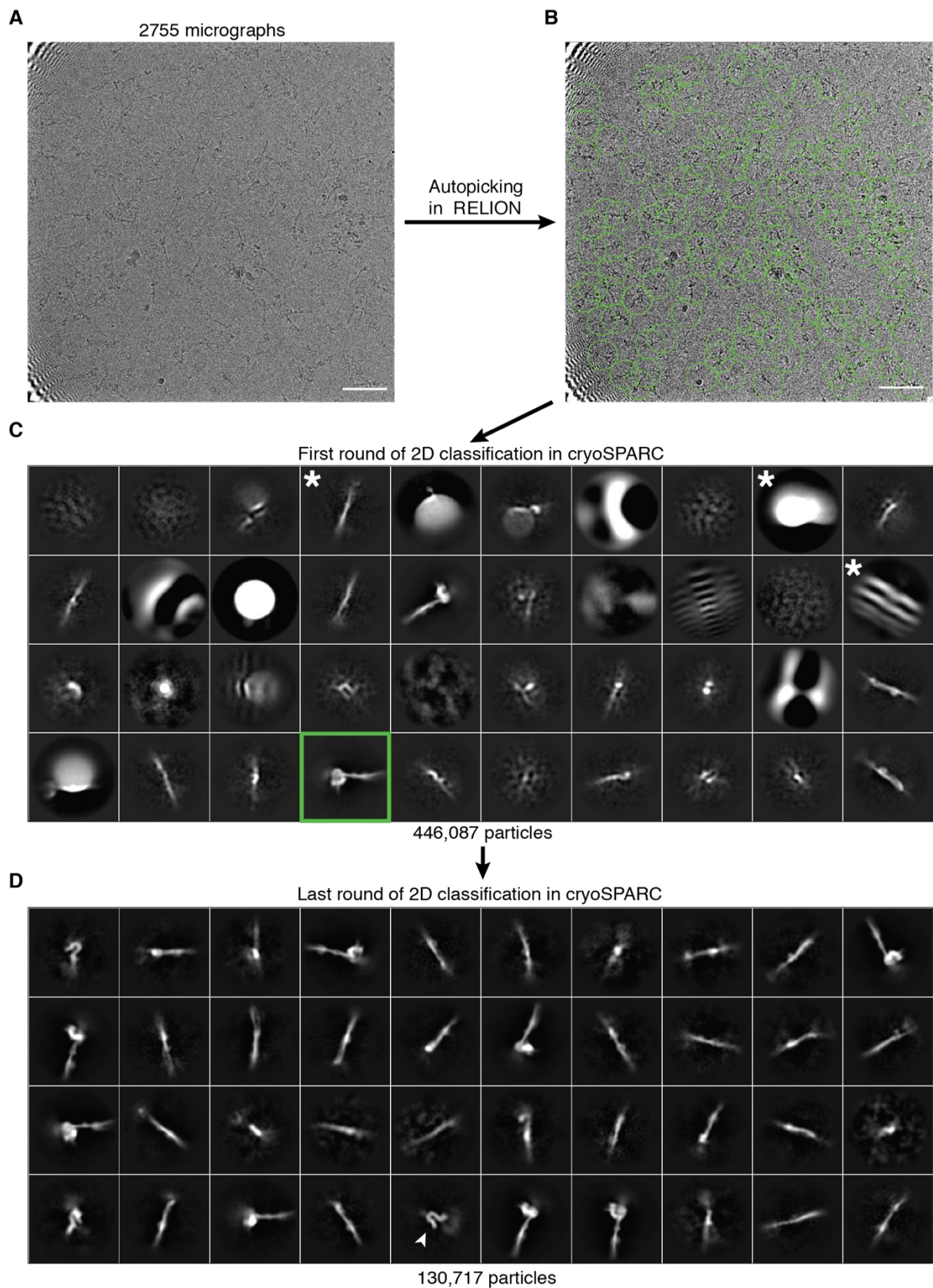


Figure 2.2: Cryo-EM of *S. cerevisiae* holo condensin. (A) Representative micrograph of a dataset acquired on a Talos Arctica cryo-EM microscope. (B) 2D template-based autopicking (green circles) in Relion was performed with low thresholds to avoid introducing biases. (Continued on next page)

(C) The dataset was cleaned up by several rounds of template-free 2D classifications. The first round showed only few clean classes (green squared 2D average as an example) and many broken particles, beam fringes or other contaminations (white asterisks). (D) After removing particles from obvious 'junk' 2D class averages for several rounds of 2D classifications, a final set of 130,717 particles was obtained. Most classes displayed rod-shaped particles while few 2D class averages contained smaller, hook-shaped particles (white arrowhead).

To reconstruct a 3D volume of the 130,717 particles, a *de novo* initial model was created. This initial model then served as a reference to align all particles with a 20-pixel offset search (**Fig. 2.3A**). I included this step because particles often appeared to be off-center after picking, possibly due to the elongated shape of the particle. Another round of 2D classification using the alignment angles from the previous 3D classification cleaned up the dataset further (**Fig. 2.3B**). I then subjected the resulting 95,090 particles to a final round of 3D classification. Refinement of one of the classes resulted in a clean density map of 16.7 Å resolution (**Fig. 2.3C, Fig. 2.3E**).

To validate the density map, I manually fitted published structures of the *C. thermophilum* Ycs4-Brn1_{Ycs4} subcomplex bound to Smc4_{hd}-Brn1_c (PDB: 6QJ4), the *S. cerevisiae* Ycg1-Brn1_{Ycg1} subcomplex (PDB: 5OQQ), the *S. cerevisiae* Smc2-Smc4 hinge domain (PDB: 4RSI) and a model of the *C. thermophilum* Smc2_{hd} (PDB: 6QJ1) bound to the *Ct* Brn1_N domain (PDB: 6Q6E) into the cryo-EM density map. The rod-like map confirmed that, in the cryo-EM images, the hinge was not located at the end of the rod-shaped particle, contrary to data from rotary-shadowed condensin particles (Terakawa et al., 2017). Instead, the hinge folded back onto the coiled coils (**Fig. 2.3D**). A similar "folded" conformation was recently suggested for cohesin based on 2D negative-stained specimen (Bürmann et al., 2019).

At the base of the rod-shaped particle, I was able to place both *Ct* Smc2_{hd}-Brn1_N and Smc4_{hd}-Brn1_c into the cryo-EM density, as well as *Ct* Ycs4-Brn1_{Ycs4} based on its peculiar proboscis element (**Fig. 2.3D**). The remaining unaccounted density accounted for the SMC coiled coils.

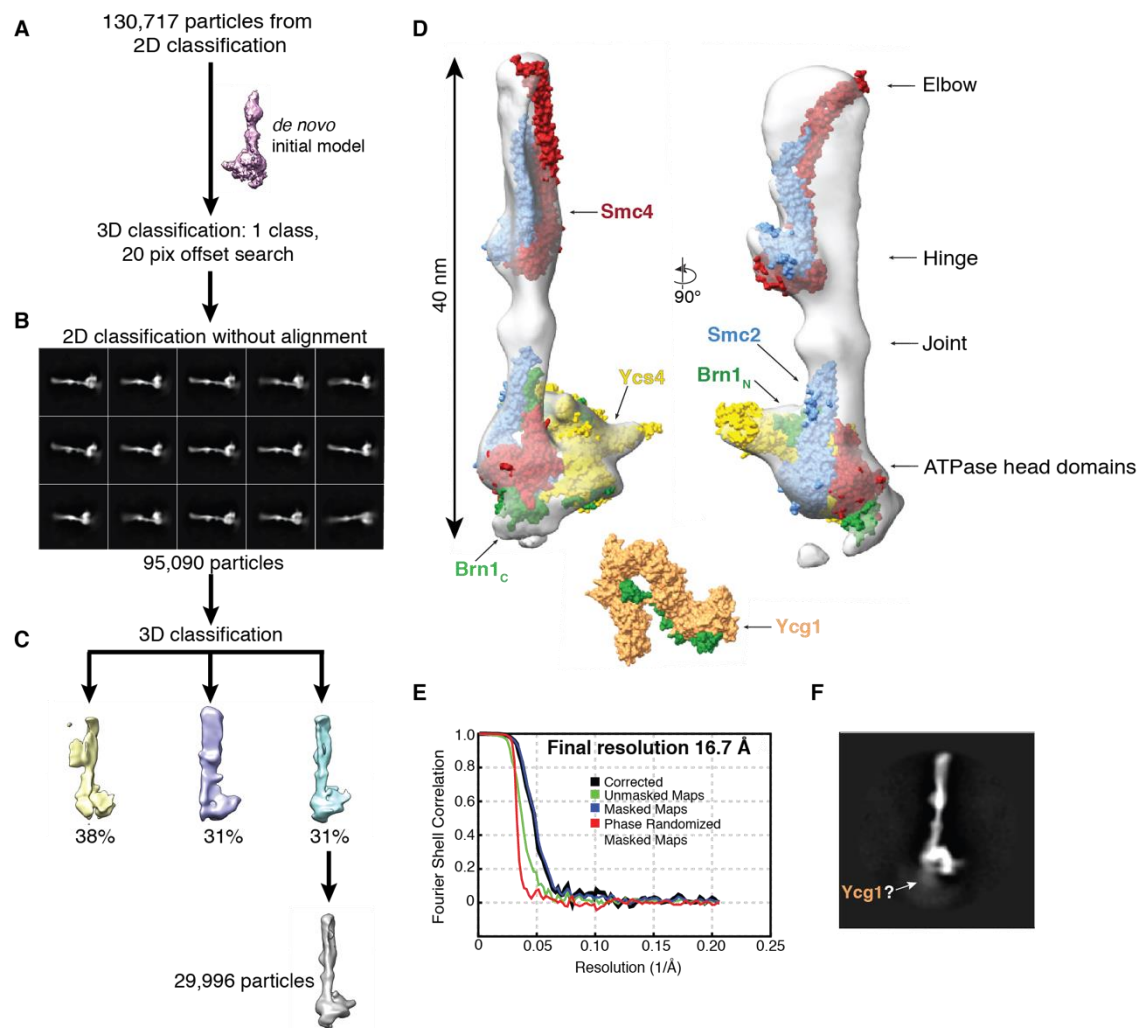


Figure 2.3: Processing workflow and structure of the entire particle. (A) 130,717 particles were aligned to a *de novo* initial model created in cryoSPARC by using 3D classification with an offset search of 20 pixels to compensate for off-center particles. (B) Angles from 3D classification were used to clean up the dataset further by 2D classification without image alignment. (C) 3D classification resulted in a distinct class that was refined and sharpened in Relion. Percentages indicate fractions of total particles. (D) Crystal structures of *Ct* Ycs4-Brn1_{Ycs4} with *Ct* Smc4_{hd}-Brn1_C (PDB: 6QJ4), *Sc* Ycg1-Brn1_{Ycg1} (PDB: 5OQQ), *Sc* Smc2-Smc4 hinge domain (PDB: 4RSI) and a model of *Ct* Smc2_{hd} (PDB: 6QJ1) with *Ct* Brn1_N (PDB: 6Q6E) were manually fitted into the cryo-EM density map. No density for Ycg1 was identified. (E) FSC plot of the cryo-EM map shown in (D). (F) Representative 2D class average displaying additional density below the head segment.

Ycg1-Brn1_{Ycg1} could not be placed into the density map. I did, however, observe additional fuzzy density close to the head segment in a few 2D class averages of the holo complex (Fig. 2.3F). It is thus conceivable that the Ycg1 subunit is only flexibly tethered to the rest of the complex through its interaction with the largely unstructured Brn1. Averaging of many particles, each with a different Ycg1 localization, would then lead to an absence of clear Ycg1 density in the averaged images. It cannot be

excluded, however, that the complex disintegrated partially during sample preparation. The above-mentioned hook-shaped particles that appeared in a few 2D class averages could hence represent Ycg1 alone (**Fig. 2.2D**).

2.2.1 The arm segment in absence of ATP

To improve the resolution of the coiled-coil arm segment, I used a focused refinement approach. Based on the map obtained for the entire complex, I re-centered particles on the arm segment and re-extracted particles in a smaller particle box.

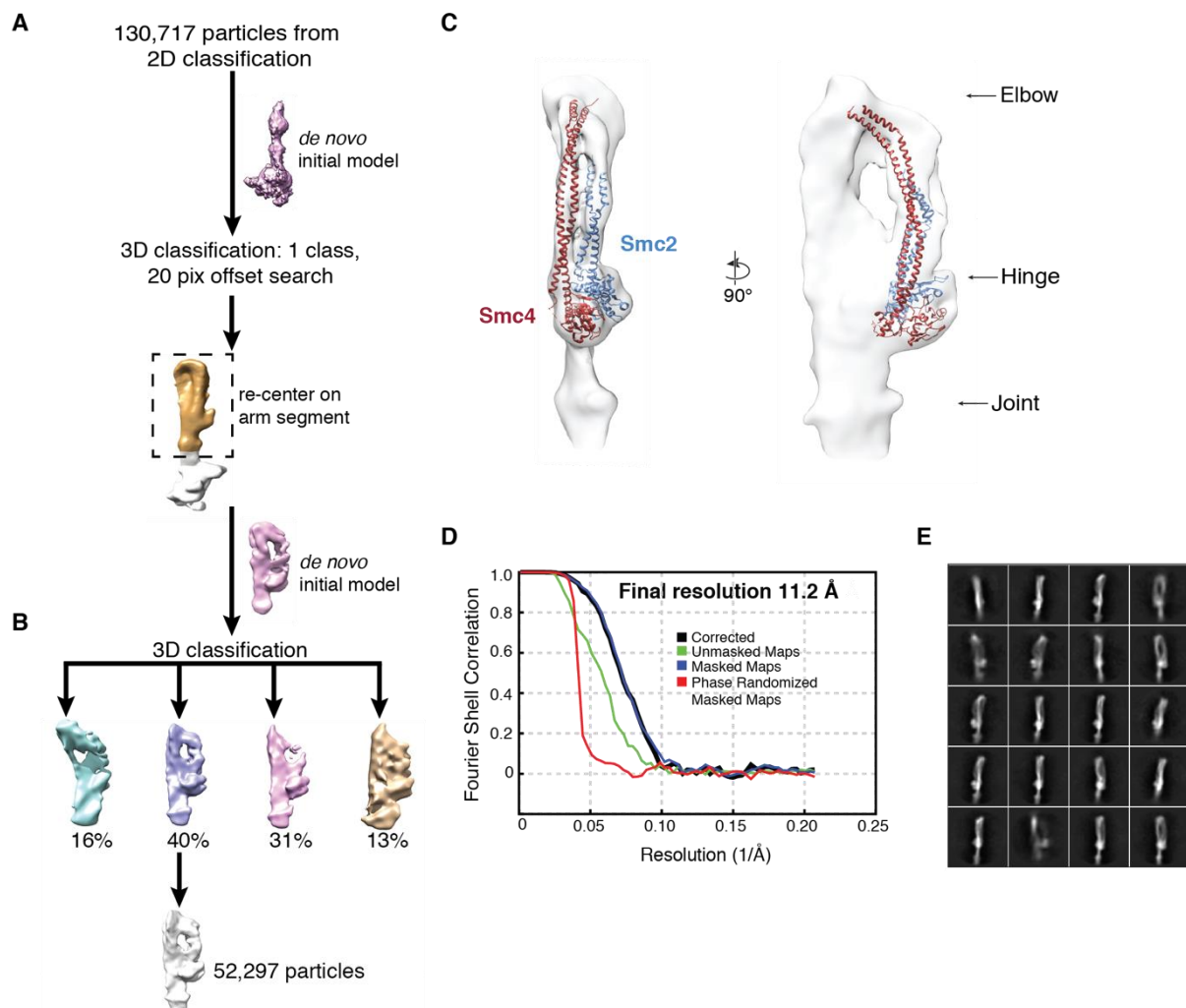


Figure 2.4: Focused refinement of the arm segment. (A) Starting from the single class as shown in Fig. 2.3, particles were re-centered on the arm segment and re-extracted. An initial model was created *de novo* using cryoSPARC. (B) The initial model was used as a reference for 3D classification with four classes. Percentages represent fractions of total particles. One class was further refined and sharpened. (C) Map of the arm segment with manually fitted Sc Smc2-Smc4 hinge (PDB: 4RSI) displaying a folded conformation where the hinge interacts with the coiled coils. (D) FSC plot of the map in (C). (E) Representative 2D class averages of the arm segment demonstrating the folded conformation.

After generating an initial model *de novo*, I subjected particles to 3D classification, which resulted in a distinct class that reached a resolution of 11.2 Å (**Fig. 2B, D**). This class confirmed that the hinge domain folds back onto the coiled coils (**Fig. 2.4C**). Due to the limited resolution, it remained unclear which part of the hinge domain interacts with which part of the coiled coils, although it appeared that the Smc4 half of the hinge is located closer to the coiled-coil density. The folded back hinge domain is also evident from 2D class averages of the arm segment (**Fig. 2.4E**).

2.2.2 The head segment in absence of ATP

I used the same focused refinement approach for the head segment (**Fig. 2.5A**). Surprisingly, a subsequent 3D classification resulted in two distinct classes (**Fig. 2.5B**). The first and major class (~76% of particles) showed high similarity to the head segment of the full particle. The improved resolution of 9.7 Å for the refined head segment allowed placement of the co-crystal structure of *Ct* Ycs4-Brn1_{Ycs4} in complex with *Ct* Smc4_{hd}-Brn1_c by rigid body fitting in UCSF chimera (Pettersen et al., 2004). In contrast, I had to place the *Ct* Smc2_{hd}-Brn1_N structure manually, since the density for this part of the complex was not as well preserved (**Fig. 2.5C**). This could indicate that the Smc2 head retains a certain degree of flexibility within the complex. Although biochemical data suggest that the Smc2 coiled coil immediately adjacent to the head domain binds the amino-terminal Brn1 helical domain (Onn et al., 2007), the density was insufficient to unequivocally address this notion.

Although no ATP had been provided during purification of the complex and sample preparation, the SMC heads were closely aligned, with only a gap of 2 nm separating their ATP binding sites. As a consequence, the Smc2 and Smc4 coiled coils aligned along their entire lengths. Due to this arrangement of Smc2 and Smc4, I will refer to this conformation as the '**zipped**' apo state.

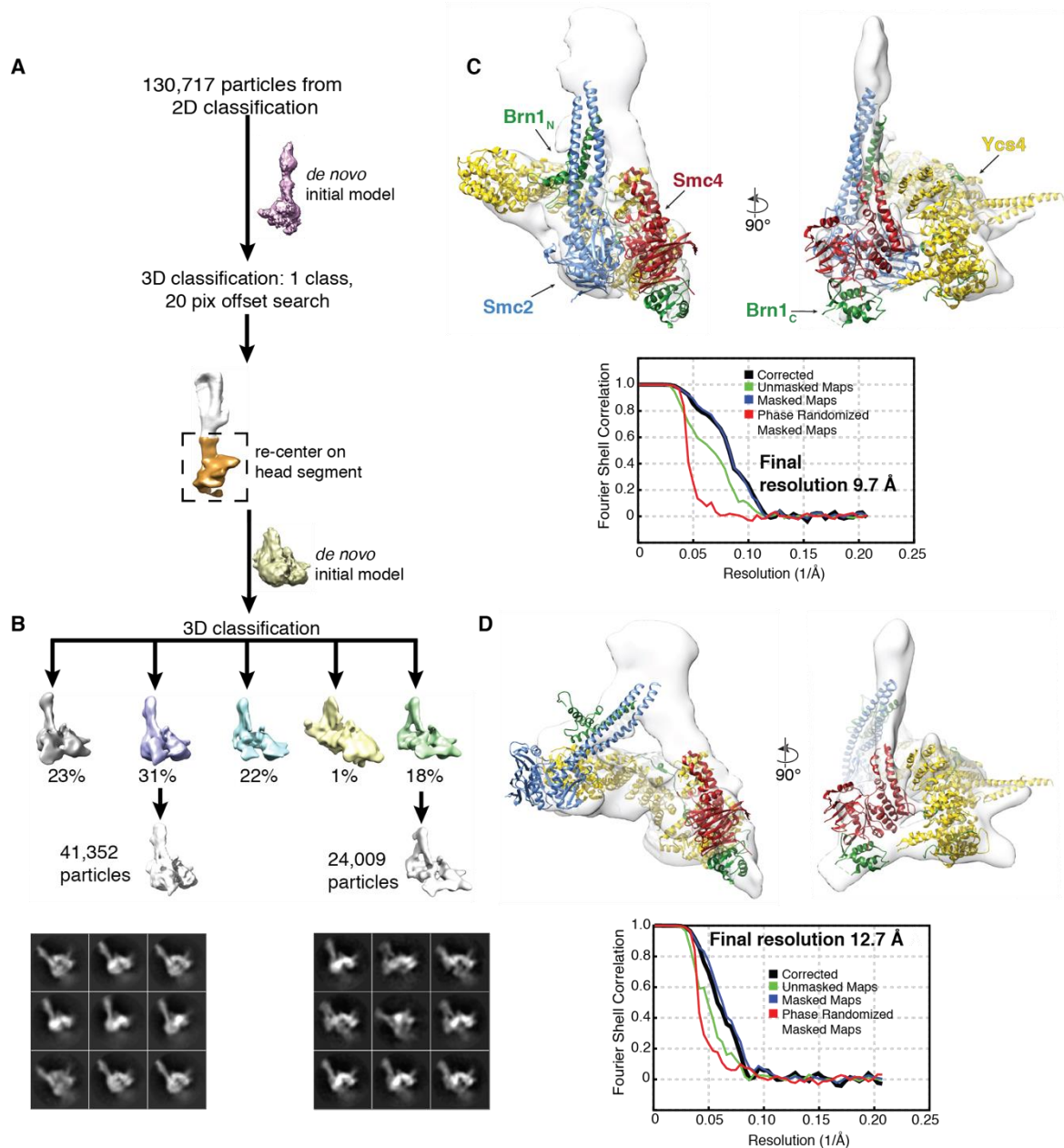


Figure 2.5: Focused refinement of the head segment. (A) Based on the map of the entire complex, particles were re-centered on the head segment and re-extracted. (B) An initial model was created *de novo* to serve as reference in a 3D classification with five classes. Percentages correspond to fraction of total particles. Two different classes were independently refined and sharpened. Representative 2D class averages of the two different classes are shown below. (C) Map of the major class (zipped apo state) with fitted crystal structures *Ct* Ycs4-Brn1_{Ycs4} bound to *Ct* Smc4_{hd}-Brn1_C (PDB: 6QJ4) and a model of *Ct* Smc2_{hd} (PDB: 6QJ1) with the *Ct* Brn1_N domain (PDB: 6Q6E) displayed closely aligned Smc2 and Smc4 head domains. FSC curves are shown below the map. (D) Map of the minor class (bridged apo state) with the same fitted structures as in (C) showed a separation of the Smc2 and Smc4 head domains. FSC plot is shown below.

I observed a different conformation in the second and minor class of particles (~18% of particles), which I will refer to as the ‘bridged’ apo state. Although the obtained resolution was lower for this state (12.7 Å) and the density remained partially

featureless, I was able to assign the Smc2 head domain to a different location when compared to the zipped state (**Fig. 2.5D**). In the bridged state, the Smc2 head domain bound to the amino-terminal end of Ycs4, while Smc4 remained bound to the carboxy-terminal half of Ycs4. Ycs4 hence bridges the two head domains. Interconversion of the zipped into the bridged state would require substantial structural rearrangements further up in the coiled coils. At the available resolution, however, it remained unclear where exactly such an rearrangement takes place in the coiled coils.

In conclusion, the newly described architecture of the condensin complex is different from how condensin or other eukaryotic SMC proteins have been envisioned. First, at least in the absence of ATP, condensin adopts a rod-like instead of a ring-like shape. Second, the hinge domain folds back onto the coiled coils, resulting in a reduction of the overall extension of the complex from the reported length of ~50 nm to ~40 nm (Terakawa et al., 2017). Third, condensin adopts at least two different states in the absence of nucleotide, the zipped and the bridged apo states.

2.3 Improved structure of the apo state of condensin

In order to improve the overall resolution of the apo condensin complex, I plotted the angular distribution of the particles onto the density map (**Fig. 2.6**). As already suspected from 2D class averages (see **Fig. 2.3B**, **Fig. 2.4D**, **Fig. 2.5B**), particle orientation was highly biased toward a single dominant side view, which possibly limits the resolution during 3D reconstruction (Baldwin and Lyumkis, 2020).

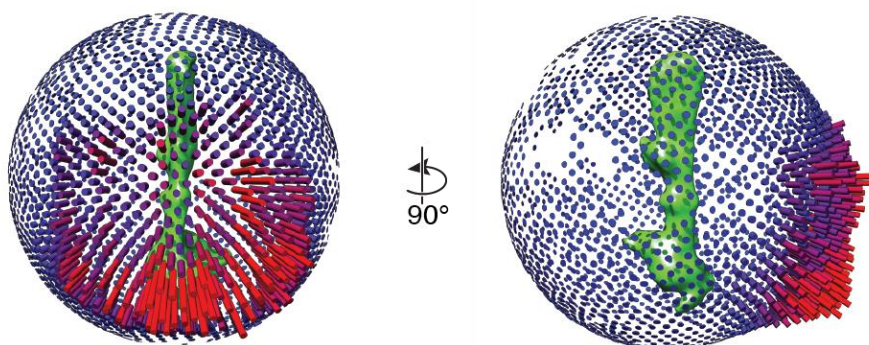


Figure 2.6: Angular distribution of the particles. Particles plotted based on their orientation. Column size and color (red = more particles) indicates number of particles in a given angle. Corresponding particle map is depicted in green.

Non-uniform particle orientation within the thin layer of a vitrified ice is a common problem in cryo-EM (Noble et al., 2018). Often, the preferred orientation is caused by the interaction of the particle with the air-water interface (Noble et al., 2018; Taylor and Glaeser, 2008). To overcome the influence of the air-water interface, I screened a wide range of buffer conditions that affect surface charges, including different salt concentrations, varying blotting parameters, changes in buffer components and pH, additives like glycerol or trehalose, multiple detergents or mild crosslinking. None of the tested conditions appeared to affect the preferred orientation.

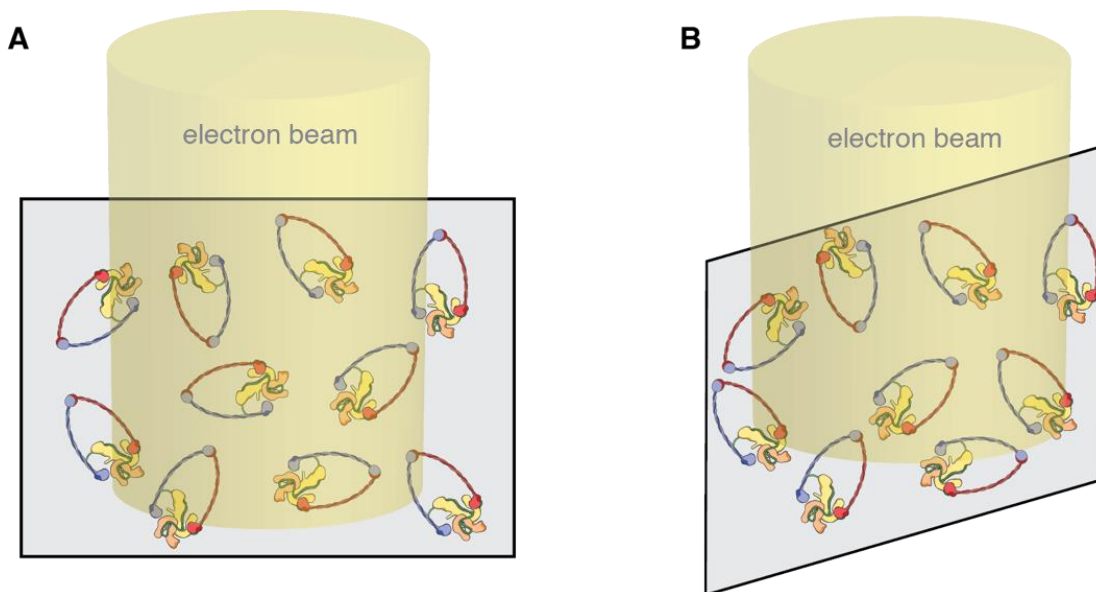


Figure 2.7: The effect of stage tilting. (A) Particles have a preferred orientation on the cryo-EM grid due to a possible interaction with the air-water interface and display the same sideview. Particles can, however, still rotate freely in the plane parallel to the stage (grey square). In conventional single particle analysis, the stage is not tilted for image acquisition. (B) Tilting the stage exposes particles to the electron beam (yellow) from different angles because of their rotation in the plane parallel to the stage. This leads to an improved angular coverage.

To nevertheless collect images of the condensin particles from at least slightly different angles, I acquired parts of a dataset after tilting the stage by 38° (**Fig. 2.7A**). Stage tilting had previously been demonstrated to restore different views of a particle, which then improved 3D reconstruction (Tan et al., 2017). Unlike in cryo-EM tomography, where the stage is being tilted continuously to acquire a tomogram, the stage is usually only tilted to a single specific angle for single particle analysis (SPA).

A single tilt angle can improve angular coverage because, even if particles preferably adopt only one specific side view as is the case for condensin, the particles can still

rotate freely in the plane of the stage (**Fig. 2.7B**). Hence, upon tilting the stage, particles are exposed to the electron beam in a range of different angles. The tilt angle was computationally determined by using cryoEF (Naydenova and Russo, 2017), a program that quantifies the orientation bias based on the angular distribution of particles in the refined map.

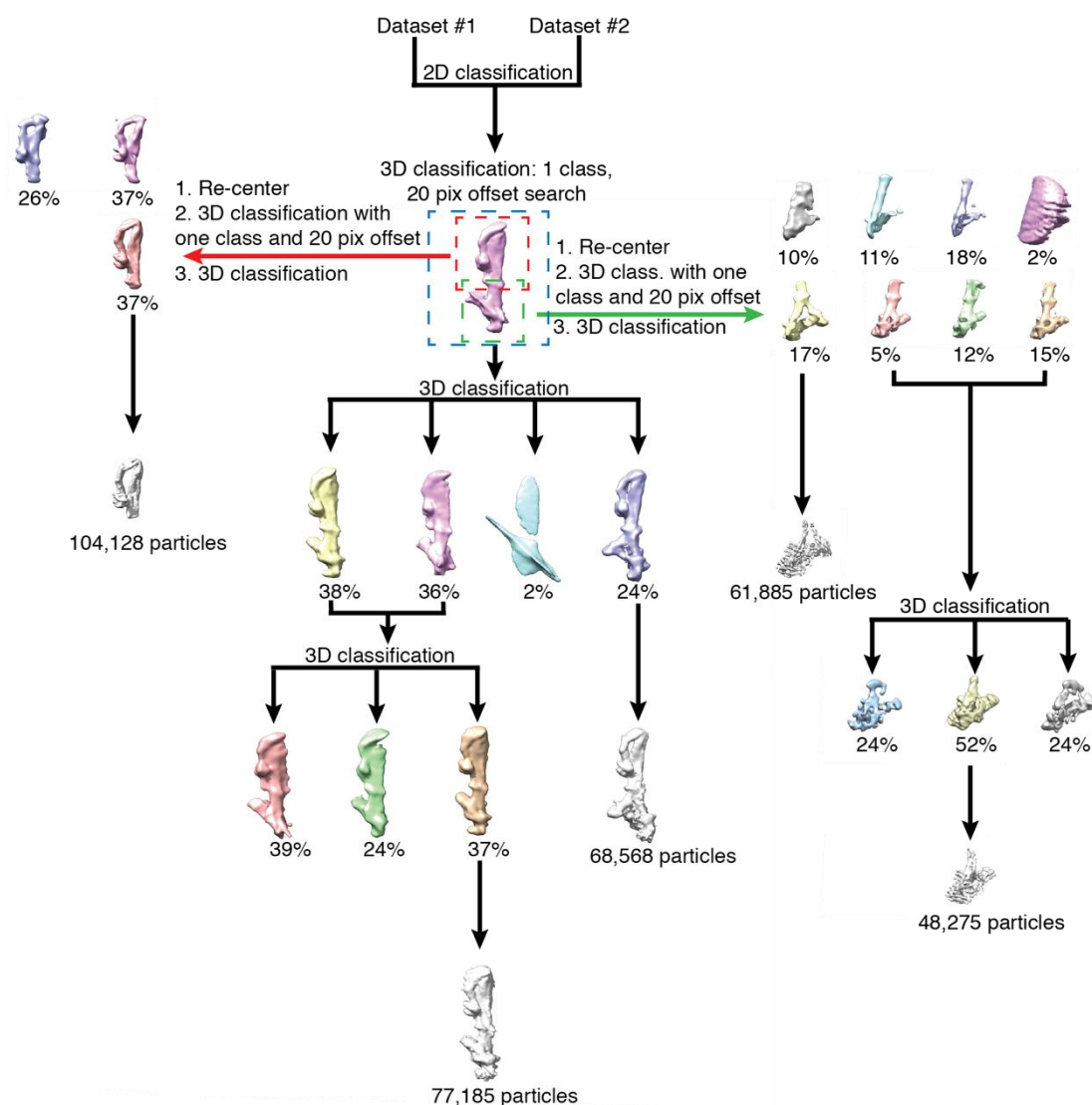


Figure 2.8: Processing workflow after stage tilting in absence of ATP. Two datasets were pre-processed independently and then cleaned up by several rounds of 2D classification to exclude obvious 'junk' particles. Particles from both datasets were merged and a *de novo* initial model was created to align all particles into one class with an offset search of 20 pixels to compensate for off-center particles. Based on this 3D map, particles were re-centered on the arm segment (left), the head segment (right), or processed as full particles (middle). Additional rounds of 3D classifications with indicated percentages of total particles led to the five final maps (from left to right: Arm segment, full particle in the zipped state, full particle in the bridged state, head segment in the zipped state, head segment in the bridged state) with corresponding number of particles.

To additionally increase the particle number, two datasets were acquired with a tilted stage and combined after pre-processing. I processed the datasets in a similar way

as described above. After particle picking and clean-up, I used 3D classification with an offset search of 20 pixels to center all particles and align them into a single class. As described above, this step was implemented to center particles properly. To refine a homogenous set of particles, a second round of 3D classification, this time with multiple classes, was used. Simultaneously, I re-centered particles on arm and head segments and re-extracted them to improve the resolution (**Fig. 2.8**).

2.3.1 Structure of the entire particle

For the full particle, the resolution improved by ~ 5 Å for the zipped apo state (**Fig. 2.9A**). This improvement allowed the identification of clearly discernible features like the folded hinge, the joint region, the proboscis of the Ycs4 subunit, or the additional density below the heads possibly corresponding to Ycg1. Furthermore, the improved data quality confirmed the existence of the previously postulated bridged apo state, with clear densities for both, Smc2 and Smc4 head domains (**Fig. 2.9B**). This also revealed that the coiled coils split apart at their joint regions in the bridged apo state. The joint represents a break in the otherwise mostly continuous helical coiled coils. It is conceivable that this break allows sufficient flexibility for the ATPase heads to move apart, while maintaining a seemingly identical coiled-coil arm conformation above the joint. In both, the zipped as well as the bridged apo states, particle orientation, albeit still favoring one view, displayed a more even distribution therefore covering more angles and possibly facilitating 3D reconstruction (**Fig. 2.9C**).

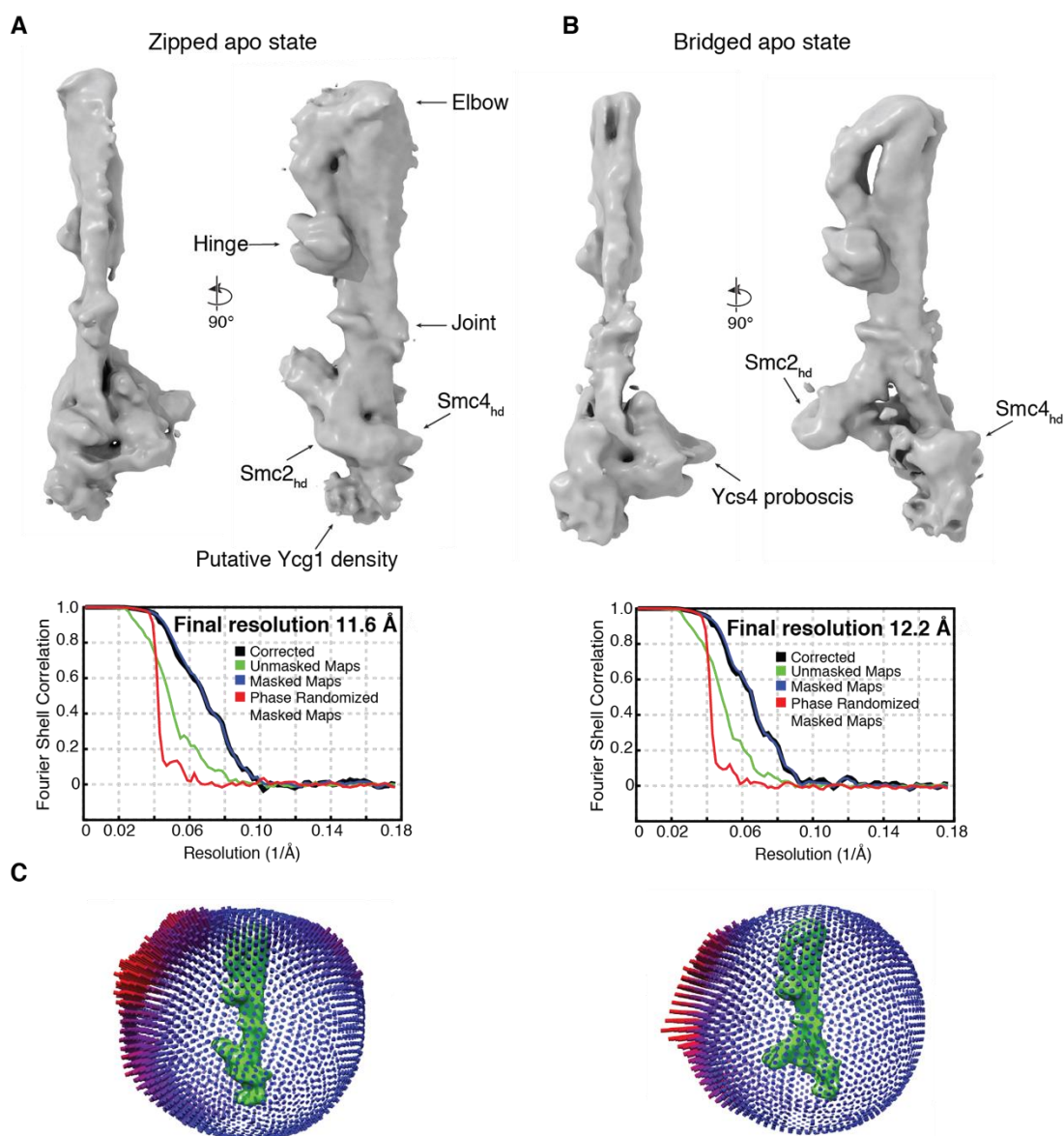


Figure 2.9: Entire particle after stage tilting. (A) Cryo-EM density map of the zipped apo state with indicated structural features highlighting closely aligned Smc2 and Smc4 head domains, an overall rod-like shape, and a folded hinge conformation. The corresponding FSC plot is shown below. (B) Cryo-EM density map of the bridged apo state displayed a separation of the Smc2 and Smc4 head domains compared to the zipped state. Corresponding FSC plot is shown below. (C) Angular distribution of particles for the zipped state (left) and the bridged state (right). Size and color (red = more particles) of the columns represent the number of particles.

2.3.2 Focused refinement of the arm segment

Similar to the entire particle, focused refinement and sharpening of the arm segment improved the resolution to 8.4 Å. At this resolution, single helices of the coiled coils close to the hinge became discernible (**Fig. 2.10A**). Fitting of the *S. cerevisiae* hinge crystal structure with proximal coiled coils (PDB: 4RSI) produced a near-perfect match

for the hinge domain itself, the coiled coils, especially the coiled coil of Smc4, were slightly misplaced (**Fig. 2.10B**). A different coiled-coil angle in the crystal structure could be the result of forces during crystal packing, or of additional constraints in the context of the holo complex acquired by cryo-EM.

Tracing the coiled coils to the ATPase heads indicated that the hinge domain contacts only the Smc2 coiled coil. Together with the hinge arrangement, this suggests that the interaction between hinge and coiled coils is only mediated by the Smc4 half of the hinge domain and the Smc2 part of the coiled coils (**Fig. 2.10C**).

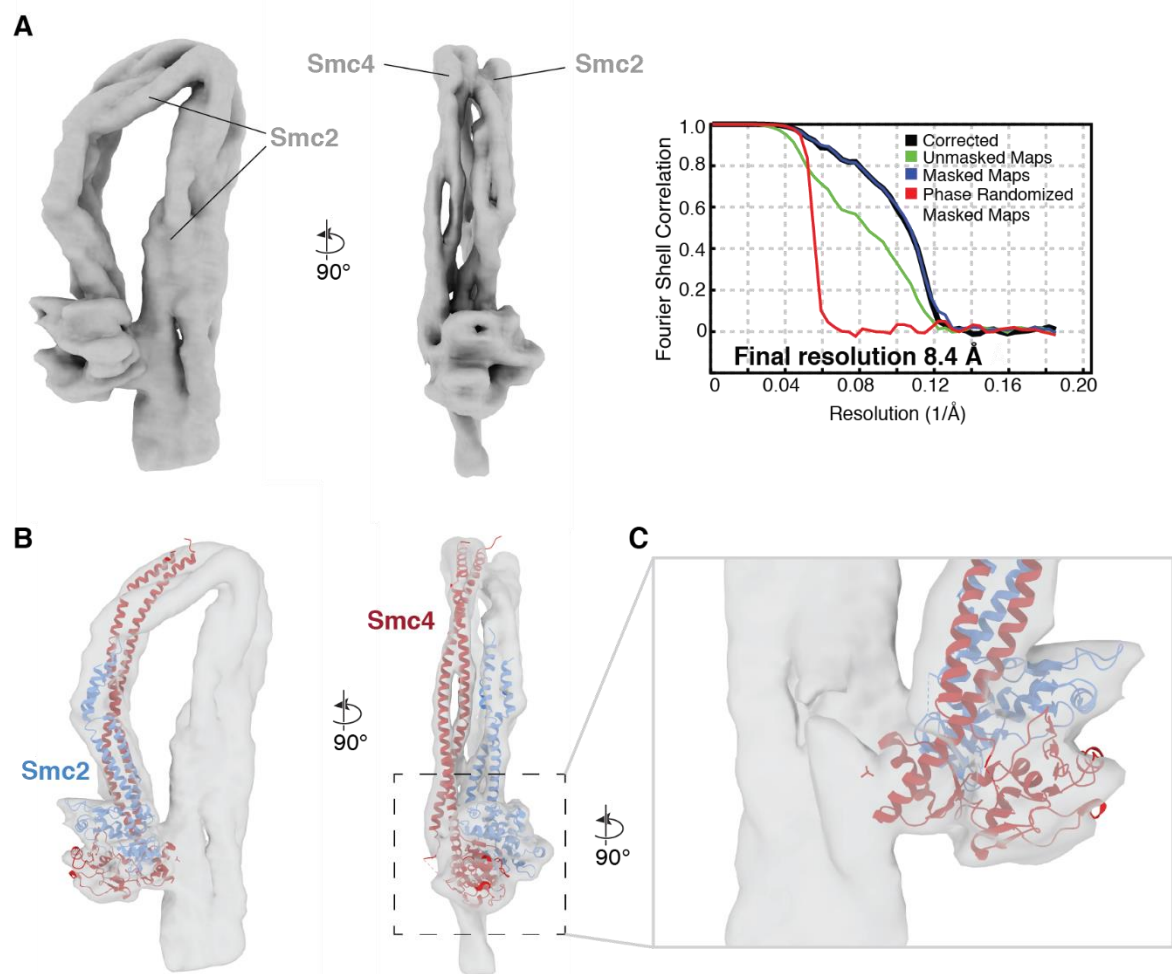


Figure 2.10: Arm segment after stage tilting. (A) Cryo-EM density map of the arm segment in absence of ATP demonstrated that only the Smc2 coiled-coil is contacted by the hinge domain. FSC plot is shown on the right. (B) Rigid body fitting of the *S. cerevisiae* hinge domain with proximal coiled coils (PDB: 4RSI) into the cryo-EM density map from (A). (C) Interaction site between the hinge domain and the coiled coils suggests that the interaction is mediated by the Smc4 half of the hinge and the Smc2 coiled-coil.

2.3.3 Focused refinement of the head segment

Focused refinement of the head segment confirmed the existence of two distinct zipped (~70% of particles) and bridged (~30% of particles) apo states in absence of ATP.

For the zipped state, tilting the stage and increasing the number of particles resulted in a density map of 7.4 Å resolution, which revealed clearly defined alpha helices (**Fig. 2.11A, Fig. 2.11G**). Due to its high number of alpha helical repeats, the density for the Ycs4 subunit with its interacting Brn1 fragment was of sufficient quality to allow rigid body docking of the co-crystal structure of *Ct* Ycs4-Brn1_{Ycs4} in complex with *Ct* Smc4_{hd}-Brn1_C (**Fig. 2.11B**). This confirmed the recently discovered Smc4-Ycs4 interaction (Hassler et al., 2019). I then manually placed a model for the *Ct* Smc2_{hd}-Brn1_N subcomplex, since rigid body docking failed despite of sufficient density for the coiled coils, the amino-terminal Brn1 helical motif and the Smc2 head domain (**Fig. 2.11C**).

SMC head domains are composed of a 'helical' lobe, which extends into the coiled coils, and a RecA-like lobe, which contains the ATP binding site (Hopfner and Tainer, 2003). Interestingly, I could either match the 'helical' or the RecA-like lobe with the cryo-EM density, but not both lobes simultaneously. A possible explanation can be found when comparing the Smc2 crystal structure with the structures of other homologous SMC heads, like the cohesin Smc3 subunit. In the Smc3 crystal structure, the angle between the RecA-like lobe and the helical lobe is smaller than in the Smc2 crystal structure (**Fig. 2.11D**). Indeed, Smc3-Scc1_N fitted better into the cryo-EM density than Smc2-Brn1_N (**Fig. 2.11E**).

The improved cryo-EM density map of the zipped head segment confirmed that the heads are closely aligned in this state and would require only minor structural rearrangements to form a fully engaged head dimer upon ATP binding (**Fig. 2.11F**).

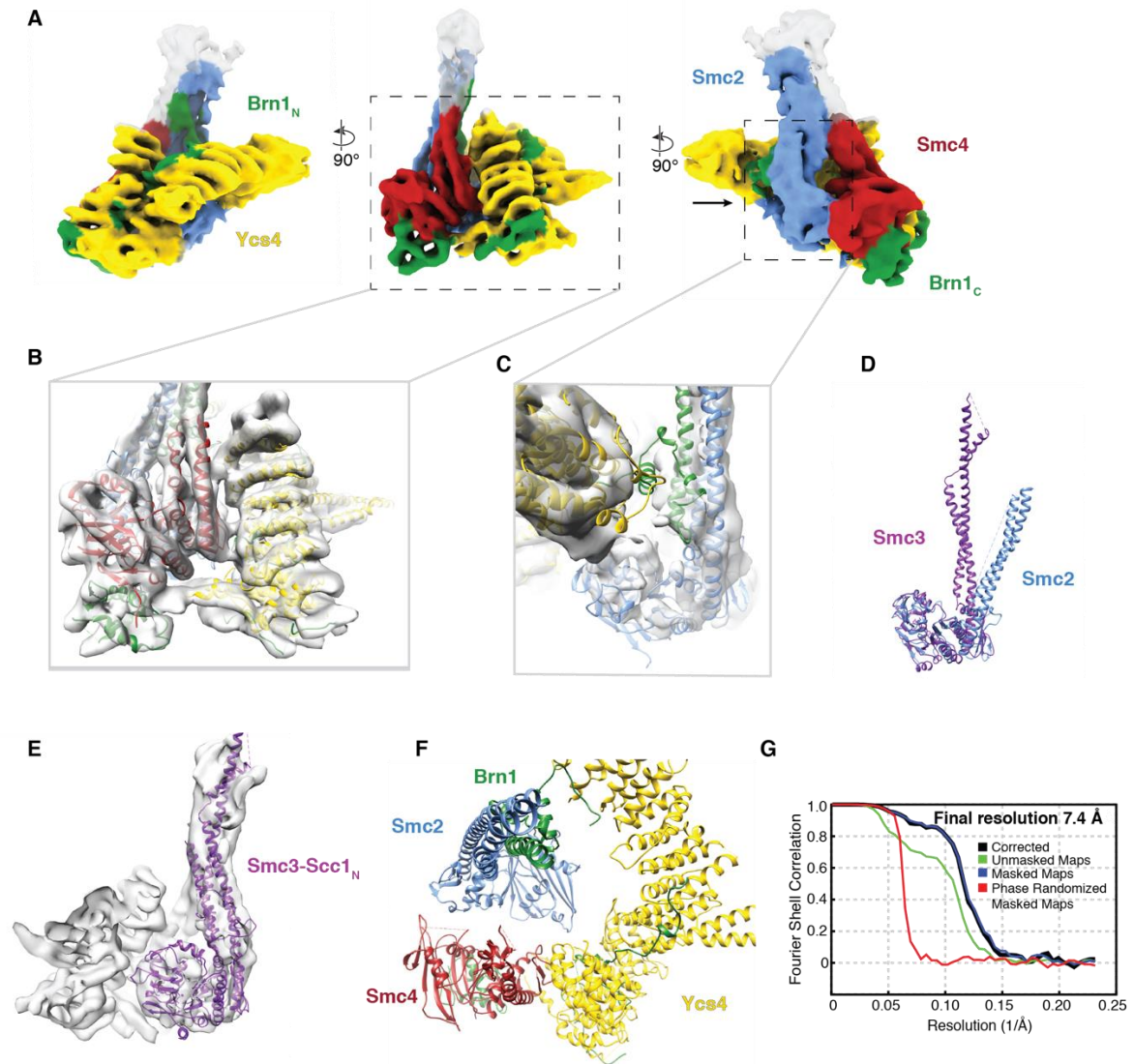


Figure 2.11: Head segment of the zipped apo state after stage tilting. (A) Cryo-EM density map of the head segment with rigid body fitted crystal structure of *Ct* Ycs4-Brn1_{Ycs4} bound to *Ct* Smc4-Brn1_C (PDB: 6QJ4) as well as a manually placed model of *Ct* Smc2_{hd} (PDB: 6QJ1) bound by Brn1_N (PDB: 6Q6E). (B) Highlight of the high accordance between cryo-EM density map and crystal structures of Smc4 and Ycs4. (C) The RecA-like lobe of Smc2 (left part of the Smc2 head domain) only partially matched with the cryo-EM density while the helical part (right part of Smc2) displayed a good fit. (D) Superimposition of *Ct* Smc2 (PDB: 6QJ1) and the homologous *Sc* Smc3 (PDB: 4UX3) shows a difference in the angle between helical part and RecA-like lobe. (E) Rigid-body fitting of the *Sc* Smc3-Scc1_N crystal structure (PDB: 4UX3) into the cryo-EM density map from (A) yielded an improved fit compared to Smc2. (F) Top view of the pseudoatomic model of the zipped apo state reveals closely aligned Smc2 and Smc4 head domains. (G) FSC curve corresponding to the cryo-EM density map in (A).

I observed a similar improvement in map quality for the bridged apo state, which could now be resolved to 8 Å (Fig. 12A, Fig. 12D). Again, electron density for the Ycs4 subunit and Smc4 head was well preserved and accommodated the respective crystal structures. In contrast, fitting of the Smc2 head faced the same problems as for the

zipped apo state (**Fig. 12B**). Nonetheless, clear additional density next to the two Smc2 coiled coils suggested that the Brn1 amino terminus remained bound in the bridged apo state, which is in line with published results that suggested a release of Brn1_N only upon addition of ATP (Hassler et al., 2019). Unlike in the zipped apo state, Smc2 and Smc4 head domains were separated by ~10 nm in the bridged apo state. A transition from one to the other state would require considerable flexibility in the coiled coils. This flexibility might be provided by structural changes in the joint region, where the coiled coils start to split apart in the bridged apo state (**Fig. 2.9B**). It is important to note that this movement takes place in the absence of ATP.

2.4 High-resolution structures of condensin in absence of ATP

While solving the improved structures of the condensin apo complex, the group of Jan Löwe at the MRC LMB independently solved the structure of the *S. cerevisiae* condensin complex in its ATP-free state.

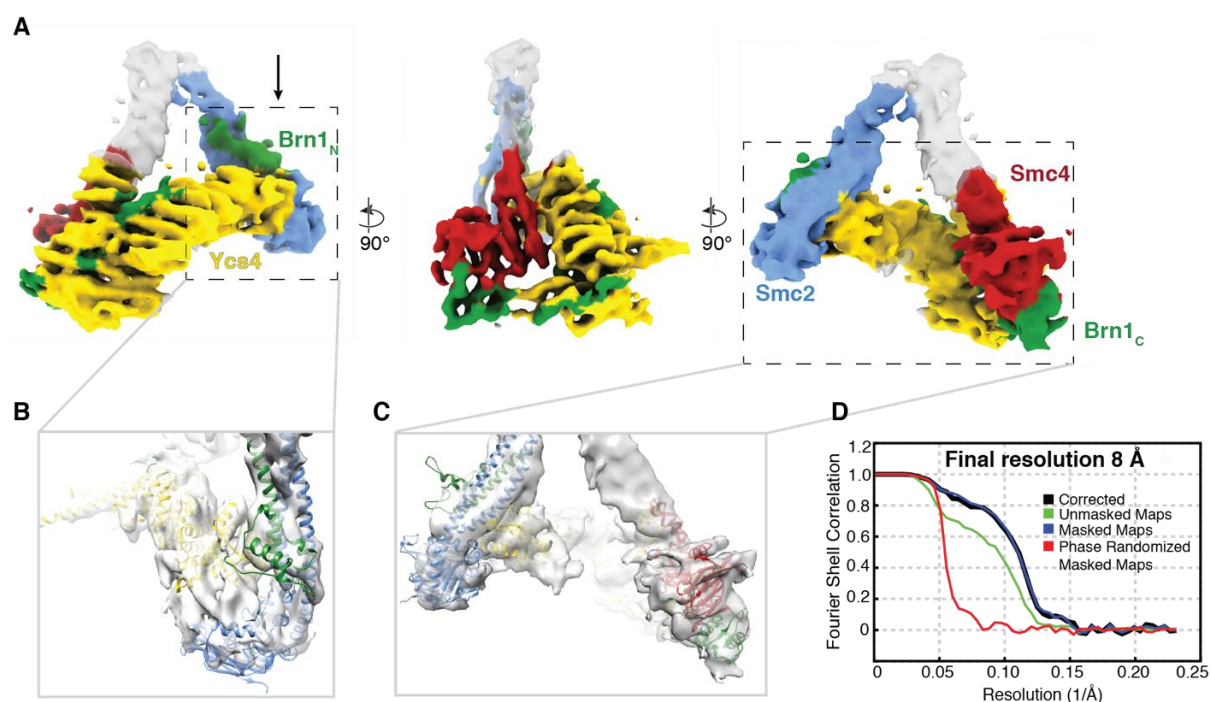


Figure 2.12: Head segment of the bridged apo state after stage tilting. (A) Cryo-EM density map of the head segment with rigid body fitted crystal structures of *Ct* Ycs4-Brn1_{Ycs4} bound to *Ct* Smc4-Brn1_C (PDB: 6QJ4) as well as a manually placed model of *Ct* Smc2_{hd} (PDB: 6QJ1) bound to *Ct* Brn1_N (PDB: 6Q6E). (B) Top view of the Ycs4-Smc2 interaction interface highlighting poor accord of the Smc2 crystal structure and cryo-EM density similar to what was previously observed for the zipped state. (C) Sideview of the bridged Smc2 and Smc4 head domains with separation of coiled coils. (D) FCS curve corresponding to the cryo-EM map in (A).

Using a combination of phase-plate acquisition, stage tilting, imaging condensin complexes that lacked the Ycg1 subunit and a total of 12 merged datasets that resulted in ~34,000 micrographs, the group obtained density maps at 8.1 Å resolution for the entire particle and at 5.5 Å or 4.2 Å for the arm or head segments, respectively (Lee et al., 2020). This allowed modeling of the entire holo complex in its zipped (**Fig. 2.13A**) and bridged (**Fig. 2.13B**) apo states based on available crystal structures. These data independently confirmed the overall rod-like structure, interaction of the Smc4 half of the hinge with the Smc2 coiled coil and positions of the head domains in the zipped and bridged apo states. As described above, the high resolution condensin map did also not fit to the Smc2 crystal structure and therefore Byung-Gil Lee and colleagues used a homology model of the *Sc* Smc2_{hd}-Brn1_N subcomplex based on the cohesin *Sc* Smc3_{hd}-Scc1_N crystal structure (PDB: 4UX3).

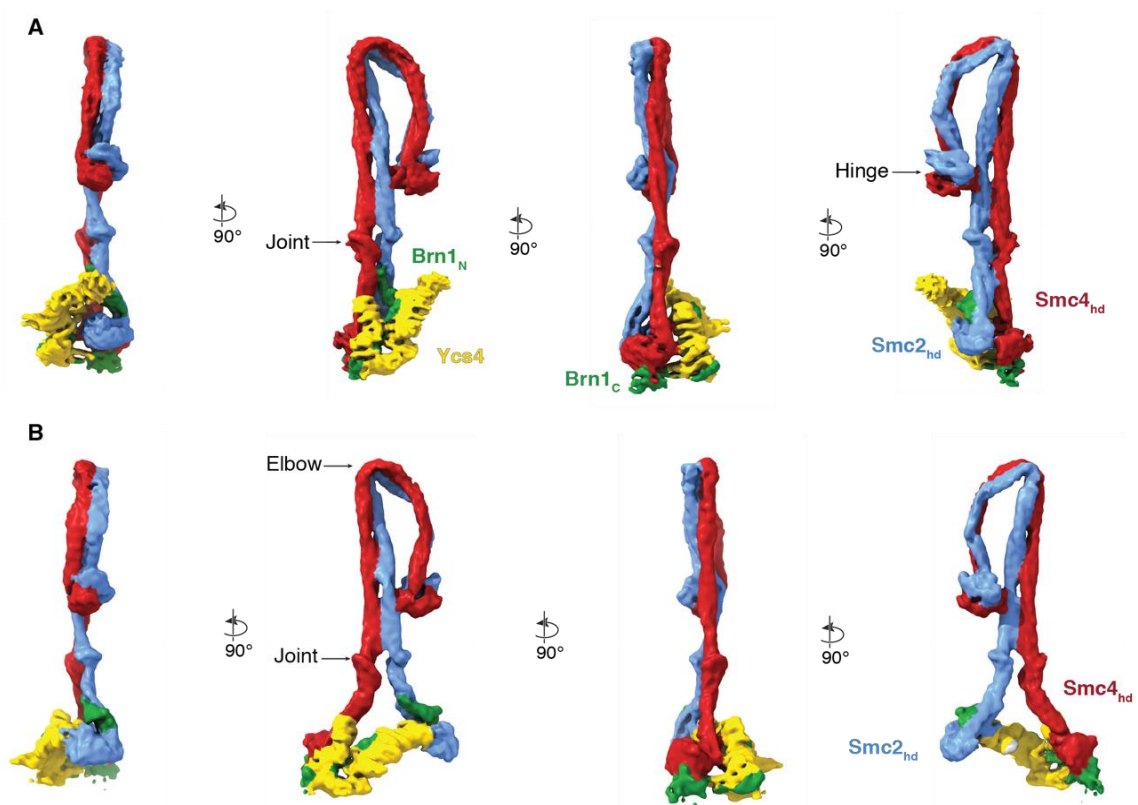


Figure 2.13: High resolution cryo-EM maps of the apo state. (A) Cryo-EM density map of the zipped apo state with highlighted structural features independently confirming the rod-like shape, the close alignment of the Smc2 and Smc4 head domains and the folded conformation. Map was colored based on a pseudo-atomic model (PDB: 6YVU). (B) Cryo-EM density map of the bridged apo state with highlighted structural features. Map was colored based on a pseudo-atomic model (PDB: 6YVV). Data was acquired and processed by Byung-Gil Lee.

Since Byung-Gil Lee and I obtained basically identical results, we decided to focus on the high-resolution data. In the following discussion, I will refer to this data when analyzing the condensin apo states.

2.5 Comparison of the zipped and bridged apo states

Comparing the pseudo-atomic models obtained for the zipped and bridged apo states showed that the Smc2 and Smc4 heads are only ~2 nm apart in the former state and then separate to a distance of ~10 nm in the latter state. This movement is caused by a 50° wedge formation between the coiled coils of Smc2 and Smc4 (**Fig. 2.14A**).

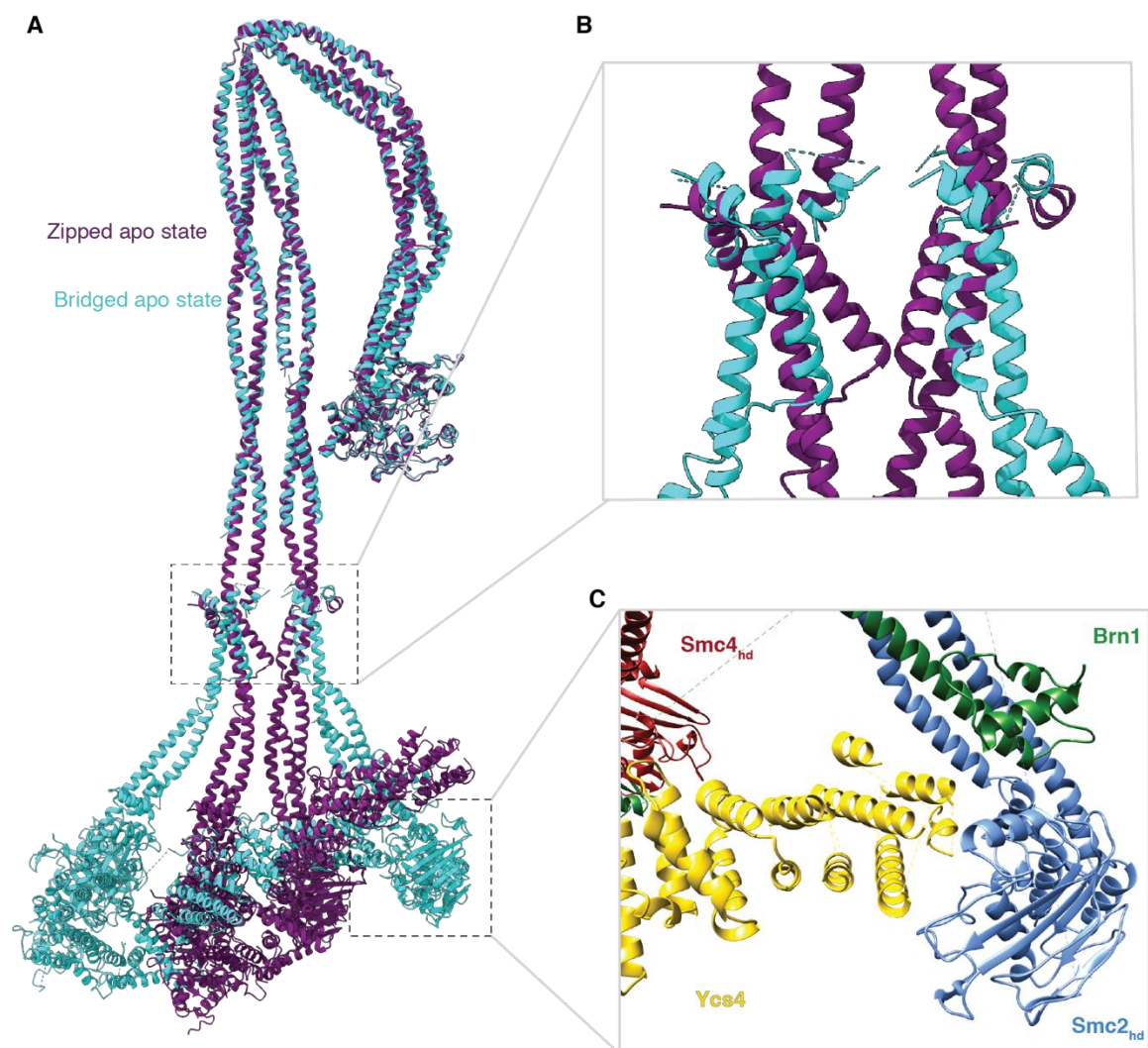


Figure 2.14: Comparison of the bridged and zipped apo states. (A) Superimposition of the zipped and the bridged apo states of condensin in absence of ATP (Panel from Lee et al., 2020). (B) Highlighting the superimposed joint region in the zipped and bridged apo states revealed that the transition from zipped to bridged apo state is enabled by the discontinuity of the coiled coils in the joint region. (C) Interaction interface of Smc2 and the amino-terminus of Ycs4 in the bridged state.

The wedge in the coiled coils is stabilized by the amino terminus of Ycs4, which interacts with the Smc2 head domain close to the ATP binding site (**Fig. 2.14B**). Interestingly, it appears to be only a small region, namely the joint, a region of previously unknown function, that enables this flexibility in the coiled coils and allows the two heads to drift apart (**Fig. 2.14C**).

2.6 Structure of condensin in presence of ATP

To learn more about the catalytic mechanism of the condensin ATPase and its accompanying structural rearrangements, I plunge froze *S. cerevisiae* condensin complexes in the presence of an equimolar mix of ATP and its non-hydrolysable analogue AMP-PNP. Initial datasets revealed again a strong preferred particle orientation, which impaired 3D reconstruction (data not shown). To address this issue, I acquired two datasets at a tilt angle of 30°. After pre-processing, I merged particles from both sets and subjected them to several rounds of 2D classification as described for the apo complexes. The final round of 2D classifications displayed a high amount of heterogeneity compared to the rather uniformly appearing particles imaged in the absence of ATP (compare **Fig. 2.15** and **Fig. 2.2D**). Although different orientations in 2D can be misinterpreted, I nevertheless identified several distinct classes. Three of these classes (purple, orange and teal in **Fig. 2.15**) looked similar to the classes of the apo states of condensin with respect to the coiled coils. They showed a rod-like appearance with a folded-back hinge domain. The head segment, however, displayed markedly different conformations, ranging from complete disorder, presumably as a consequence of flexibility (purple), to some flexibility around the heads (orange) to a well-defined head segment, which looked different to the head segments of the apo states (teal). The fourth class (green), on the contrary, displayed a high degree of flexibility in the coiled-coil segment, which suggested that the rod-like coiled-coil confirmation might have been lost (**Fig. 2.15**).

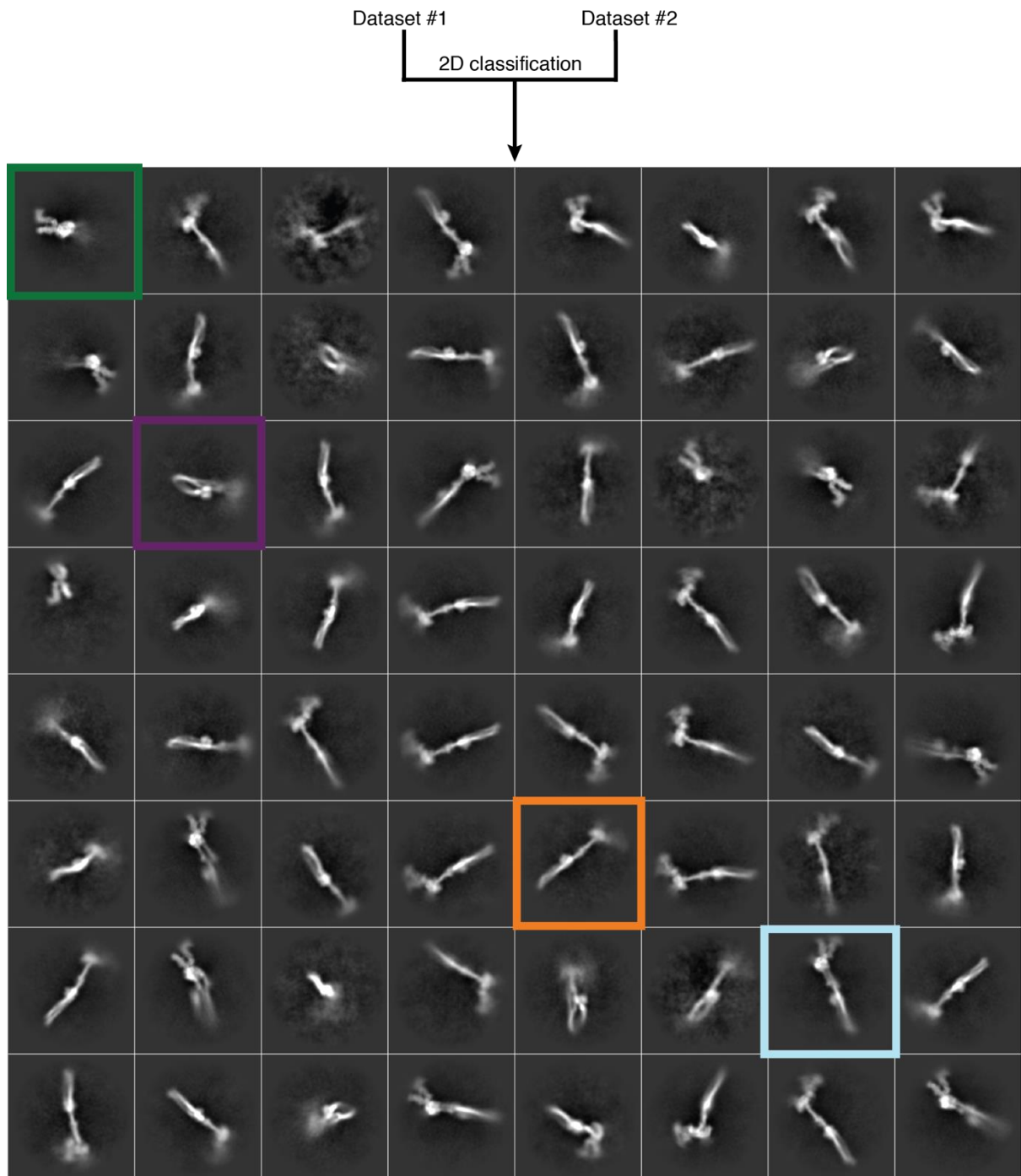


Figure 2.15: Heterogeneity of condensin particles upon addition of ATP. Two datasets of *Sc* condensin holo complexes were acquired in presence of ATP after stage tilting. Particles were merged after independent pre-processing. Particles were cleaned up through several rounds of careful 2D classification. Representative 2D averages of the last round are shown highlighting the structural heterogeneity. Four major classes were observed displaying highly flexible coiled coils and a clearly visible head segment (green box), rod-shaped coiled coils and a clearly visible head segment (teal box), rod-shaped coiled coils with fuzzy density around the head domains (orange box) or an entirely fuzzy head segment with rod-shaped coiled coils (purple box).

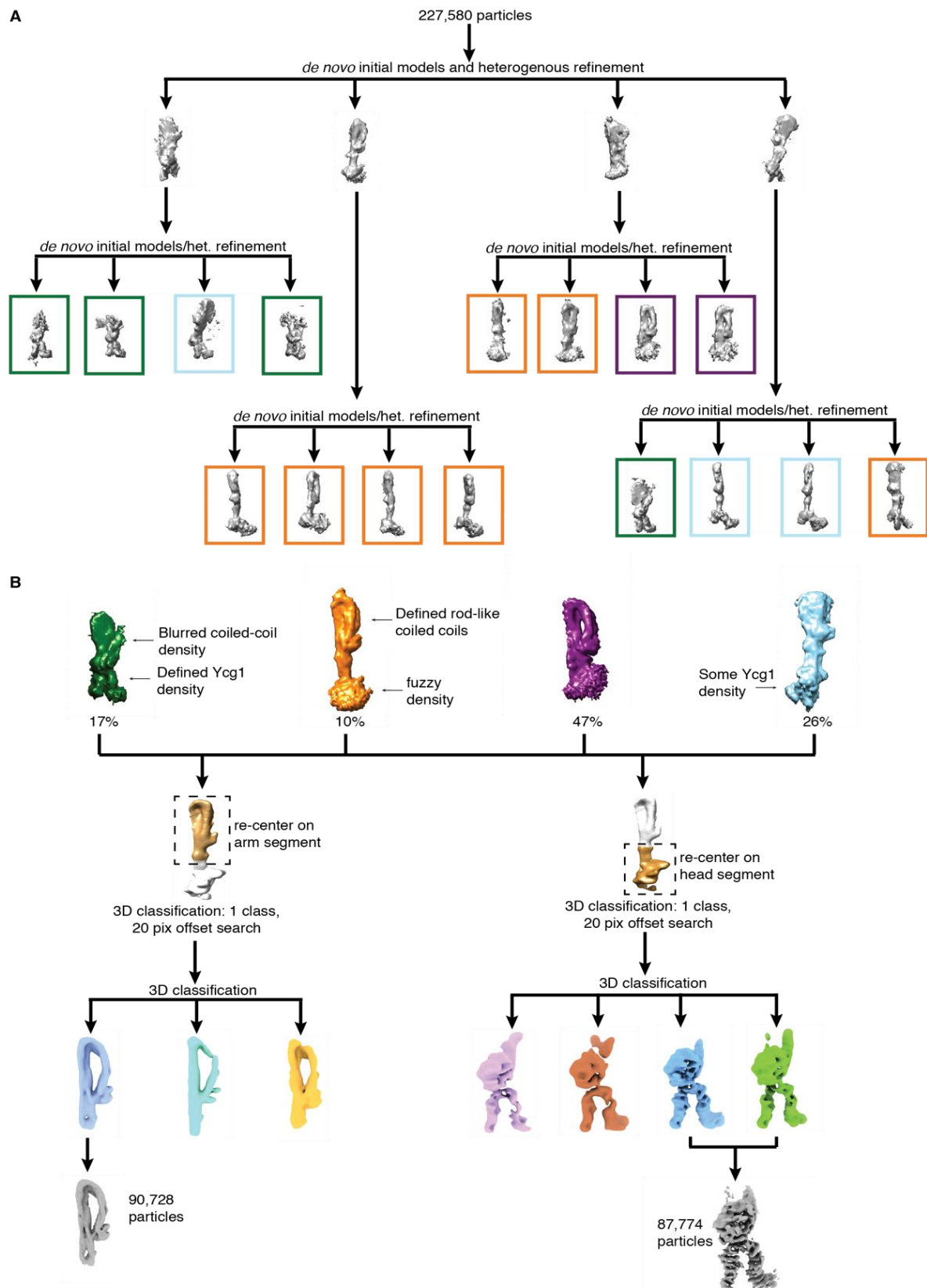


Figure 2.16: Processing workflow of the +ATP datasets after stage tilting. (A) Particles were cleaned up by careful 2D classifications (see Fig. 2.15) resulting in a total of 227,580 particles. To address heterogeneity within the dataset, particles were divided into four classes in a template free manner. Each of the four classes was then further divided into another four classes in a template free manner resulting in a total of 16 classes. Upon visual inspection particles from similar classes (colored boxes) were pooled and refined independently. (continued on next page)

(B) The final four cryo-EM density maps with labeled structural features and percentage of total particles. Based on the four maps, particles were either re-centered on the arm (left) or the head segment (head) for focused refinement. In both cases, an initial model was created *de novo* to align the particles into one class with an offset search of 20 pixels. As previously described, this step was introduced to account for off-center particles. A second round of 3D classification was performed to identify classes suitable for refinement and sharpening resulting a cryo-EM density map for the arm segment and the head segment with indicated number of particles.

Due to the high amount of heterogeneity within the dataset, I modified the processing workflow. After carefully removing contaminations and broken particles by 2D classification, I divided the remaining particles into four initial models in a template-free approach (Fig. 2.16A). I repeated this process with each of the four classes to generate 16 classes in total (Fig. 2.16B). Upon visual inspection, I pooled particles from similar classes and refined them independently, giving rise to four rough 3D reconstructions (Fig. 2.16C). I then used focused refinement as described previously to improve the resolution of the head and the arm segments (Fig. 2.16D).

2.6.1 The condensin arm segment in the presence of ATP

Overall, particles of the arm segment could be separated into two different classes: They showed either rod-shaped or flexible, open coiled-coil conformations. The first, rather homogenous class gave rise to the same folded coiled-coil confirmation that I had determined for the apo states, with the Smc4 hinge half domain binding to the Smc2 coiled-coil (**Fig. 2.17A, Fig. 2.17C**). Interestingly, some of the helical segments, especially in the elbow region, displayed slightly different conformations when compared to the arm segments of the apo states (**Fig. 2.17B**). This could be a result of movements within the head segment.

The second class of particles contained a wide range of different arm conformations and this heterogeneity impaired 3D reconstruction (**Fig. 2.17D**). In all classes that allowed the coiled coils to be traced, the hinge still appeared to fold back onto the coiled coils. In a subset of these classes, the hinge appeared to bind closer to the head segment than in the apo states, although I cannot exclude that this is a result of the particle orientation. Unlike in the apo state, however, the distance between the Smc2 and Smc4 coiled coils was larger, resulting in coils that were sometimes split along the entire length from the heads to the elbow region (**Fig. 2.17D**).

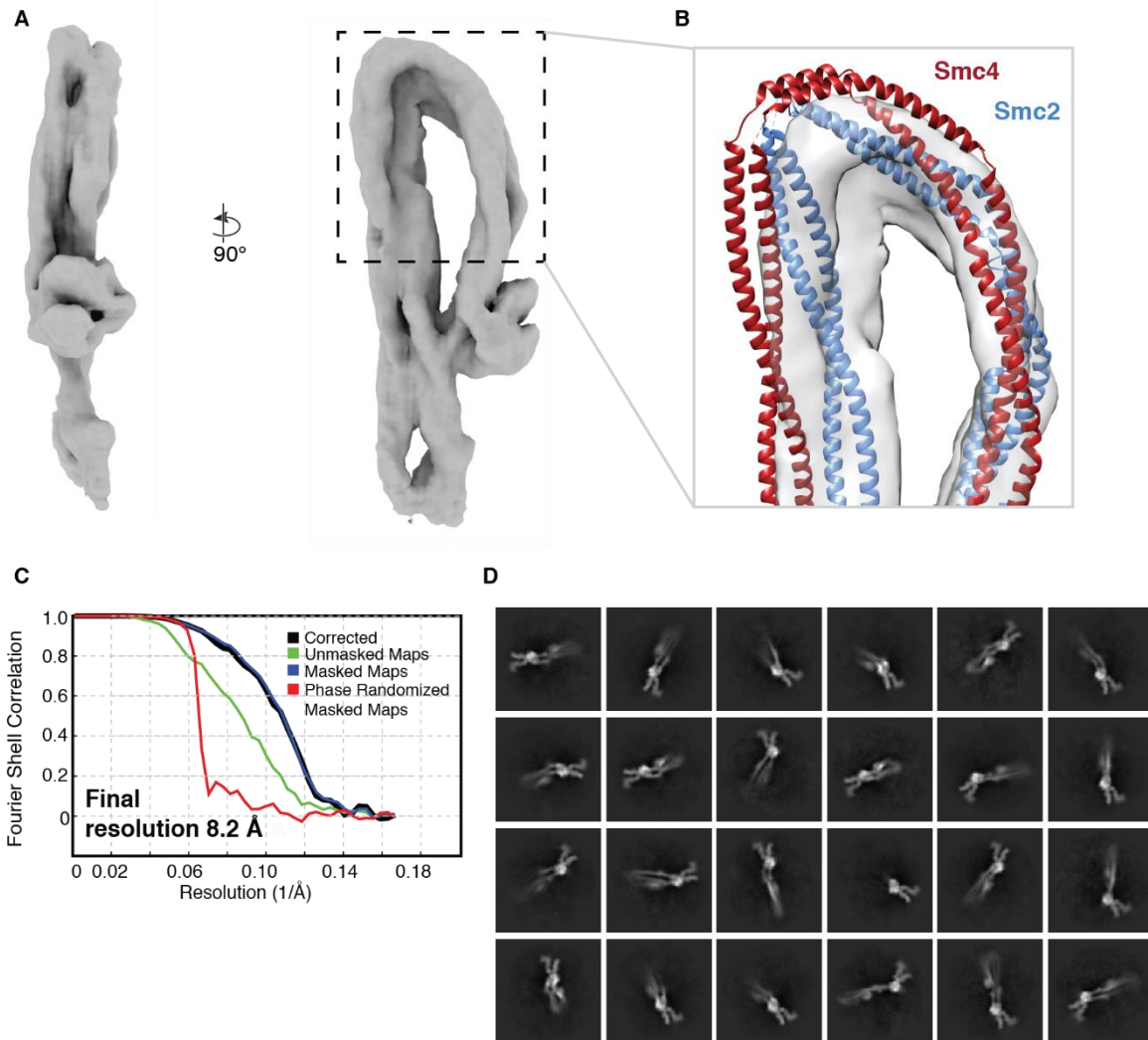


Figure 2.17: Arm segment of condensin in presence of ATP. (A) Cryo-EM density map of the rod-shaped arm segment in presence of ATP. (B) Rigid body fitting of the apo state arm segment (PDB: 6YVU) indicating differences in the elbow region. (C) Corresponding FSC curves for the cryo-EM density map in (A). (D) Representative 2D class averages of open coiled coils demonstrating the structural heterogeneity within the coiled coils upon addition of ATP. Flexibility impaired 3D reconstructions.

2.6.2 The condensin head segment in presence of ATP

Focused refinement of the head segment yielded a map of 7.6 Å resolution. I was able to clearly assign the upper part of the map to the Smc2 and Smc4 head domains with their associated coiled coils in an orientation that roughly resembled the orientation observed in the two apo states. The bottom part of the map, however, looked markedly different than the density previously assigned to Ycs4 in the apo structures (**Fig. 2.18A**). The finding that Ycs4 density cannot be assigned in the presence of ATP is consistent with biochemical evidence that indicated that Ycs4 dissociates from the

Smc4 head upon ATP binding (Hassler et al., 2019). It is conceivable that Ycs4 is only flexibly bound to the complex after its dissociation from the Smc4 head and hence is lost during particle averaging, as was the case for Ycg1 in the apo states (see **Fig. 2.3F**). Instead, I identified the additional density close to the heads to correspond to the Ycg1 subunit, as judged by rigid body fitting of the *S. cerevisiae* Ycg1-Brn1_{Ycg1} crystal structure (PDB: 5OQP) into the cryo-EM density map (**Fig. 2.18B**).

While the crystal structure of Ycg1 matched the electron density very well, I was only able to partially fit Brn1_{Ycg1} (**Fig. 2.18C**). The Brn1_{Ycg1} segment creates a 'safety belt' that is thought to encircle DNA within an unstructured region that is bordered by helical elements termed 'latch' and 'buckle' (Kschonsak et al., 2017). In the cryo-EM map, density for the latch element was absent, which indicates that, at least in absence of DNA, the Brn1 safety belt remains open, possibly in a receptive state. To improve the quality of the highly flexible coiled coils of the head segments for fitting Smc2 and Smc4 structures, I subjected the particles to an additional round of 3D classification, which resulted in a map with clear coiled-coil density for both Smc2 and Smc4 at 8.4 Å resolution (**Fig. 2.18D**).

To build a structural model, I first attempted to manually place the zipped apo state structure into the cryo-EM density. This resulted in an uncovered wedge of density between the two head domains, as well as misplaced coiled coils for either one of the two SMC proteins (**Fig. 2.18E**). Placing *Ct* Smc4_{hd}-Brn1_{Smc4} (PDB: 6QJ2) and the RecA-like and helical lobes of *Ct* Smc2_{hd} (PDB: 6QJ1) independently improved the fit of the head domains markedly (**Fig. 2.18F**). After also adapting the Smc2 coiled coil to fit the cryo-EM density, there was no unaccounted density left (**Fig. 2.18G**). This indicates that Brn1_N is absent in the presence of ATP, which is in line with previous results that demonstrated that the amino-terminal Brn1 helical domain is ejected from Smc2 upon addition of ATP (Hassler et al., 2019). In this conformation, the carboxy-terminal helix of the Smc2 coiled coils is considerably bent, providing a possible explanation for the release of the Brn1 helical domain.

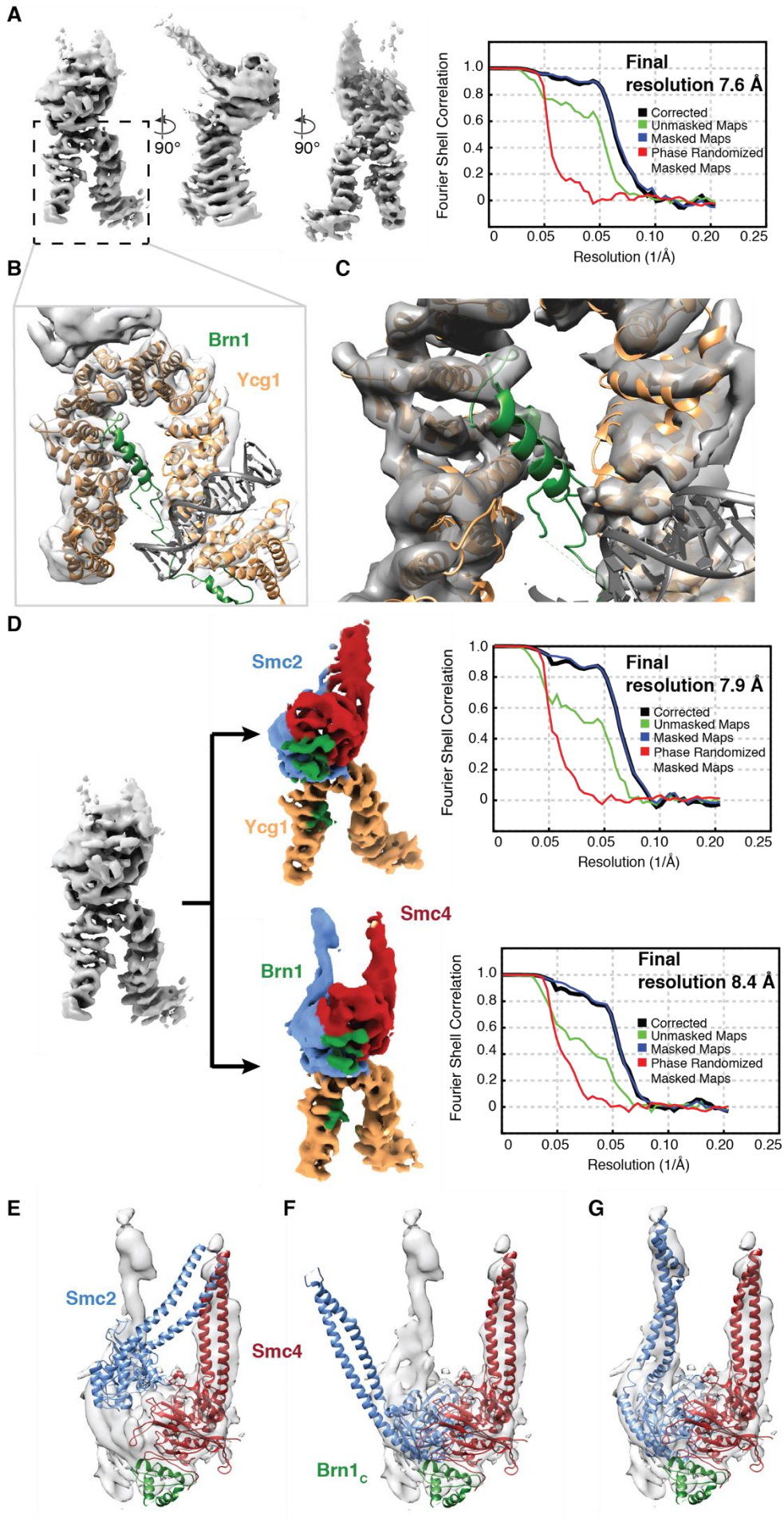


Figure 2.18: Head segment of *Sc* condensin in presence of ATP. (A) Cryo-EM density map of the head segment in presence of ATP with corresponding plot of FSC curves. (B) Rigid body fitting of *Sc* Ycg1-Brn_{Ycg1} (PDB: 5OQP) into the cryo-EM density map. (C) Absence of density for the Brn1 latch indicates that the safety belt is open. (D) 3D classification of particles from (A) yielded two classes of which one displayed clear coiled-coil density (bottom). Corresponding FSC plots are shown next to the cryo-EM density maps. (E) Rigid body fitting of the Smc2 and Smc4 head domains from the zipped apo state (PDB: 6YVU) into the cryo-EM density map of the head segment in presence of ATP demonstrating poor accordance of model and density map for Smc2. (F) Splitting *Ct* Smc2 (PDB: 6QJ1) into its RecA-like lobe and the helical part and fitting the two parts independently improved accordance of model and density map. (G) Adapting the Smc2 coiled-coil to the cryo-EM density map resulted in a bent of the carboxy-terminal helix that could be responsible for the release of Brn1_N.

Considering the intermediate resolution and the possibility of inaccuracies in placing the crystal structures, this final model of the condensin head segment looks markedly different from the zipped apo state (compare **Fig. 2.19A and B**).

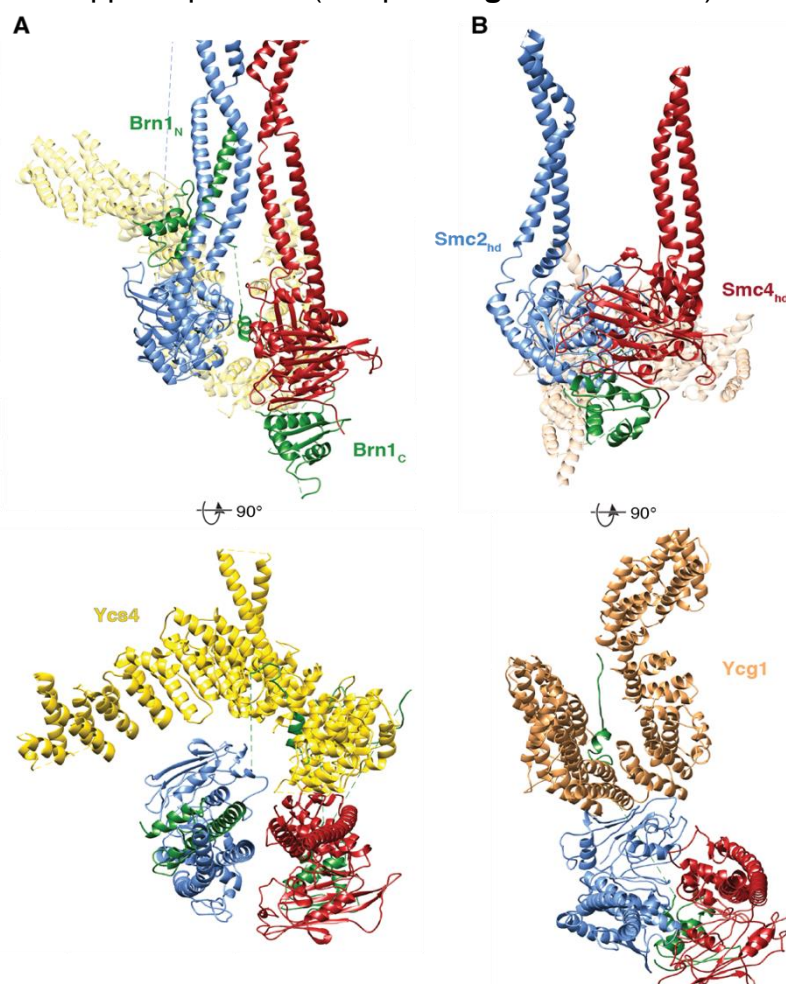


Figure 2.19: Comparison of the condensin head segment in presence and absence of ATP. (A) Pseudo-atomic model of the condensin head segment in absence of ATP (PDB: 6YVU) displaying Ycs4 binding to Smc4 and a gap between the Smc2 and Smc4 head domains. (B) Pseudo-atomic model of the head segment in presence of ATP (PDB: 6YVD) displaying Ycg1 binding to Smc2 and engaged Smc2 and Smc4 head domains.

To transition from the zipped apo state to the + ATP state, the Smc2 and Smc4 head domains need to tilt towards each other. This movement drags the coiled coils along and presumably results in an opening of the coiled coils. Furthermore, upon addition of ATP, Ycs4 is released from the Smc4 head and Ycg1 is stably bound to the Smc2 head (Fig. 2.19B).

2.7 Functional analysis of the Smc2-Ycg1 interaction

The hitherto unknown Smc2–Ycg1 interaction interface is located at the concave surface of the U-shaped Ycg1 subunit and the Smc2 head domain (Fig. 2.20A).

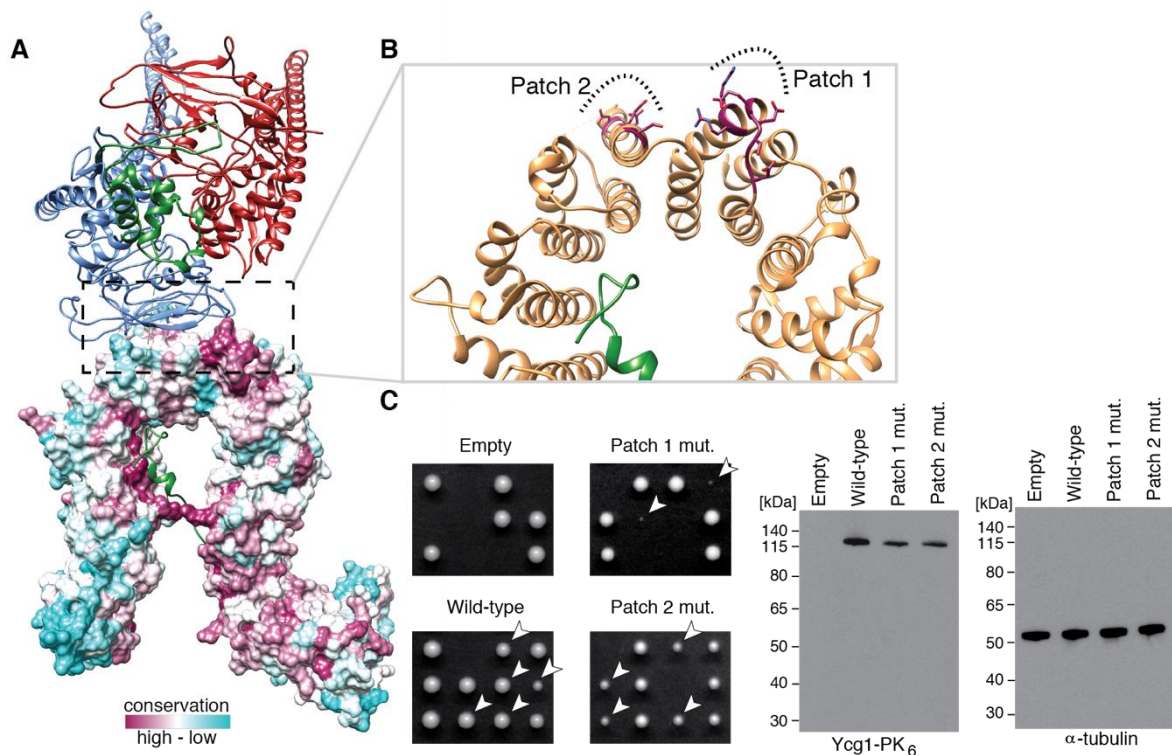


Figure 2.20: Physiological relevance of the Smc2-Ycg1 interface. (A) Pseudo-atomic model of the condensin head segment in presence of ATP with Smc2 (blue), Smc4 (red) and Brn1 (green) (PDB: 6YVD). Conservation of Ycg1 was plotted onto the surface. (B) Ycg1 side of the Smc2-Ycg1 interface with highlighted residues clustered in two conserved patches. (C) Tetrad dissection of diploid *S. cerevisiae* YCG1/*ycg1*Δ cells expressing an ectopic Ycg1-PK₆ harboring Patch 1 or Patch 2 mutations (left). Corresponding western blots (right) assaying the expression levels of Ycg1-PK₆ in wild type or patch mutants. Tubulin was used as a loading control. Panels from Lee et al., 2020. The experiments shown in this figure have been performed by Markus Hassler, Catherine Stober and Saša Perovic.

To elucidate whether Ycg1 also binds the Smc2 head *in vivo*, I first plotted conservation onto the Ycg1 surface. This revealed two conserved patches at or close to the Ycg1–Smc2_{hd} interface (**Fig. 2.20A**). Yeast strains harboring these mutations (**Table 3**) displayed reduced viability, which supports the notion that both patches are physiologically relevant for condensin’s function (**Fig. 2.20B**). In addition, a yeast strain that expressed a version of Ycg1 with the UV-crosslinkable unnatural amino acid BPA (p-benzoyl-phenylalanine) in the vicinity of the conserved patches (**Fig. 2.21A**) generated an upshifted band upon exposure to UV light that was identified as the crosslinking product of Ycg1 and Smc2 (and to a lesser extent Brn1) (**Fig. 2.21B**). Western blotting confirmed this result (**Fig. 2.21C**). In conclusion, these data support the Ycg1–Smc2 interaction observed in the cryo-EM structure of condensin in the presence of ATP and suggest that this interaction is of physiological relevance.

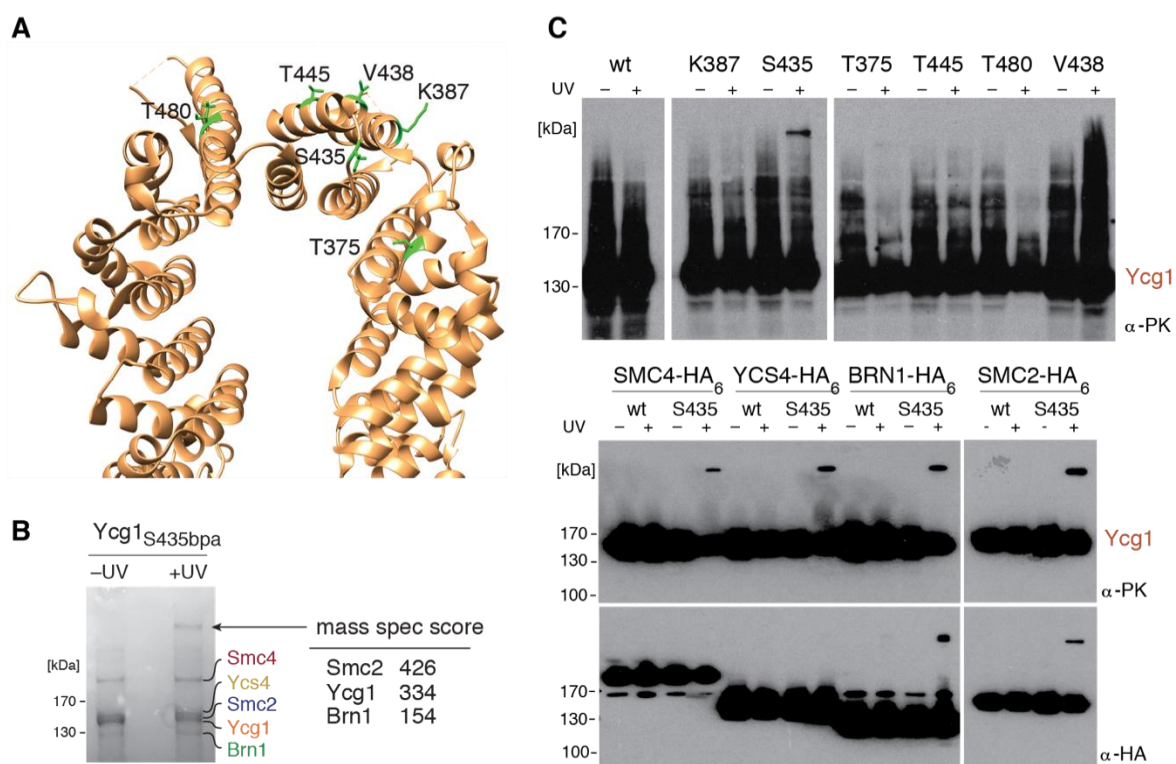


Figure 2.21: *In vivo* crosslinking of Smc2 and Ycg1. (A) Ycg1 side of the Smc2-Ycg1 interface highlighting residues that were replaced with the unnatural amino acid bpa. (B) Coomassie stained SDS-PAGE gel of purified Sc condensin holo complexes containing Ycg1_{S435bpa} before or after illumination with UV light. Mass spectrometry analysis of the upshifted band (right lane) revealed presence Smc2, Ycg1 and, to a lesser extent, Brn1. Panel from Lee et al., 2020. (C) Western blot analysis of Sc strains expressing Ycg1-PK₆ with indicated mutations before (-UV) or after (+UV) illumination with UV light (top). Endogenously HA-tagged condensin subunits Smc2, Smc4, Brn1, and Ycs4 in a yeast strain harboring wild type Ycg1 or Ycg1_{S435bpa} before (-UV) or after (+UV) photocrosslinking (bottom). Panels from Lee et al., 2020. The experiments shown in this figure have been performed by Markus Hassler, Catherine Stober and Saša Perovic.

2.8 Ycs4 and Ycg1 binding is mutually exclusive

In addition to the different conformations of the SMC head domains, the second major difference between the apo state and the +ATP state is the stable association of Ycs4 or Ycg1, respectively. The fact that I never observed particles with engaged heads that bound Ycs4 or non-engaged heads bound by Ycg1 indicates that binding of Ycg1 and Ycs4 to the Smc2 and Smc4 heads is mutually exclusive.

In a recent study, ATP binding by the Smc4 head abolished its interaction with Ycs4 (Hassler et al., 2019). Close inspection of the Ycs4 subunit structure in the apo state revealed a helix that extended from HEAT repeat 15. Alignment of the engaged heads from the +ATP structure and the zipped apo state based on the orientation of Smc4 suggests that said helix is located at a position that Smc2 would adopt in the engaged state (**Fig. 2.22A**). The resulting steric clashes would impair head engagement, which suggests that dissociation of Ycs4 from Smc4 is a prerequisite for Smc2–Smc4 head engagement.

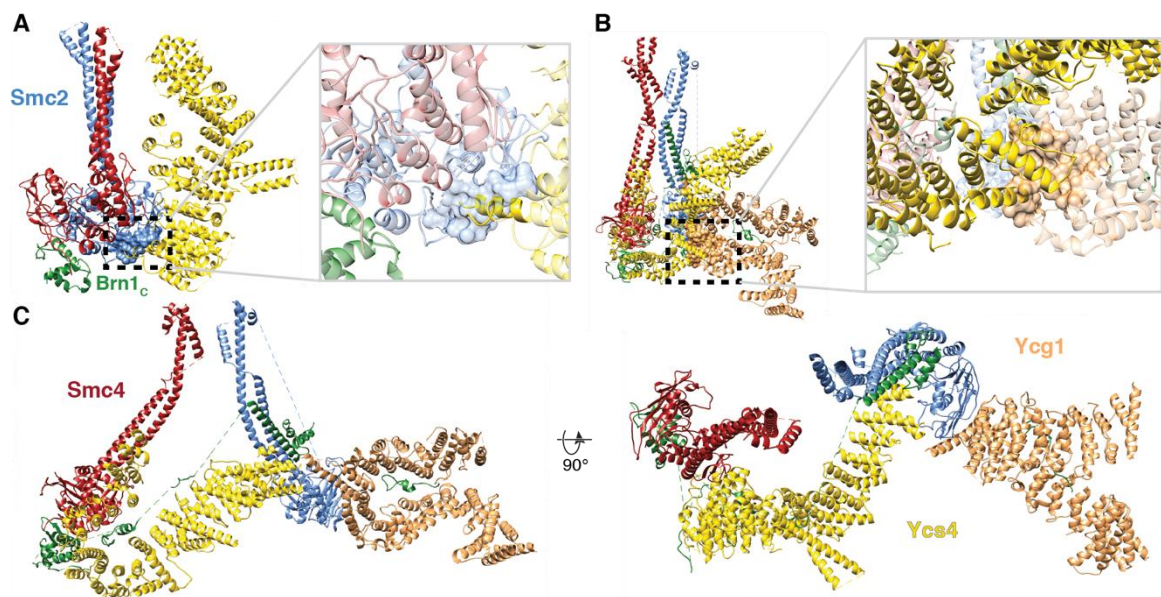


Figure 2.22: Steric clashes between the apo and the +ATP states. (A) Superimposition of the zipped apo state and the +ATP state based on Smc4 revealed that the Smc4-Ycs4 interaction and Smc2-Smc4 head engagement are incompatible due to steric clashes between the Smc2 head and HEAT repeat 15 of Ycs4. (B) Superimposition of the zipped apo state and the +ATP state based on Smc2 demonstrated that the Smc4-Ycs4 interaction and the Smc2-Ycg1 interaction are incompatible due to steric clashes between Ycs4 and Ycg1. (C) In the bridged apo state, Ycs4 and Ycg1 could theoretically bind simultaneously.

Similarly, the presence of Ycs4 bound to Smc4 also prevents Ycg1 binding to Smc2 by sterically blocking the Ycg1 interaction surface on Smc2 (**Fig. 2.22B**). This finding

indicates that it might not be the engagement of the two SMC head domains that allows Ycg1 to bind Smc2, but rather release of Ycs4. Hence, The ATP-induced release of Ycs4 from Smc4 is a pivotal step in the transition from the apo state to a nucleotide-bound state.

In contrast, in the bridged apo state, the Smc4–Ycs4 interaction would theoretically not interfere with the Smc2–Ycg1 interaction and would allow an apo state with both, Ycs4 and Ycg1, bound to the SMC head domains (**Fig. 2.22D**). The fact that I never observed such a state could indicate that additional mechanisms exist that prevent the association of Ycg1 with Smc2.

Experiments with a trimeric *C. thermophilum* condensin subcomplex that consisted of full-length Smc2 and Smc4 and a minimal Brn1 subunit addressed the mutually exclusive binding of Ycs4 and Ycg1 experimentally. The minimal Brn1 subunit (Brn1_{NC}) lacks the central part that mediates interactions with both HEAT-repeat subunits and thereby ensures that any observed interaction with a HEAT-repeat subunit reports the binding to an SMC head domain (Hassler et al., 2019; Kschonsak et al., 2017; Piazza et al., 2014). Mixing of the trimeric complex with Ycs4–Brn1_{Ycs4} resulted in the formation of a stable complex in absence of ATP, but not in the presence of ATP, as was expected from previous results (Hassler et al., 2019) (**Fig. 2.23A**). In contrast, binding of Ycg1–Brn1_{Ycg1} was independent of ATP (**Fig. 2.23B**). This result is consistent with the notion that head engagement is dispensable for the Smc2–Ycg1 interaction. As inferred from the comparison of the engaged and non-engaged states (**Fig. 2.22**), the presence of Ycs4–Brn1_{Ycs4} inhibited the interaction between Smc2–Smc4–Brn1_{NC} and Ycg1–Brn1_{Ycg1} (**Fig. 2.23C**).

In conclusion, ATP not only controls the engagement of the Smc2 and Smc4 head domains. It also regulates the mutual exclusive binding of the HEAT-repeat subunits to the SMC head domains by disengaging the Smc4–Ycs4 interface.

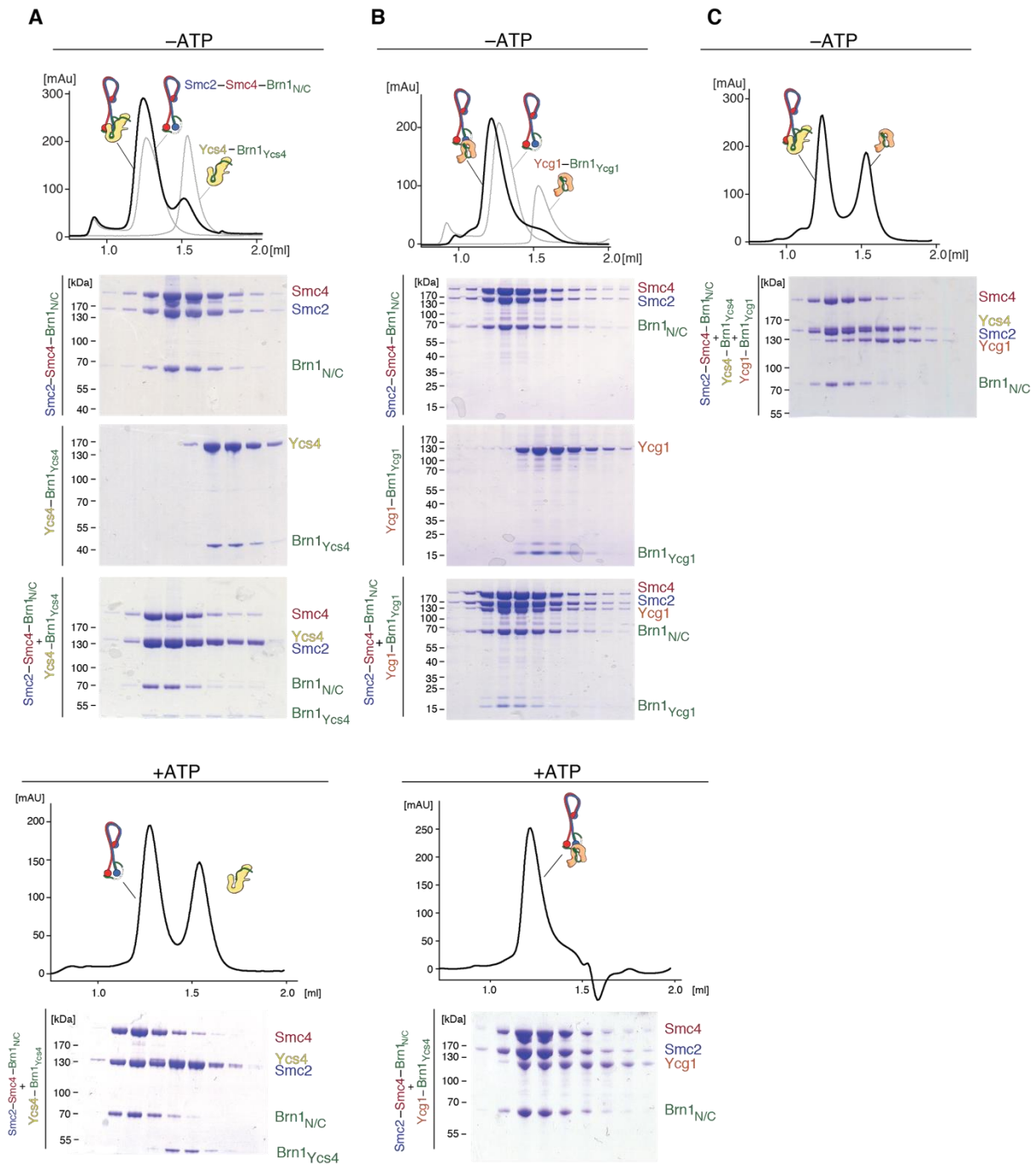


Figure 2.23: Binding of Ycg1 and Ycs4 is mutually exclusive. (A) Complex formation of *Ct* Smc2-Smc4-Brn1_{N/C} and *Ct* Ycs4-Brn1_{Ycs4} in size exclusion chromatography without (top) or with (bottom) ATP demonstrated the disruption of the Smc4-Ycs4 interface by ATP. Brn1_{N/C} lacks the constitutive Ycg1 and Ycs4 interaction sites. Coomassie stained SDS-PAGE gel shows peak fractions. (B) Complex formation of *Ct* Smc2-Smc4-Brn1_{N/C} and *Ct* Ycg1-Brn1_{Ycg1} without (top) or with (bottom) ATP revealed ATP independent binding of *Ct* Ycg1-Brn1_{Ycg1} to *Ct* Smc2-Smc4-Brn1_{N/C}. (C) *Ct* Ycs4-Brn1_{Ycs4} interaction with *Ct* Smc2-Smc4-Brn1_{N/C} prevents binding of *Ct* Ycg1-Brn1_{Ycg1} to *Ct* Smc2-Smc4-Brn1_{N/C} indicative of a mutual exclusive binding of Ycg1 and Ycs4 to the SMC head domains. All panels adapted from Lee et al., 2020. The experiments shown in this figure have been performed by Léa Lecomte.

2.9 Crosslinking mass spectrometry of condensin

During cryo-EM sample preparation, protein complexes are contained within a thin layer of liquid before being plunge frozen. It is thought that during this process, particles repeatedly touch the air-water interface, which elicits mechanical forces upon the particles (Glaeser and Han, 2017; Taylor and Glaeser, 2008). This can lead to the disintegration of protein complexes but possibly also forces the particles into non-physiological conformations. We therefore tested whether the interactions observed for the condensin holo complex by cryo-EM also occur in solution without surface effects by crosslinking mass spectrometry in collaboration with Francis O'Reilly, Ludwig Zinn and Juri Rappsilber (HU Berlin).

For the apo state, crosslinks along the entire length of the coiled coils supported a rod-like conformation of Smc2–Smc4 (**Fig. 2.24A**). Crosslinks between the Smc4 half of the hinge domain and the Smc2 coiled coil confirm the folded conformation in the absence as well as in the presence of ATP (**Fig. 2.24B**). Crosslinking mass spectrometry also identified six crosslink pairs in the head segment. Three of these crosslinks were out of range in the zipped apo state (**Fig. 2.24C**), but within distance in the bridged apo state. The opposite applied to the other three crosslinks (**Fig. 2.24C**). These results strongly suggest that both apo states observed in cryo-EM also exist in solution.

Finally, the number of crosslinks was markedly increased upon addition of ATP, possibly caused by the amount of structural rearrangements. The vast majority of the crosslinks (95% for –ATP, and 87% for +ATP) was within the expected distance of the crosslinkers used when mapped onto the pseudo-atomic models created from the cryo-EM maps.

In conclusion, crosslinking mass spectrometry data supported the existence of the three described states of the condensin holo complex.

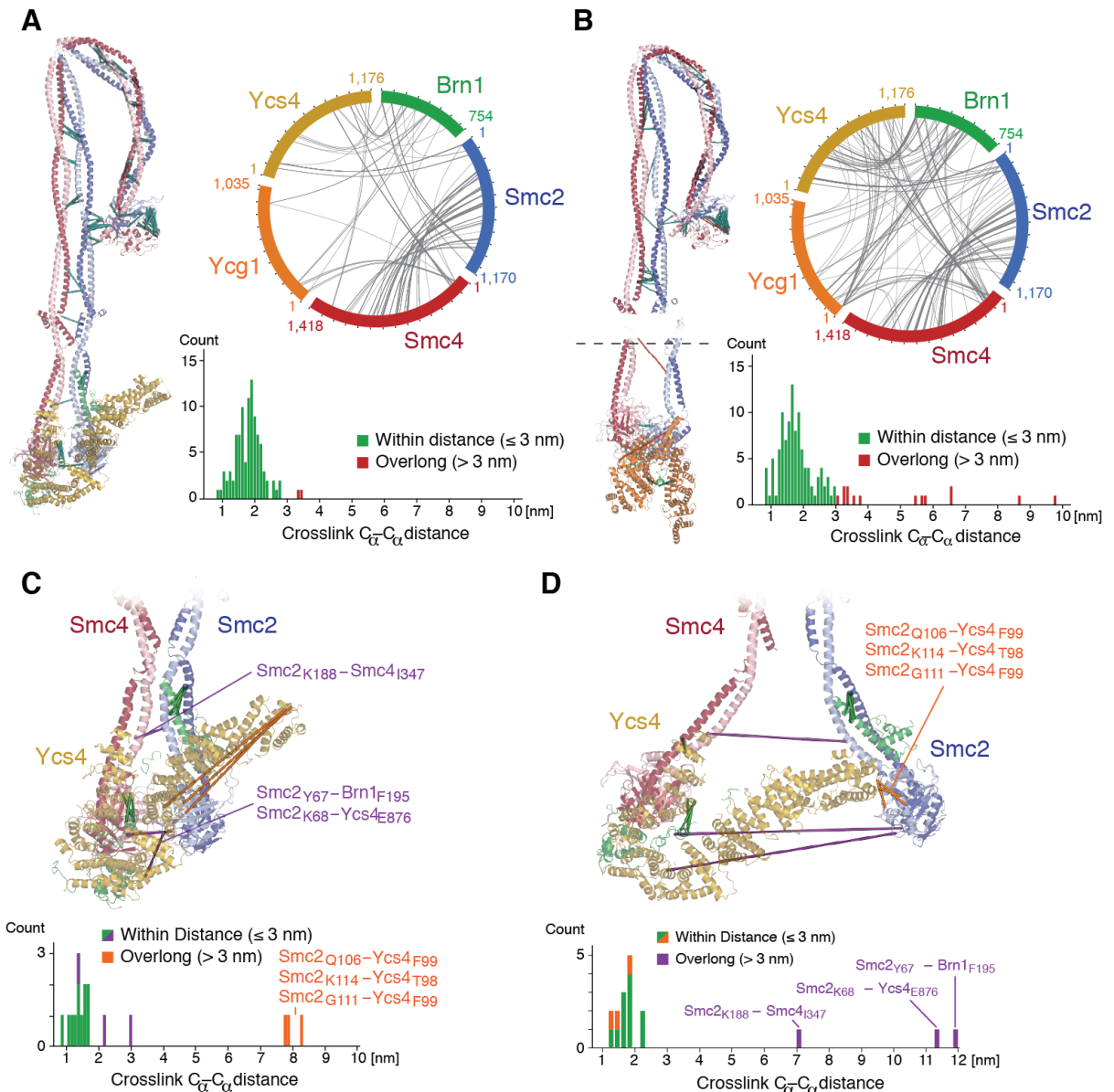


Figure 2.24: Crosslinking mass spectrometry of the condensin holo complex. (A) Intermolecular sulfo-SDA crosslinks in absence of ATP mapped onto the zipped apo state (PDB: 6YVU) (left). Circle plot of intermolecular sulfo-SDA crosslinks with an FDR <1% (top). Bar plot shows the number of crosslinks within (green) or outside (red) a distance of 30 Å (bottom). (B) As (A) but in presence of ATP. (C) Intermolecular sulfo-SDA crosslinks mapped onto the zipped head segment (PDB: 6YVU). Six crosslinks, three within distance (purple) and three overlong (orange) are highlighted. (D) Intermolecular sulfo-SDA crosslinks mapped onto the bridged head segment (PDB: 6YVV). The same six crosslinks show exactly the opposite behavior explained by the bridging of the Smc2 and Smc4 head domains. All panels adapted from Lee et al., 2020. The experiments shown in this figure have been performed by Ludwig Sinn and Francis O'Reilly.

3 Discussion

3.1 Summary of the results

Although structural information about the individual Smc2, Smc4, Brn1, Ycg1 and Ycs4 subunits of the condensin complex had been available at near-atomic resolution (Hassler et al., 2019; Kschonsak et al., 2017; Soh et al., 2015), it had remained largely unknown how the five subunits come together to form the condensin holo complex. Technological advancements in cryo-EM have now allowed me to address this 20-year-old question.

In this thesis work, I used single particle analysis cryo-EM to solve the structure of the *S. cerevisiae* condensin complex. In the absence of ATP, condensin adopts a rod-like shape. Surprisingly, the Smc2–Smc4 coiled coils are not fully extended, but instead bend sharply at the so-called elbow region, resulting in folding back of the hinge onto the coiled coils. Furthermore, condensin adopts two different apo states that differ with respect to the positions of their ATPase head segments. In the predominant class, the zipped state, Smc2 and Smc4 heads are separated by only ~2 nm, which results in the formation of closely aligned coiled coils along their entire lengths. In the minor class, the bridged state, the Smc2 head binds to the amino terminus of Ycs4. Ycs4 hence bridges the Smc2 and Smc4 head domains, which are ~10 nm apart. In both apo states, Ycs4 remains bound to Smc4, while Ycg1 is only flexibly tethered to the rest of the complex. Upon addition of ATP, the complex undergoes drastic structural changes: The Smc2 and Smc4 head domains dimerize, which presumably results in the opening of the coiled coils. Moreover, Smc4 releases Ycs4, which results in Ycg1 binding to the Smc2 head domain.

3.2 The role of the condensin arm segment

The possibility that the SMC hinge folds onto the coiled coils was already hinted at in early EM studies, which revealed kinks in the coiled coils of some particles (Anderson et al., 2002). A folded conformation was also recently described for two other SMC complexes, cohesin and MukBEF (Bürmann et al., 2019). In the condensin complex, the hinge-coiled-coil interaction is exclusively mediated by the Smc4 half of the hinge, which binds to the Smc2 coiled coil roughly halfway between the head domains and the elbow region.

The physiological relevance of this interaction has remained unclear. The hinge domain of several SMC complexes had previously been found to interact with ssDNA and, to a lesser degree, dsDNA (Chiu et al., 2004; Griese et al., 2010; Piazza et al., 2014; Vazquez Nunez et al., 2019). It is hence conceivable that folding back of the hinge serves as a mean to transport DNA closer to the head domains. This notion is supported by the finding that in cohesin and MukBEF, the kink in the coiled coils is located closer to the heads, which in turn brings the hinge into the immediate vicinity of the head segment, where presumably additional DNA binding sites exist (Bürmann et al., 2019). In MukBEF, the hinge did not always bend all the way back to the coiled coils, which might indicate that it is not the hinge-coiled-coil interaction itself that is functionally important, but the elbow region that allows bending of the coiled coils and movement of the hinge. The fact that cohesin, condensin and MukB from *E. coli* possess this sharp bend in their coiled coils argues for a conserved functional element of the complex. In contrast, *B. subtilis* SMC complexes always adopted fully extended rod-shaped conformations in negative stain EM (Soh et al., 2015).

The cryo-EM 2D class averages of condensin in the presence of nucleotide suggest that, upon addition of ATP, the gap between the coiled coils increases in size by 2-3 nm, which potentially creates a large compartment between them. In other classes, they became flexible to an extent that a 3D reconstruction was impossible.

Similar results had been observed for rotary-shadowed cohesin complexes upon addition of the non-hydrolysable ATP γ S (Hons et al., 2016). In this experimental setup, however, the coiled coils appeared extended, with the hinge positioned at the apex of the complex. This is different in condensin, where all the 2D class averages that allowed tracing the entire coiled coils retained their folded hinge conformation in presence of ATP, even if the coiled coils were separated for the entire length between head domains and elbow region. It cannot be excluded, however, that the particles of greatest flexibility have lost the hinge-coiled coil interaction.

Another hint at the structure of condensin in presence of ATP comes from recent liquid AFM studies. In this experimental setup, condensin mainly adopted O-shaped particles with completely extended and open coiled coils, as well as B-shaped particles representing a collapsed state where the hinge contacts the head segment (Ryu et al, 2019; bioarchive).

A collapsed state is also supported by two recent cryo-EM structures of cohesin (Higashi et al., 2020; Shi et al., 2020). In both cases, the hinge contacted one of the two HEAT-repeat proteins of cohesin. Shi et al. were able to show a direct contact between the Smc1–Smc3 hinge domain and STAG1, and possibly also NIPBL (Shi et al., 2020). Evolutionary evidence indicates that the HEAT-repeat subunits of cohesin and condensin share a common ancestor (Wells et al., 2017). Structural similarities support this notion and suggest that STAG1 and NIPBL are the cohesin orthologs of Ycg1 and Ycs4, respectively (further discussed below). It is important to note that in the above-mentioned studies, cohesin was in an ATP- and DNA-bound state, the so-called gripping stage. It is tempting to speculate that addition of DNA would result in a similar repositioning of the hinge from the center of the coiled-coil stem to a position closer to the head domains and HEAT-repeat subunits in the condensin complex. Future studies will have to analyze the different SMC complexes under the same conditions to evaluate the architecture of the arm segment and specifically perturb the hinge interaction interfaces in order to study their physiological relevance.

3.3 The role of the SMC head domains of condensin

The head segment of condensin in absence of ATP adopts two different states with respect to the location of the Smc2 and Smc4 head domains. In the zipped state, the head domains are closely aligned and in the correct orientation to allow head engagement, that is, each ATP binding site, which contains the Walker A and B motifs in one of the heads, faces the signature motif on the opposite head. This is in contrast to an offset of these domains that had been observed in apo structures of the *Bs* SMC-ScpAB complex and inferred from cysteine crosslinking experiments with cohesin, referred to as the ‘juxtaposed state’ (Chapard et al., 2019; Diebold-Durand et al., 2017; Vazquez Nunez et al., 2019). In this state, the signature motifs face each other and a translational movement would be required to allow ATP-dependent head engagement (**Fig. 3.1A**). This apparent difference to the here described data could be resolved, however, when considering the flexibility of the SMC head domains, as evidenced by the weak cryo-EM density for the Smc2 head. Crosslinking would trap any ‘state’ where crosslink pairs are at the right distance, even if it were only transient. The flexibility is likely necessary to allow transition from the zipped to the bridged state. It

is important to note that the interconversion between zipped and bridged states is independent of ATP.

Upon addition of ATP, the head domains close in on each other to form what I refer to as engaged heads. Due to insufficient resolution, however, the exact nucleotide state of each of the two ATP binding sites remained unclear. Since I added an equimolar ratio of ATP and AMP-PNP, any combination where one or both ATP binding sites are bound by ATP, ADP or AMP-PNP is conceivable. Interestingly, addition of ATP to a Walker B mutant condensin complex that is deficient in ATP hydrolysis displayed highly similar 2D class averages as the +ATP state reported here (data not shown).

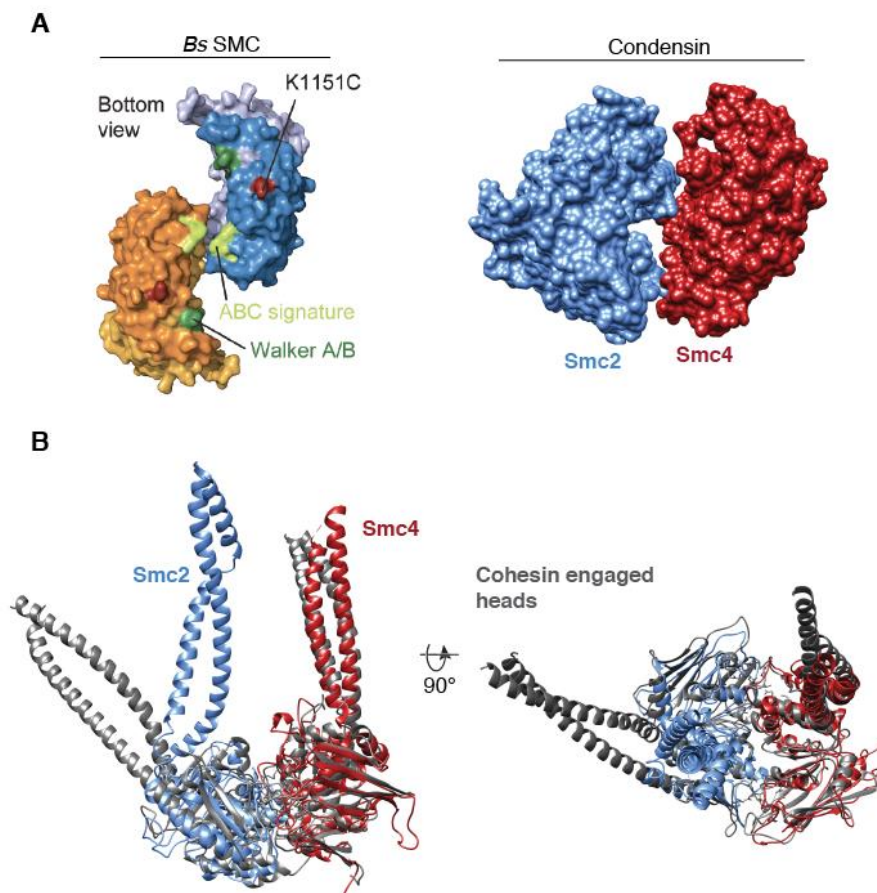


Figure 3.1: Head conformations in SMC complexes. (A) Bottom view of a model of the *Bs* SMC complex based on a combination of crystallography, crosslinking mass spectrometry and cysteine crosslinking (K1151C as one of the cysteine pairs) suggests that SMC heads are in a juxtaposed state where the signature motifs align (left) (modified from Diebold-Durand et al., 2017). The corresponding view of the condensin apo zipped state demonstrates that each ATP binding site (Walker A/B) is directly opposite of its signature motif and heads require no translational movement to allow engagement (right). (B) Superimposition of the engaged cohesin *Hs* Smc1-Smc3 dimer (PDB: 6WG3) and the presumably engaged *Sc* Smc2-Smc4 condensin dimer (PDB: 6YVU).

This indicates that the observed state is in a pre-hydrolysis state, i.e. with ATP or AMP-PNP bound to at least one active site, or that there is no significant structural change in the complex upon ATP hydrolysis to ADP and P_i.

Connected to the nucleotide state is the question whether the observed state of condensin represents a fully or only partially engaged Smc2–Smc4 dimer. This is an important distinction, considering the asymmetry between Smc2 and Smc4 ATPase sites (Hassler et al., 2019). A comparison of the nucleotide-bound state with the structures of ATP-engaged cohesin Smc1–Smc3 heads (Shi et al., 2020), reveals a highly similar conformation. This indicates that the observed condensin structure represents a fully engaged dimer with both active sites bound to a nucleotide (**Fig. 3.1B**). The structural similarity extends to wild-type engaged cohesin bound to two molecules of ADP- BeF₃⁻ and an ATP-hydrolysis deficient Walker B version of cohesin bound to two molecules of AMP-PNP (Higashi et al., 2020; Shi et al., 2020). Both ADP- BeF₃⁻ and Walker B cohesin would trap the complex in its nucleotide-bound state (Kagawa et al., 2004), further supporting the notion that condensin would be in a pre-hydrolysis state. It should be noted, however, that both cohesin structures were determined in presence of DNA, which raises the possibility that the DNA state of the complex affects the ATP state.

To address the nucleotide state of each ATPase site, future studies will have to focus on improving the resolution to a point where the nucleotide itself becomes discernible.

3.4 The condensin HEAT-repeat subunits switch position

Earlier studies revealed that Ycs4 not only binds to Brn1 (Piazza et al., 2014) but also to Smc4 in an ATP-controlled fashion (Hassler et al., 2019). The cryo-EM structures I obtained not only confirm these interactions, but also explain why the Smc4–Ycs4 interaction needs to be regulated. Without the ATP-dependent release of Ycs4, neither could Smc2 and Smc4 heads engage nor could Ycg1 bind to the Smc2 head. This marks the Smc4–Ycs4 interaction as yet another ATP-controlled interaction in the condensin complex, in addition to the Smc2–Smc4 head engagement and the Smc2–Brn1_N interaction.

It is interesting to note that in cohesin, ATP binding appears to have quite different effects. First, the structure of and position in the cohesin holo complex suggests that Scc2^{NIPBL} is the functional ortholog of Ycs4. In contrast to Ycs4, however, Scc2^{NIPBL} remained bound to the Smc1–Smc3 heads even in presence of an ATP analog (Higashi et al., 2020; Shi et al., 2020). Second, as judged from structural similarities, Scc3^{Stag1} is presumably the functional ortholog of Ycg1. Yet, there is no evidence for an interaction between Scc3^{Stag1} and Smc3, the homolog of Smc2, neither in presence nor in absence of ATP. Lastly, in contrast to the condensin Brn1_N–Smc2 interaction, the amino-terminal helical motif of the kleisin subunit Scc1^{Rad21} remains bound to the Smc3 subunit of cohesin upon addition of an ATP analog (Hassler et al., 2019; Higashi et al., 2020; Shi et al., 2020). It must be mentioned, however, that the presence of DNA in the cohesin structure could limit a direct comparison to the three described condensin states. As such, it is conceivable that DNA regulates the interactions of Scc3^{Stag1} (Ycg1) and Scc2^{NIPBL} (Ycs4) with the other subunits and leads to the re-binding of Scc1^{Rad21}_N to the Smc3 coiled-coil once DNA is bound.

The hitherto undescribed ATP-triggered positional switch of the condensin HEAT-repeat subunits requires that either Ycs4 or Ycg1 releases from the SMC heads. Because Ycg1 and Ycs4 constitutively bind to Brn1, they would not entirely dissociate from the complexes, although I cannot exclude that conditions during sample preparation led to a dissociation of Ycs4 in presence of ATP or Ycg1 in absence of ATP.

To further our understanding of the switch between Ycs4 and Ycg1, especially with regards to its physiological function, it will be crucial to specifically perturb each interaction. While this has been achieved for Ycs4 (Hassler et al., 2019), the Ycg1-Smc2 interaction can possibly be disrupted by mutating the negatively charged, conserved patch of Ycg1.

3.5 Possible modes of DNA binding by the condensin complex

It is obvious that condensin needs to interact with DNA to achieve its chromatin organizing functions. While several subunits or domains have been implied in direct DNA binding (Griese et al., 2010; Kschonsak et al., 2017; Piazza et al., 2014; Strick

et al., 2004; Vazquez Nunez et al., 2019), only Ycg1 has so far been unambiguously shown to interact with dsDNA (Kschonsak et al., 2017). Nonetheless, the position of DNA within the condensin holo complex has remained unknown, especially when one considers that asymmetric loop-extrusion likely requires more than a single DNA binding site.

For the structurally related Rad50–Mre11 complex, Rad50 has been shown to bind DNA at its coiled-coil neck region above the head domain (Käshammer et al., 2019; Liu et al., 2016; Rojowska et al., 2014). An additional DNA binding site was observed on top of the engaged Rad50 head domains (**Fig. 3.2A**) (Käshammer et al., 2019). Likewise, cryo-EM structures of cohesin revealed a DNA binding site on top of the engaged Smc1–Smc3 head domains (**Fig. 3.2B**) (Higashi et al., 2020; Shi et al., 2020). It is tempting to speculate whether a similar DNA binding site exists on top of the Smc2–Smc4 heads in condensin. There is indeed sufficient space in the nucleotide-bound state to accommodate a dsDNA between the head-proximal coiled coils (**Fig. 3.2C**). In addition, in the case of cohesin, Scc2^{NIPBL} forms an elongated DNA-binding channel together with Scc3^{Stag1} that extends the binding sites on the Smc1–Smc3 head domains (**Fig. 3.2D**). The high similarity between Scc2^{NIPBL} in the ATP state and Ycs4 in the apo state raises the possibility that Ycs4 could also contribute to DNA binding. In this respect, the bridged apo state could be important to allow access of DNA to the concave surface of Ycs4. This notion is supported by positively charged residues along said surface (**Fig. 3.2E**) and the fact that Ycs4 shifts DNA in EMSA assays (Kschonsak et al., 2017). Once DNA is bound by Ycs4, a switch to the zipped apo state could lead to wrapping of Smc2 and Smc4 around the DNA (**Fig. 3.2F**).

Unlike in cohesin, the binding of Ycg1 to the Smc2 head in the nucleotide-bound state would not create an elongated channel if DNA were bound within the Ycg1–Brn1_{Ycg1} safety belt and on top of the SMC head domains at the same time. To elucidate how the condensin holo complex interacts with DNA, single particle analysis or sub tomogram averaging could be used to obtain a condensin cryo-EM structure in the presence of DNA.

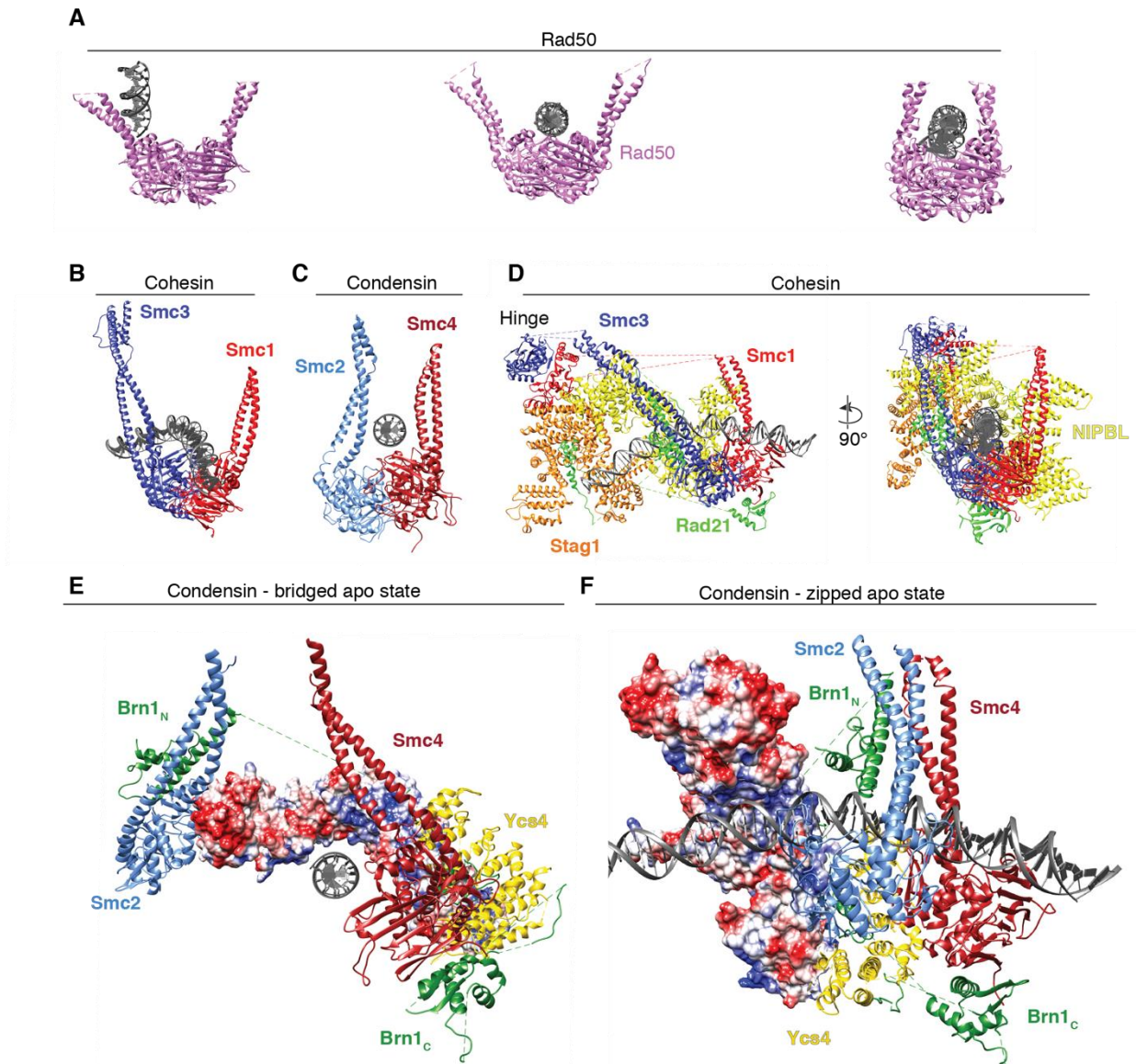


Figure 3.2: DNA in SMC and SMC-like complexes. (A) Crystal and cryo-EM structures of Rad50 in complex with DNA (PDBs from left to right: 4W9M, 5F3W, 6S85) showing a DNA binding site on top of the engaged ATPase head domains. (B) Cryo-EM structure of *Hs* cohesin in presence of DNA (PDB: 6WG3). (C) Model of how an engaged Smc2-Smc4 dimer could interact with DNA similar to cohesin and Rad50 (PDB: 6YVD). (D) Structure of *Hs* cohesin walker B mutant in presence of ATP and DNA (PDB: 6WG3) displaying a DNA binding channel formed by the engaged Smc1-Smc3 dimer, Scc2^{NIPBL} and Scc3^{Stag1}. (E) Model of the *Sc* condensin bridged apo state (PDB: 6YVV) suggesting that the bridged apo state could be important to allow DNA access to a positively charged groove in Ycs4. Electrostatic potential map of the Ycs4 amino-terminal part is shown; red: -10 keT, blue: +10 keT. (F) Model of how *Sc* condensin in its zipped apo state (PDB: 6YVU) could interact with DNA by forming a channel between the Smc2 and Smc4 head domains and Ycs4. Addition of ATP could then result in a similar DNA binding mode as observed in cohesin. Electrostatic potential map of the Ycs4 amino-terminal part is shown; red: -10 keT, blue: +10 keT.

3.6 A model for the condensin ATPase cycle

Although ATP binds solely to the ATPase sites in the Smc2 and Smc4 head domains, the effects of ATP binding lead to structural rearrangements throughout the entire ~40 nm complex. In its apo state, condensin is mostly found in a zipped state with closely aligned Smc2 and Smc4 coiled coils and with Ycs4 bound to the Smc4 head domain. Spontaneous transition into the bridged state possibly allows DNA to interact with Ycs4 in a similar manner as DNA binds Scc2^{NIPBL} in cohesin.

Addition of ATP results in the binding of ATP to the Smc4 active site, which leads to the release of Ycs4 from the Smc4 head. The release of Ycs4 in turn enables binding of Ycg1 to Smc2. All these flexible movements most likely explain the fuzzy cryo-EM density close to the ATPase heads. At the same time as Ycg1 binds the Smc2 head, a second ATP molecule binds to the Smc2 ATPase site, which results in the complete engagement of the Smc2–Smc4 head domains. Head engagement leads to opening of the coiled coils from their zipped conformation. Possibly due to constraints that arise in the arm segment, the Smc2 coiled coil is bent considerably at a position close to the neck region. The bent in the carboxy-terminal helix could explain the dissociation of the amino-terminal Brn1 fragment. If there were DNA positioned on top of the engaged SMC heads, like it is in cohesin, release of Brn1_N would allow the DNA to enter the compartment between the SMC coiled coils. To elucidate the exact order of events in the ATPase cycle, combinations of single ATPase site mutants could be used to determine the structure of intermediate states. This will be a crucial step in solving the mystery of how condensin mechanistically extrudes DNA loops to organize mitotic chromosomes.

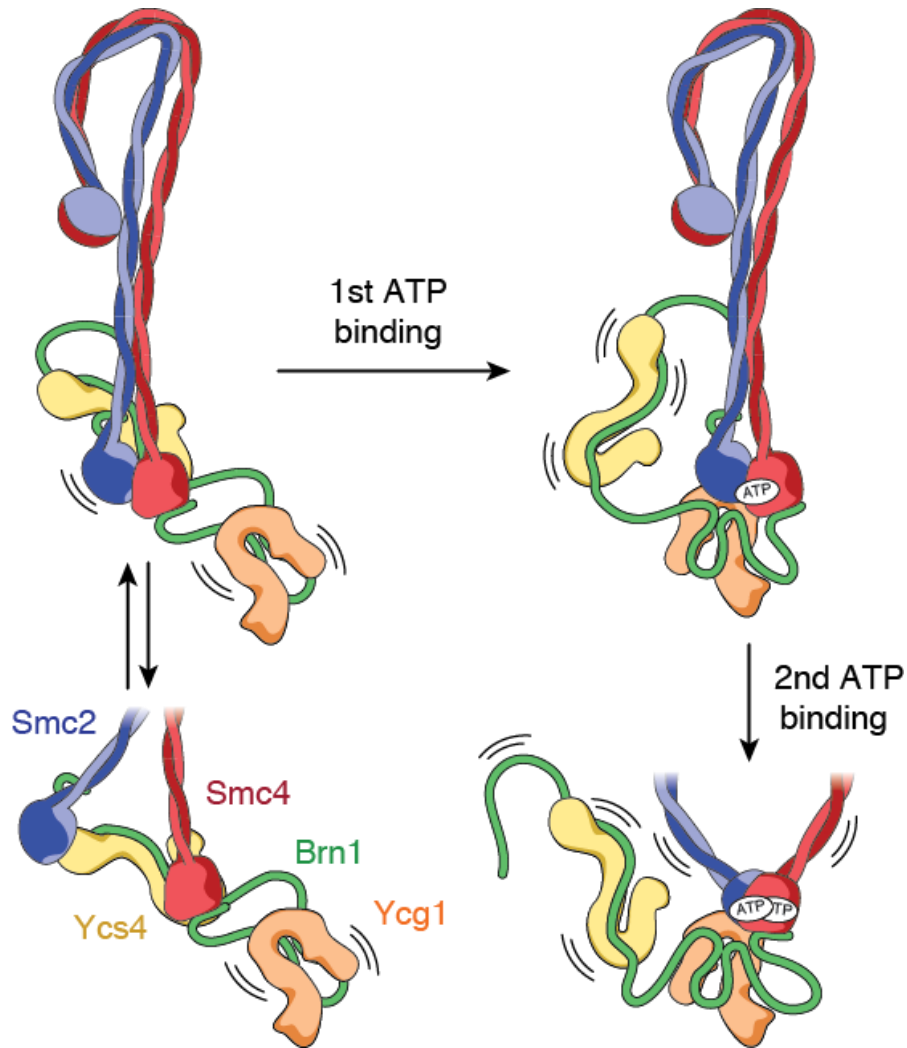


Figure 3.3: Model for the condensin reaction cycle. Without ATP, the condensin complex adopts either a zipped or a bridged state where the Smc2 and Smc4 head domains are separated by ~2 nm or ~10 nm, respectively. In the zipped state, Ycs4 interacts with Smc4 while in the bridged state Ycs4 interacts with both Smc2 and Smc4. Binding of ATP to the Smc4 ATPase site releases Ycs4 which in turn allows Ycg1 to bind Smc2. Once a second molecule of ATP binds the Smc2 ATPase site, the Smc2 and Smc4 head domains engage. The structural rearrangement necessary for this dimerization results in opening of the formerly rod-shaped coiled coils. During this process, the Smc2 coiled-coil is kinked potentially leading to the release of the amino-terminal fragment of Brn1 (From Lee et al. 2020).

4 **Material and Methods**

4.1 Materials

4.1.1 Software

Table 1: Software

Software	Source
CryoEM	
SerialEM	Mastronade, 2005
Relion 3	Zivanov et al., 2018
CryoSparc 2	Punjani et al., 2017
MotionCorr2	Zheng et al., 2017
GCTF	Zhang et al., 2016
Warp	Tegunov and Cramer, 2019
cryoEF	Naydenova and Russo, 2017
Data visualization	
UCSF chimera	Pettersen et al., 2004
UCSF ChimeraX	Goddard et al., 2018
ConSurf	Ashkenazy et al., 2016
Jalview 2.11.1.0	Waterhouse et al., 2009
Coot 0.8.2	Emsley and Cowtan, 2004
Fiji 2	Schindelin et al., 2012
Online sources	
PDB	https://www.rcsb.org/
EMDB	https://www.ebi.ac.uk/pdbe/emdb/
Thesis writing	
Office 2016	Microsoft

Software	Source
Illustrator CS6	Adobe
Zotero 5.0.89	Zotero.org

4.1.2 Strains

Table 2: *E. coli* strains

Name	Genotype	Source
<i>E. coli</i> Rosetta 2 (DE3) pLysS	F- <i>ompT hsdSB</i> ($tb^- mb^-$) <i>gal dcm</i> λ (DE3 [<i>lacI lacUV5-T7 gene 1 ind1 sam7 nin5</i>]) pLysSpRARE2 (Cam ^R)	Merck

Table 3: *S. cerevisiae* strains

ID	Genotype	Source
Figure 2.20		
C4943	<i>ycg1::natNT2</i> , [YCplac111 <i>Ycg1-PK6(int)::LEU2</i>], [pLH157::TRP1]	Lena Thaerichen
C4276	<i>ycg1::natNT2/YCG1</i> , <i>ura3::empty vector::URA3/ura3</i>	Marc Kschonsak
C4408	<i>ycg1::natNT2/YCG1</i> , <i>ura3::YCG1-PK6(int)::URA3/ura</i>	Marc Kschonsak
C4909	<i>ycg1::natNT2/YCG1</i> , <i>ura3::ycg1(D433K, D436K, E437K, R440D, R441D)-PK6(int)::URA3/ura3</i>	Lena Thaerichen
C5450	<i>ycg1::natNT2/YCG1</i> , <i>ura3::ycg1(D477R, E484R, D488R, D491R)-PK6(int)::URA3/ura3</i>	Catherine Stober
Fig. 2.21		
C4943	<i>ycg1::natNT2</i> , [YCplac111 <i>Ycg1-PK6(int)::LEU2</i>], [pLH157::TRP1]	Lena Thaerichen

ID	Genotype	Source
C4944	ycg1::natMX, [YCplac111 Ycg1(S435amb)-PK6(int)::LEU2],[pLH157::TRP1]	Lena Thaerichen
C4947	ycg1::natMX, [YCplac111 Ycg1(K387amb)-PK6(int)::LEU2],[pLH157::TRP1]	Lena Thaerichen
C4948	ycg1::natMX, [YCplac111 Ycg1(T375amb)-PK6(int)::LEU2],[pLH157::TRP1]	Lena Thaerichen
C4949	ycg1::natMX, [YCplac111 Ycg1(T445amb)-PK6(int)::LEU2],[pLH157::TRP1]	Lena Thaerichen
C4950	ycg1::natMX, [YCplac111 Ycg1(T480amb)-PK6(int)::LEU2],[pLH157::TRP1]	Lena Thaerichen
C4951	ycg1::natMX, [YCplac111 Ycg1(V438amb)-PK6(int)::LEU2],[pLH157::TRP1]	Lena Thaerichen
C5426	ycg1::natNT2, SMC4-HA6::HIS3, [YCplac111 YCG1-PK6(int); LEU2],[pLH157; TRP1]	Catherine Stober
C5427	ycg1::natNT2, SMC4-HA6::HIS3, [YCplac111 YCG1(S435amb)-PK6(int); LEU2], [pLH157; TRP1]	Catherine Stober
C5195	ycg1::natNT2, YCS4-HA6::HIS3, [YCplac111 YCG1-intPK6(int)::LEU2], [pLH157::TRP1]	Marc Kschonsak
C5196	ycg1::natNT2, YCS4-HA6::HIS3, [YCplac111 YCG1(S435amb)-PK6(int)::LEU2], [pLH157::TRP1]	Marc Kschonsak
C5197	ycg1::natNT2, BRN1-HA6::HIS3, [YCplac111 YCG1-PK6(int)::LEU2], [pLH157::TRP1]	Marc Kschonsak
C5198	ycg1::natNT2, BRN1-HA6::HIS3, [YCplac111 YCG1(S435amb)-PK6(int); LEU2], [pLH157::TRP1]	Marc Kschonsak
C5193	ycg1::natNT2, SMC2-HA6::HIS3, [YCplac111 YCG1-PK6(int) LEU2], [pLH157 TRP1]	Marc Kschonsak
C5194	ycg1::natNT2, SMC2-HA6::HIS3, [YCplac111 YCG1(S435amb)-PK6(int) LEU2], [pLH157 TRP1]	Marc Kschonsak

Fig. 2.1

ID	Genotype	Source
C4491	MATa, lys2::pGAL1 GAL4::LYS2, pep4::HIS3, bar1::hisG, [2micron pGAL7 SMC4- StreplI3, pGAL10 SMC2, pGAL1 BRN1-His12-HA3, TRP1], [2micron pGAL1 YCG1, pGAL10 YCS4, URA3]	Terakawa et al., 2017

All *S. cerevisiae* strains were created in a *W303* background.

4.1.3 Plasmids

Table 4: *E. coli* and *Sf21* expression plasmids

ID	Name	Source
1778	pET-MCN-Brn1 ₅₁₅₋₆₃₄ -Ycg1 (Amino-terminal 6xHIS-tag-TEV-cleavage-site, residues 515-634 of <i>C. thermophilum</i> Brn1 and residues 24-1006 of untagged <i>C. thermophilum</i> Ycg1)	Dominique Koppenhoefer
2221	pET-MCN-Brn1 ₂₂₅₋₅₁₂ -Ycs4 (Amino-terminal 6xHIS-tag-TEV-cleavage-site, residues 225-512 of <i>C. thermophilum</i> Brn1 and residues 3-1222 of untagged <i>C. thermophilum</i> Ycs4)	Marc Kschonsak
3565	pAceBac1-SMC2-SMC4-StreplI-Brn1-His8 (lacking residues 225-634,3C cleavage-site between residues 224-635), full length of <i>C. thermophilum</i> Smc2 and Smc4, residues 1-224 and 635-898 of <i>C. thermophilum</i> Brn1	Robin Stipp

4.1.4 Buffers and media

For all buffers, media and solutions, double distilled water (ddH₂O) was used.

Coomassie staining solution: 0.2% (w/v) Coomassie brilliant blue R250, 45% (v/v) ethanol, 10% (v/v) acetic acid

Coomassie destaining solution: 30% (v/v) methanol, 7% (v/v) acetic acid

5x SDS loading buffer: 250 mM Tris-HCl pH 6.8, 10% (w/v) SDS, 50% (v/v) glycerol, 0.5% (w/v) bromophenol blue, 0.5 M DTT

YPAD/YEPD: 2% (w/v) peptone, 2% (w/v) glucose, 1% (w/v) yeast extract

-URA -TRP media: 0.8% (w/v) DIFCO yeast nitrogen base without amino acids, 0.0055% (w/v) tyrosine, 0.0055% (w/v) adenine, 1.1% (w/v) C.A.A. vitamin assay, 0.01% (w/v) leucine (added after autoclaving), 2% (w/v) raffinose or glucose (after autoclaving)

-LEU -TRP media: 0.8% (w/v) DIFCO yeast nitrogen base without amino acids, 0.0055% (w/v) tyrosine, 0.0055% (w/v) adenine, 1.1% (w/v) C.A.A. vitamin assay, 2% (w/v) raffinose or glucose (after autoclaving)

MOPS: 50 mM Tris, 50 mM MOPS, 0.1% (w/v) SDS, 0.8 mM EDTA

Western blot blocking solution: 25 mM Tris-HCl pH 7.4, 140 mM NaCl, 3 mM KCl, 0.05% (v/v) Tween 20, 5% (w/v) milk powder

TBS: 25 mM Tris-HCl pH 7.4, 140 mM NaCl, 3 mM KCl

TBS-T: 25 mM Tris-HCl pH 7.4, 140 mM NaCl, 3 mM KCl, 0.05% (v/v) Tween 20

SpoVB: 0.19% (w/v) KCl, 0.82% (w/v) sodium acetate, 0.035% (w/v) MgSO₄, 0.12% (w/v) NaCl

4.1.5 Antibodies

Table 5: Primary and secondary antibodies

Target	Source
PK6-tag (mouse monoclonal)	Serotec
HA-tag (rabbit monoclonal)	Abcam
Tubulin (TAT1) (mouse monoclonal)	Woods et al., 1985
Anti-mouse IgG-HRP (goat polyclonal)	Dianova
Anti-rabbit IgG-HRP (goat polyclonal)	Dianova

4.1.6 Data availability

Model and map of the *S. cerevisiae* condensin head segment in presence of ATP were submitted to PDB (6YVD). The map of the *S. cerevisiae* condensin arm segment in presence of ATP was submitted to EMDB (10964).

4.2 Methods

4.2.1 Protein expression and purification

S. cerevisiae condensin holo complex

Expression of *S. cerevisiae* condensin holo complexes containing the five subunits Smc2, Smc4-StrepII₃, Brn1-His₁₂-HA₃, Ycg1 and Ycs4 were co-expressed in *S. cerevisiae* (C4491) from 2 μ plasmids (*URA3 leu2-d pGAL7-SMC4-StrepII₃ pGAL10-SMC2 pGAL1-BRN1-HA₃-His₁₂ TRP1 leu2-d pGAL10-YCS4 pGAL1-YCG1*). Cultures were inoculated to OD₆₀₀ 0.2 and grown at 30 °C in synthetic complete (SC) –TRP –URA media containing 2 % (w/v) raffinose to OD₆₀₀ of 1. Overexpression was achieved by addition of 2 % (w/v) galactose for 18 hr at 30 °C. Cells were then harvested by centrifugation and resuspended in His buffer (50 mM Tris-HCl pH 7.5, 200 mM NaCl, 20 mM imidazole, 5 mM β -mercaptoethanol, 5 % (v/v) glycerol) supplemented with 1x cOmplete™ EDTA-free Protease Inhibitor Cocktail (cOm–EDTA, Roche). Resuspended cells were then frozen in liquid nitrogen followed by cryo-milling (SPEX Sample Prep Freezer/Mill 6970). The lysate was cleared by two rounds of centrifugation at 45,000 \times g 20 min each at 4 °C and loaded onto a 5-ml HisTrap column (GE Healthcare) pre-equilibrated with His buffer. To remove unspecific interactions, the resin was exposed to a series of washing steps: First, with 3 column volumes (CV) His buffer. Second, with 4 CV His Buffer supplemented with 500 mM NaCl. Third, with His Buffer containing 1 mM MgCl₂, 10 mM KCl, 1 mM ATP. Fourth, with 4 CV His Buffer containing 40 mM imidazole. Elution of bound protein was achieved in His Buffer supplemented with 200 mM imidazole. After pooling and diluting the peak fractions to 1.5 mM EDTA, Tween 20 (0.01 % (v/v) final) and PMSF (0.1 mM final) was added before incubating with 2 ml (bed volume) Strep-Tactin high-capacity Superflow resin (IBA) for 16 h at 4 °C. SB-wash buffer containing 20 mM HEPES-NaOH pH 7.5, 500 mM NaCl, 2% (v/v) glycerol, 1 mM MgCl₂, 1 mM DTT, 0.01% (v/v)

Tween 20 and SB-ATP-wash buffer containing 20 mM HEPES-NaOH pH 7.5, 200 mM NaCl, 50 mM KCl, 2 % (v/v) glycerol, 10 mM MgCl₂, 1 mM DTT, 0.01 % (v/v) Tween 20, 1 mM ATP was used to wash the beads. Elution was carried out in SB-elution buffer containing 20 mM HEPES-NaOH, 200 mM NaCl, 2 % (v/v) glycerol, 1 mM MgCl₂, 1 mM DTT and 5 mM d-desthiobiotin. Eluted fractions were concentrated by ultrafiltration (Vivaspin 30,000 MWCO) and loaded on a Superose 6 10/30 column (GE Healthcare) pre-equilibrated with Sup6 buffer containing 20 mM HEPES-NaOH pH 7.5, 200 mM NaCl, 2 % (v/v) glycerol, 1 mM MgCl₂, 1 mM DTT. Peak fractions were pooled and concentrated to 5-10 μM by ultracentrifugation.

C. thermophilum condensin subcomplexes

C. thermophilum condensin non-SMC subcomplexes Ycg1–Brn1_{Ycg1} and Ycs4–Brn1_{Ycs4} were expressed from pET-MCN plasmids in an *E. coli* Rosetta (DE3) pLysSRARE2 strain. Bacteria were grown in 2xTY medium at 37 °C. Induction was carried out by addition of IPTG to a final concentration of 0.2 mM at 18 °C for 18 h. Sonication at 4 °C in lysis buffer (50 mM Tris-HCl pH 7.5, 500 mM NaCl, 20 mM imidazole-HCl pH 7.5, 5 mM β-mercaptoethanol, cOm-EDTA) was used to lyse cells. The lysate was then centrifuged at 45,000 xg prior to mixing the supernatant with Ni-Sepharose beads (GE Healthcare; 1 mL of beads/mL lysate). Beads were washed once with 50–100 CV lysis buffer. For elution of bound proteins, 5–7 CV of lysis buffer supplemented with 300 mM imidazole were added. After dialysis at 4 °C in 25 mM Tris-HCl pH 7.5, 300 mM NaCl, 1 mM DTT in a SnakeSkin™ dialysis tubing with a size cut-off of 10,000 MW (Thermo Fisher), the sample was diluted to a final NaCl concentration of 150 mM. For anion exchange, a 6-mL Resource Q anion exchange column (GE Healthcare) was pre-equilibrated with 25 mM Tris-HCl pH 7.5, 100 mM NaCl, 1 mM DTT. The column was washed with 3-5 CV of the pre-equilibration buffer. Elution was performed by increasing NaCl concentration in a linear gradient of 10 CV to 1 M. A Superdex 200 26/60 column (GE Healthcare) was pre-equilibrated in 25 mM Tris-HCl pH 7.5, 300 mM NaCl, 1 mM DTT and loaded with peak fractions from the anion exchange chromatography. Peak fractions were again collected and concentrated using a Vivaspin tube with a molecular weight cut-off of 30,000 (Sartorius).

C. thermophilum condensin subcomplexes containing Smc2-Smc4-Brn1_{NC} were expressed from a Multibac plasmid in Sf21 cells (Fitzgerald et al., 2006). The first steps of purification including clearing lysates and NiNTA affinity chromatography was performed as described above for the non-SMC subcomplexes. To desalt the sample, a HiPrep 26/10 desalting column (GE Healthcare) was used with 50 mM Tris-HCl pH 7.5, 100 mM NaCl, 1 mM DTT. Anion exchange chromatography was carried out as described for the non-SMC subcomplexes. Peak fractions from anion exchange chromatography were pooled and loaded onto a Superose 6 10/300 column (GE Healthcare) pre-equilibrated with 25 mM Tris-HCl pH 7.5, 200 mM NaCl, 1 mM DTT, 5 % glycerol. Smc2-Smc4-Brn1_{NC} fractions were pooled and concentrated using a Vivaspin tube with a molecular weight cut-off of 30,000 (Sartorius).

4.2.2 Analytical size-exclusion chromatography

To analyse a potential interaction between condensin subcomplexes Ycg1–Brn1_{Ycg1}, Ycs4–Brn1_{Ycs4} and Smc2–Smc4–Brn1_{NC} of *Chaetomium thermophilum*, complexes were incubated on ice for 15 min at a concentration of 15 μ M (equimolar ratio) in a buffer containing 50 mM Tris-HCl, pH 7.5, 1 mM DTT, 1 mM MgCl₂ and a final concentration of 150 mM NaCl. Size-exclusion was carried out in a pre-equilibrated Superose 6 Increase 3.2/300 column (GE Healthcare) at a flow rate of 0.05 ml min⁻¹. SEC buffer containing 50 mM Tris-HCl, pH 7.5, 150 mM NaCl, 1 mM DTT, 1 mM MgCl₂ was used for pre-equilibration. Fractions were collected in 100 μ l batches. Peak fractions were loaded onto a NuPage™ 4–12% Bis-Tris SDS gel (Thermo Fisher). Proteins in the gel were visualized by Coomassie Blue staining. For ATP experiments, Smc2–Smc4–Brn1_{NC} complexes were incubated with 1 mM ATP on ice prior to gel filtration, and the SEC buffer was supplemented with 0.1 mM ATP.

4.2.3 *In vivo* crosslinking

To create yeast strains expressing Ycg1_{bpa} constructs, plasmid shuffle was used in a *ycg1* Δ background strain. The *URA3*-based episomal plasmid to be replaced contained a wild-type *Ycg1* allele in a *TRP1*-based plasmid encoding *E. coli* TyrRS and tRNA CUA. The replacing *LEU2*-based centromeric plasmid contained a *ycg1*_{bpa}

allele with an amber stop codon at the indicated position. Strain genotypes are listed in Table 2. Protein levels were assayed by Western blotting. To this end, yeast strains were grown at 30 °C to an OD₆₀₀ of 0.6–0.8 in 20 ml –LEU–TRP synthetic drop-out medium supplemented with 1 mM p-benzoyl-L-phenylalanine (bpa; Bachem 4017646). Centrifugation was used to harvest cells. After resuspending the pellet in 4 ml PBS, half of the sample was irradiated with 365 nm light to a total of 10 J (~50 min exposure time) on ice. The other half of the cells was kept in the dark. Centrifugation was used to harvest the cells. Harvested cells were resuspended in 0.2 ml 100 mM NaOH and kept at room temperature for 10 min. Cells were harvested again by centrifugation. Lysis was performed in SDS loading buffer (50 mM Tris-HCl, pH 6.8, 2% (w/v) SDS, 10% (v/v) glycerol, 0.1% (w/v) bromophenol blue, 0.1 M DTT) at 65 °C for 5 min. Samples were loaded onto NuPage™ 4–12% Bis-Tris SDS gels (Thermo Fisher). Antibodies against the PK (V5) tag (Serotec, MCA1360) or the HA tag (Abcam, ab9110) were used for Western blotting.

For mass spectrometry analysis, a 4-l culture was harvested at an OD₆₀₀ of 1 and resuspended in 500 ml PBS. Again, one half of the sample was exposed to 10 J of 365-nm light, whereas the other half was kept in the dark. Cells were harvested by centrifugation. The pellet was washed with 45 ml lysis buffer (50 mM Tris-HCl, pH 7.5, 100 mM NaCl, 2.5 mM MgCl₂, 0.25% (v/v) Triton X-100) and resuspended in 15 ml lysis buffer containing 1 mM DTT, 1 mM PMSF and 2× cOmplete–EDTA protease inhibitors. Mechanical lysis was performed by cryogenic grinding (SPEX Freezer/Mill 6970). For the immunoprecipitation of Condensin complexes 100 µl protein A-coupled Dynabeads™ were pre-bound with 10 µg anti-PK antibody and then incubated with the lysate. Proteins were then eluted from the beads and separated using an SDS–PAGE. Proteins were visualized with Coomassie Blue. The crosslinked band in the +UV sample and a band at the same height in the –UV control were excised for analysis by mass spectrometry (Kschonsak et al., 2017).

4.2.4 SDS-PAGE

Prior to loading, protein samples were mixed with 5x SDS loading dye consisting of 250 mM Tris-HCl pH 6.8, 5 % (w/v) SDS, 50 % (v/v) glycerol, 100 mM DTT, 0.5 % (w/v) bromophenol blue boiled at 95 °C for 5 min and spun down in a table top

centrifuge (Eppendorf). *S. cerevisiae* condensin subunits were separated based on their size in NuPAGE™ 4–12% gradient Bis-Tris gels (ThermoFisher) at a constant 180 V for 80 min in MOPS buffer.

4.2.5 Coomassie staining

To visualize protein bands, SDS-gels were stained for 15 min at room temperature in Coomassie brilliant blue solution consisting of 0.2 % (w/v) Coomassie brilliant blue R-250, 45 % (v/v) ethanol and 10 % (v/v) acetic acid. Unspecific staining was removed by incubation of the gel for 15 min in destaining solution containing 30 % (v/v) methanol and 7 % (v/v) acetic acid.

4.2.6 Western blot

For western blotting, the semi-dry Trans-Blot Turbo Transfer System (Bio Rad) was used. Upon completion of an SDS-PAGE run, gels were briefly rinsed in Turbo Transfer buffer (Bio Rad) together with an equally sized nitrocellulose membrane. Protein were transferred from gel to membrane at 16.6 mA/cm² for 30 min. To avoid unspecific interactions, the membrane was blocked with freshly prepared western blot blocking solution for 1 h at room temperature. Antibodies were diluted (α -PK₆ 1: 5,000; α -HA₆ 1: 5,000; α -tubulin 1: 500) in blocking solution and added for 60 min at room temperature. After washing the membrane in TBS-T multiple times, secondary antibody was added as a dilution of 1:5,000 in blocking solution.

4.2.7 Yeast viability test

Yeast strains (**Table 3**) were created by integration of wild-type or mutant *ycg1* alleles under control of their native promoters into the *ura3* locus of diploid *YCG1/ycg1 Δ* strains. An empty plasmid was used as a negative control. After growing yeast cells on YEPD media, cells were sporulated at 30 °C for 2-3 days on SpoVB plates. To digest cell walls, cells were transferred to 0.9 M sorbitol containing 1 mg/ml zymolyase 100T (AMS Biotechnology) for 15 to 20 min at 30 °C. 5 μ l of the digested sample was distributed as a line on one side of a YEPD plate. A dissection microscope (Singer

MSM) was used to separate the spores. Pictures were taken after 3 days of growth at 25 °C.

4.2.8 Yeast expression test

10 ml of exponentially growing cells were harvested by centrifugation. Alkaline lysis was carried out by resuspending the pellet in 200 µl 100 mM NaOH and incubation of the mixture at room temperature for 10 min. Cellular material was again harvested by centrifugation and diluted in 1x SDS loading buffer. To adjust protein levels between samples the volume of 1x SDS loading buffer was adapted based on the density of the culture as determined by measuring the OD₆₀₀ (1 ml 1x SDS loading buffer/OD₆₀₀ unit). Samples were boiled at 80 °C for 5 min before being loaded onto an SDS gel.

4.2.9 Sequence alignment

Ycg1 sequence from ten fungi species (*Saccharomyces cerevisiae*, *Kluyveromyces lactis*, *Chaetomium thermophilum*, *Sclerotinia sclerotiorum*, *Emericella nidulans*, *Phaeosphaeria nodorum*, *Tuber melanosporum*, *Schizosaccharomyces pombe*, *Moniliophthora roreri*, *Encephalitozoon cuniculi*), ten animal species (*Homo sapiens*, *Mus musculus*, *Gallus gallus*, *Alligator mississippiensis*, *Xenopus laevis*, *Danio rerio*, *Callorhinchus milii*, *Apis mellifera*, *Daphnia pulex*, *Octopus bimaculoides*), 10 plant species (*Arabidopsis thaliana*, *Theobroma cacao*, *Glycine max*, *Populus trichocarpa*, *Vitis vinifera*, *Solanum lycopersicum*, *Beta vulgaris*, *Zea mays*, *Amborella trichopoda*, *Cyanidioschyzon merolae*) and five protist species (*Monosiga brevicollis*, *Dictyostelium discoideum*, *Phaeodactylum tricornutum*, *Saprolegnia parasitica*, *Guillardia theta*) were aligned using MAFFT (Kato et al., 2002) as described in Kschonsak et al., 2017.

4.3 Cryo-EM techniques

4.3.1 Cryo-EM sample preparation

Condensin apo state – untilted

For the untilted condensin apo state dataset, purified condensin at a concentration of 10.3 μM was thawed and diluted in a buffer containing 25 mM Hepes pH 7.5, 100 mM NaCl, 0.5% (v/v) glycerol, 1 mM MgCl_2 and 1 mM DTT to a final concentration of 0.4 μM . After glow discharging Quantifoil Au R2/2 mesh 200 grids for 40 seconds in a custom build glow discharger, 3 μl sample was applied to the carbon side of the grid. Using a Vitrobot Mark IV set to 10 °C and 100% humidity, the grid was plunge frozen in liquid ethane with 0 s wait and drain time, blot time 1 s and blot force 3.

Condensin apo state - tilted

The same approach was used for the tilted condensin apo dataset. Here, however, purified condensin at a concentration of 8.7 μM was diluted in a buffer containing 25 mM Hepes pH 7.5, 125 mM NaCl, 1 mM MgCl_2 and 1 mM DTT. To reduce beam induced movement of the grid, UltraAufoil R1.2/1.3 mesh 200 grids were used. Further, the blotting paper touching the top side of the grid was replaced by a teflon piece resulting in one-sided blotting from the bottom side of the grid. In addition, wait time was increased to 2 min prior to plunging.

Condensin +ATP state – tilted

For the tilted +nucleotide condensin dataset, the same procedure was applied as for the tilted apo dataset. In this case, purified condensin at a concentration of 8.7 μM was diluted in 25 mM Hepes pH 7.5, 125 mM NaCl, 1 mM MgCl_2 , 1 mM DTT, 1 mM ATP, 1 mM AMP-PNP and incubated for 15 min on ice prior to plunging.

Grids were stored until use in liquid nitrogen tanks.

4.3.2 Data acquisition

Automated data acquisition was performed using SerialEM (Mastronarde, 2005).

Condensin apo state – non-tilted

The dataset was collected on a FEI Talos Arctica operating at 200 keV and equipped with a Falcon 3 camera. Micrographs were recorded with $45 \text{ e}/\text{\AA}^2$ distributed over 10 frames at a magnification of 120,000x resulting in a pixel size of $1.207 \text{ \AA}/\text{pix}$. A total of 2755 micrographs were collected at a defocus range of $-3 \text{ }\mu\text{m}$ to $-1 \text{ }\mu\text{m}$.

Condensin apo state - tilted

Data was collected on a FEI Titan Krios operating at 300 keV equipped with a Quantum energy filter. Acquisition was carried out at a magnification of 105,000x and a pixel size of $1.35 \text{ \AA}/\text{pix}$ with $45 \text{ e}/\text{\AA}^2$ distributed over 40 frames. The defocus ranged from $-2.5 \text{ }\mu\text{m}$ to $-1 \text{ }\mu\text{m}$ and was monitored using Warp (Tegunov and Cramer, 2019). To compensate for preferred particle orientation, the stage was tilted to 38° during acquisition. Two datasets of 2953 and 3657 micrographs, respectively, were acquired independently.

Condensin +ATP state – tilted

Data acquisition was performed on a FEI Titan Krios operating at 300 keV equipped with a Quantum energy filter. A magnification of 81,000x was used resulting in a pixel size of $1.7 \text{ \AA}/\text{pix}$. Per micrograph $45 \text{ e}/\text{\AA}^2$ were distributed over 40 frames. The defocus range was set from $-2.5 \text{ }\mu\text{m}$ to $-1 \text{ }\mu\text{m}$. To address preferred particle orientation, the stage was tilted by 30° during acquisition. Two datasets of 4158 and 4894 micrographs, respectively, were acquired independently.

4.3.3 Data analysis

If not stated otherwise, data was analyzed using Relion 3.0 (Zivanov et al., n.d.). Resolution was determined after gold-standard refinement with two independent half-sets using the 0.143 FSC criterion (Rosenthal and Henderson, 2003).

Condensin apo state – non-tilted

Particle movement in 2755 micrographs was corrected by using the implementation of MotionCor2 in 5 x 5 patches with dose-weighting (Zheng et al., 2017). CTF values were estimated using GCTF (Zhang, 2016). After manually picking ~1,000 particles, a low resolution 2D template was generated to instruct autopicking. To avoid creating biases in picking, autopicking was set up with a low threshold to pick as many higher contrast objects as possible. A total of 446,087 particles were extracted in a box of 200^2 pixels with pixel size of 2.414 Å/pix. 2D classification in cryoSPARC 2 (Punjani et al., 2017) was used in several rounds to remove all obvious junk particles, contaminations or empty areas presumably caused by the low threshold used in autopicking. The resulting 130,717 cleaned up particles were used to create a *de novo* initial model in cryoSPARC 2 (Punjani et al., 2017). This model was used as a reference to align the particles by 3D classification with an offset search of 20 pixels and a limited E-step resolution of 10 Å into one class to account for off center particles. Particles were cleaned up by 2D classification without image alignment and a final run of 3D classification to yield a class that could be refined to 16.7 Å consisting of 29,996 particles.

Based on the first 3D map of the entire particle, 130,717 particles were re-centered on the arm segment and re-extracted with a boxsize of 130 pixels and a pixel size of 2.414 Å/pix. An initial model for the arm segment was created *de novo* in cryoSPARC 2 (Punjani et al., 2017) to serve as reference for the following 3D classification run with one class and an offset search of 20 pixels. A subsequent 3D classification resulted in a distinct class that was then refined to a resolution of 11.2 Å consisting of 52,297 particles.

Similar to the arm segment, particles were re-centered on the head segment with a box size of 100 pixels and a pixel size of 2.414 Å/pix. The 130,717 particles of the head segment were used to create an initial model *de novo* in cryoSAPRC 2 (Punjani et al., 2017). After compensating for off center particles by performing a 3D classification with one class and an offset search of 20 pixels using the initial model as reference, particles were classified further in 3D. Two classes were further refined.

One for the zipped apo state with a resolution of 9.7 Å containing 41,352 particles and one for the bridged state with a resolution of 12.7 Å containing 24,009 particles.

Condensin apo state – tilted

As described for the untilted condensin apo state dataset, pre-processing of two datasets consisting of 2953 and 3657 micrographs, respectively, was performed using MotionCorr 2 (Zheng et al., 2017) and GCTF (Zhang, 2016). Particles were autopicked based on a lowpass filtered 2D template, extracted in a box of 180 pixels (2.835 Å/pix) and carefully cleaned up in several rounds of 2D classification as described previously. An initial model was created *de novo* in cryoSPARC 2 (Punjani et al., 2017). A total of 281,678 particles from both datasets were subjected to 3D classification with one class and an offset search of 20 pixels. Duplicates were removed within a radius of 100 Å. A second round of 3D classification was used to separate the particles into four classes. One class corresponding to the bridged apo state was directly refined to a resolution of 12.2 Å consisting of 68,568 particles. For the zipped apo state, two of the four classes were combined and the resulting particles were separated into three classes. Of these three classes, one was refined to a resolution of 11.6 Å consisting of 77,158 particles.

As described for the untilted apo state dataset, focused refinement was used for the arm and the head segment. Particles for the arm segment were extracted in a box of 100 pixels (2.7 Å/pix) while the head segments were extracted in a box of 110 pixels (2.7 Å/pix). In both cases a 3D classification step with one class and an offset search of 20 pixels was used to compensate for off-center particles. In case of the arm segment, a subsequent round of 3D classification separated the particles into three classes of which one was further refined to a map with a resolution of 8.4 Å containing 104,128 particles. For the head segment, 281,678 particles were separated into eight classes. Class two was re-extracted in a 160 pix box (2.16 Å/pix) and refined to a map of 8 Å resolution containing 61,885 particles. Particles from classes six, seven and eight were pooled and subjected to another round of 3D classification. One of the resulting classes was subsequently refined to a map of 7.4 Å resolution containing 48,275 particles.

Condensin +ATP state – tilted

As described for the untilted condensin apo state dataset, pre-processing of 9,052 micrographs, separated into two datasets, was performed using MotionCorr (Zheng et al., 2017) and GCTF (Zhang, 2016) for each dataset independently. The remaining workflow is depicted in Fig. 2.16. After autopicking of particles in RELION based on a provided 2D template, particles were extracted with a box-size of 308 pixels (1.7 Å per pixel) binned to a box-size of 150 pixels. Several rounds of reference-free 2D classification in cryoSPARC 2 (Punjani et al., 2017) were used to discard obvious junk particles, contaminations and empty areas resulting in a total of 227,580 particles. Due to the high amount of heterogeneity, four initial models were generated in a reference-free manner using cryoSPARC 2 (Punjani et al., 2017). The four models were heterogeneously refined. To improve particle distribution among the classes, particles in each of the four classes were subjected to a second round of *de novo* initial model generation and heterogenous refinement. Upon visual inspection of the resulting 16 classes, similar looking classes were combined and refined independently (**Fig. 2.16**).

Based on the four final maps, particles were re-centered on the coiled coils in each class and re-extracted in a 90²-pixel box resulting in a pixel size of 3.4 Å. Coiled-coil particles were then pooled and subjected to a round of 3D classification with one class and an offset search of 20 pixel to compensate for off-centre particles. After removing duplicates within a range of 70 Å, particles were cleaned up by 2D and 3D classification without image alignment yielding a final map of 8.2 Å.

Similarly, particles were re-centered on the head segments of the final four maps of the full particles. In addition, a 2D template of the head segment low-pass filtered to 20 Å was used for autopicking. Particles from re-centering and autopicking were extracted with a box-size of 100 pixels, a pixel size of 2.448 Å and combined. Duplicates were removed within a radius of 70 Å. After cleaning up the particles by 2D classification, particles were subjected to 3D classification resulting in a distinct class that was refined to 7.6 Å and used for initial fitting of crystal structures. A subsequent 3D classification yielded a class with almost absent Smc2 coiled-coil density (7.9 Å) and a second class with improved Smc2 coiled-coil density (8.4 Å). The latter class was used to create a pseudoatomic model of the engaged condensin state.

4.3.4 Model building

Apo states

To create pseudo-atomic models of the head domain, the co-crystal structure of Smc4_{Brn1}-Ycs4_{Brn1} (PDB: 6QJ3) was rigid body docked into the cryo-EM head segment maps at 7.4 or 8 Å resolution for the zipped and the bridged state, respectively, using UCSF Chimera (Pettersen et al., 2004). A model for Smc2-Brn1_N was created by superimposition of the carboxy-terminal coiled coil of *Ct* Smc2 (PDB: 6QJ1) with the amino-terminal Brn1-HTH motif (PDB: 6QE6). Manual modifications were performed in COOT (Emsley and Cowtan, 2004). The model of Smc2-Brn1_N was manually placed into the cryo-EM density map of the head segment using UCSF Chimera (Pettersen et al., 2004). For the arm segment, the crystal structure of the *Sc* hinge with proximal coiled coils (PDB: 4RSI) was fitted into the cryo-EM density maps for the holo complexes at 11.6 or 12.2 Å resolution for the zipped and bridged state, respectively, as well as into the arm segment cryo-EM map at 8.4 Å resolution.

+ATP state

To build a model for the +ATP state, the *S. cerevisiae* crystal structure of Ycg1-Brn1_{Ycg1} (PDB: 5OQQ) was rigid body docked into the cryo-EM density map using UCSF chimera (Pettersen et al., 2004). Two changes were applied to the crystal structure. First, an extended helix (residues 499-507) that was only partially present in the crystal structure was manually added in COOT (Emsley and Cowtan, 2004). Second, the part of the Brn1 safety belt for which no density was present in the cryo-EM map (residues 458–496) was deleted. Next, to model the engaged Smc2-Smc4 heads, Smc4_{hd}-Brn1_C (PDB 6QJ2) and the helical and RecA-like half domains of the *C. thermophilum* Smc2_{hd} (PDB 6QJ1) were fitted into the cryo-EM map individually. The coiled coils of both heads were adjusted to the cryo-EM density with COOT (Emsley and Cowtan, 2004). A *S. cerevisiae* homology model was created using SWISS-MODEL (Waterhouse et al., 2018).

5. Contributions

Maria Sol Bravo purified *Sc* condensin holo complexes.

Léa Lecomte purified the *Ct* condensin subcomplexes Smc2-Smc4-Brn1_{N/C}, Ycs4-Brn1_{Ycs4}, Ycg1-Brn1_{Ycg1} and performed the analytical size exclusion experiments.

Marc Kschonsak with help of Lena Thaerichen performed the pioneering *in vivo* crosslinking experiments between Ycg1 and Smc2 and validated the physiological relevance of Ycg1 patch #1 mutant.

Catherine Stober, Saša Perovic and Markus Hassler validated the *in vivo* crosslinking experiments between Ycg1 and Smc2.

Markus Hassler created the Smc2-Brn1_N model, the pseudoatomic model for the engaged head segment and tested the physiological relevance of the Ycg1 patch #2 mutant with the help of Catherine Stober.

Byung-Gil Lee provided the high resolution maps of the *Sc* condensin holo complex in its apo state and accompanying models.

Francis O'Reilly and Ludwig Sinn performed and analyzed the crosslinking mass spectrometry experiments.

6. References

- Alipour, E., Marko, J.F., 2012. Self-organization of domain structures by DNA-loop-extruding enzymes. *Nucleic Acids Res.* 40, 11202–11212. <https://doi.org/10.1093/nar/gks925>
- Anderson, D.E., Losada, A., Erickson, H.P., Hirano, T., 2002. Condensin and cohesin display different arm conformations with characteristic hinge angles. *J. Cell Biol.* 156, 419–424. <https://doi.org/10.1083/jcb.200111002>
- Bak, A.L., Zeuthen, J., Crick, F.H., 1977. Higher-order structure of human mitotic chromosomes. *Proc. Natl. Acad. Sci.* 74, 1595–1599. <https://doi.org/10.1073/pnas.74.4.1595>
- Baldwin, P.R., Lyumkis, D., 2020. Non-uniformity of projection distributions attenuates resolution in Cryo-EM. *Prog. Biophys. Mol. Biol.* 150, 160–183. <https://doi.org/10.1016/j.pbiomolbio.2019.09.002>
- Baxter, J., Sen, N., Martínez, V.L., Carandini, M.E.M.D., Schvartzman, J.B., Diffley, J.F.X., Aragón, L., 2011. Positive Supercoiling of Mitotic DNA Drives Decatenation by Topoisomerase II in Eukaryotes. *Science* 331, 1328–1332. <https://doi.org/10.1126/science.1201538>
- Bazett-Jones, D.P., Kimura, K., Hirano, T., 2002. Efficient Supercoiling of DNA by a Single Condensin Complex as Revealed by Electron Spectroscopic Imaging. *Mol. Cell* 9, 1183–1190. [https://doi.org/10.1016/S1097-2765\(02\)00546-4](https://doi.org/10.1016/S1097-2765(02)00546-4)
- Bolzer, A., Kreth, G., Solovei, I., Koehler, D., Saracoglu, K., Fauth, C., Müller, S., Eils, R., Cremer, C., Speicher, M.R., Cremer, T., 2005. Three-Dimensional Maps of All Chromosomes in Human Male Fibroblast Nuclei and Prometaphase Rosettes. *PLoS Biol.* 3, e157. <https://doi.org/10.1371/journal.pbio.0030157>
- Bürmann, F., Lee, B.-G., Than, T., Sinn, L., O'Reilly, F.J., Yatskevich, S., Rappsilber, J., Hu, B., Nasmyth, K., Löwe, J., 2019. A folded conformation of MukBEF and cohesin. *Nat. Struct. Mol. Biol.* 26, 227–236. <https://doi.org/10.1038/s41594-019-0196-z>
- Cai, S., Chen, C., Tan, Z.Y., Huang, Y., Shi, J., Gan, L., 2018. Cryo-ET reveals the macromolecular reorganization of *S. pombe* mitotic chromosomes in vivo. *Proc. Natl. Acad. Sci.* 115, 10977–10982. <https://doi.org/10.1073/pnas.1720476115>
- Champoux, J.J., 2001. DNA Topoisomerases: Structure, Function, and Mechanism. *Annu. Rev. Biochem.* 70, 369–413. <https://doi.org/10.1146/annurev.biochem.70.1.369>
- Chang, L.-H., Ghosh, S., Noordermeer, D., 2020. TADs and Their Borders: Free Movement or Building a Wall? *J. Mol. Biol., Chromosome Hi C structure and function* 432, 643–652. <https://doi.org/10.1016/j.jmb.2019.11.025>
- Chapard, C., Jones, R., van Oepen, T., Scheinost, J.C., Nasmyth, K., 2019. Sister DNA Entrapment between Juxtaposed Smc Heads and Kleisin of the Cohesin

- Complex. Mol. Cell 75, 224-237.e5.
<https://doi.org/10.1016/j.molcel.2019.05.023>
- Chiu, A., Revenkova, E., Jessberger, R., 2004. DNA Interaction and Dimerization of Eukaryotic SMC Hinge Domains. *J. Biol. Chem.* 279, 26233–26242.
<https://doi.org/10.1074/jbc.M402439200>
- Ciosk, R., Shirayama, M., Shevchenko, Anna, Tanaka, T., Toth, A., Shevchenko, Andrej, Nasmyth, K., 2000. Cohesin's Binding to Chromosomes Depends on a Separate Complex Consisting of Scc2 and Scc4 Proteins. *Mol. Cell* 5, 243–254. [https://doi.org/10.1016/S1097-2765\(00\)80420-7](https://doi.org/10.1016/S1097-2765(00)80420-7)
- Cui, Y., Petrushenko, Z.M., Rybenkov, V.V., 2008. MukB acts as a macromolecular clamp in DNA condensation. *Nat. Struct. Mol. Biol.* 15, 411–418.
<https://doi.org/10.1038/nsmb.1410>
- Cuylen, S., Metz, J., Haering, C.H., 2011. Condensin structures chromosomal DNA through topological links. *Nat. Struct. Mol. Biol.* 18, 894–901.
<https://doi.org/10.1038/nsmb.2087>
- Davidson, I.F., Bauer, B., Goetz, D., Tang, W., Wutz, G., Peters, J.-M., 2019. DNA loop extrusion by human cohesin. *Science* 366, 1338–1345.
<https://doi.org/10.1126/science.aaz3418>
- Dekker, J., Rippe, K., Dekker, M., Kleckner, N., 2002. Capturing Chromosome Conformation. *Science* 295, 1306–1311.
<https://doi.org/10.1126/science.1067799>
- Diebold-Durand, M.-L., Lee, H., Ruiz Avila, L.B., Noh, H., Shin, H.-C., Im, H., Bock, F.P., Bürmann, F., Durand, A., Basfeld, A., Ham, S., Basquin, J., Oh, B.-H., Gruber, S., 2017. Structure of Full-Length SMC and Rearrangements Required for Chromosome Organization. *Mol. Cell* 67, 334-347.e5.
<https://doi.org/10.1016/j.molcel.2017.06.010>
- Dixon, J.R., Selvaraj, S., Yue, F., Kim, A., Li, Y., Shen, Y., Hu, M., Liu, J.S., Ren, B., 2012. Topological domains in mammalian genomes identified by analysis of chromatin interactions. *Nature* 485, 376–380.
<https://doi.org/10.1038/nature11082>
- Earnshaw, W.C., Laemmli, U.K., 1983. Architecture of metaphase chromosomes and chromosome scaffolds. *J. Cell Biol.* 96, 84–93.
<https://doi.org/10.1083/jcb.96.1.84>
- Eeftens, J.M., Bisht, S., Kerssemakers, J., Kschonsak, M., Haering, C.H., Dekker, C., 2017. Real-time detection of condensin-driven DNA compaction reveals a multistep binding mechanism. *EMBO J.* 36, 3448–3457.
<https://doi.org/10.15252/embj.201797596>
- Eeftens, J.M., Katan, A.J., Kschonsak, M., Hassler, M., de Wilde, L., Dief, E.M., Haering, C.H., Dekker, C., 2016. Condensin Smc2-Smc4 Dimers Are Flexible and Dynamic. *Cell Rep.* 14, 1813–1818.
<https://doi.org/10.1016/j.celrep.2016.01.063>

- Emsley, P., Cowtan, K., 2004. Coot: model-building tools for molecular graphics. *Acta Crystallogr. D Biol. Crystallogr.* 60, 2126–2132. <https://doi.org/10.1107/S0907444904019158>
- Finch, J.T., Klug, A., 1976. Solenoidal model for superstructure in chromatin. *Proc. Natl. Acad. Sci.* 73, 1897–1901. <https://doi.org/10.1073/pnas.73.6.1897>
- Fitzgerald, D.J., Berger, P., Schaffitzel, C., Yamada, K., Richmond, T.J., Berger, I., 2006. Protein complex expression by using multigene baculoviral vectors. *Nat. Methods* 3, 1021–1032. <https://doi.org/10.1038/nmeth983>
- Flemming, W., 1882. *Zellsubstanz, kern und zelltheilung.* Leipzig, F. C. W. Vogel.
- Fowler, W.E., Erickson, H.P., 1979. Trinodular structure of fibrinogen: Confirmation by both shadowing and negative stain electron microscopy. *J. Mol. Biol.* 134, 241–249. [https://doi.org/10.1016/0022-2836\(79\)90034-2](https://doi.org/10.1016/0022-2836(79)90034-2)
- Ganji, M., Shaltiel, I.A., Bisht, S., Kim, E., Kalichava, A., Haering, C.H., Dekker, C., 2018. Real-time imaging of DNA loop extrusion by condensin. *Science* 360, 102–105. <https://doi.org/10.1126/science.aar7831>
- Gasser, S.M., Laroche, T., Falquet, J., Boy de la Tour, E., Laemmli, U.K., 1986. Metaphase chromosome structure: Involvement of topoisomerase II. *J. Mol. Biol.* 188, 613–629. [https://doi.org/10.1016/S0022-2836\(86\)80010-9](https://doi.org/10.1016/S0022-2836(86)80010-9)
- Gerlich, D., Hirota, T., Koch, B., Peters, J.-M., Ellenberg, J., 2006. Condensin I Stabilizes Chromosomes Mechanically through a Dynamic Interaction in Live Cells. *Curr. Biol.* 16, 333–344. <https://doi.org/10.1016/j.cub.2005.12.040>
- Gibcus, J.H., Samejima, K., Goloborodko, A., Samejima, I., Naumova, N., Nuebler, J., Kanemaki, M.T., Xie, L., Paulson, J.R., Earnshaw, W.C., Mirny, L.A., Dekker, J., 2018. A pathway for mitotic chromosome formation. *Science* 359, eaao6135. <https://doi.org/10.1126/science.aao6135>
- Glaeser, R.M., Han, B.-G., 2017. Opinion: hazards faced by macromolecules when confined to thin aqueous films. *Biophys. Rep.* 3, 1–7. <https://doi.org/10.1007/s41048-016-0026-3>
- Gligoris, T., Löwe, J., 2016. Structural Insights into Ring Formation of Cohesin and Related Smc Complexes. *Trends Cell Biol.* 26, 680–693. <https://doi.org/10.1016/j.tcb.2016.04.002>
- Gligoris, T.G., Scheinost, J.C., Bürmann, F., Petela, N., Chan, K.-L., Uluocak, P., Beckouët, F., Gruber, S., Nasmyth, K., Löwe, J., 2014. Closing the cohesin ring: Structure and function of its Smc3-kleisin interface. *Science* 346, 963–967. <https://doi.org/10.1126/science.1256917>
- Goddard, T.D., Huang, C.C., Meng, E.C., Pettersen, E.F., Couch, G.S., Morris, J.H., Ferrin, T.E., 2018. UCSF ChimeraX: Meeting modern challenges in visualization and analysis. *Protein Sci. Publ. Protein Soc.* 27, 14–25. <https://doi.org/10.1002/pro.3235>

- Goloborodko, A., Imakaev, M.V., Marko, J.F., Mirny, L., 2016. Compaction and segregation of sister chromatids via active loop extrusion. *eLife* 5, e14864. <https://doi.org/10.7554/eLife.14864>
- Griese, J.J., Witte, G., Hopfner, K.-P., 2010. Structure and DNA binding activity of the mouse condensin hinge domain highlight common and diverse features of SMC proteins. *Nucleic Acids Res.* 38, 3454–3465. <https://doi.org/10.1093/nar/gkq038>
- Gruber, S., Haering, C.H., Nasmyth, K., 2003. Chromosomal Cohesin Forms a Ring. *Cell* 112, 765–777. [https://doi.org/10.1016/S0092-8674\(03\)00162-4](https://doi.org/10.1016/S0092-8674(03)00162-4)
- Guacci, V., Yamamoto, A., Strunnikov, A., Kingsbury, J., Hogan, E., Meluh, P., Koshland, D., 1993. Structure and Function of Chromosomes in Mitosis of Budding Yeast. *Cold Spring Harb. Symp. Quant. Biol.* 58, 677–685. <https://doi.org/10.1101/SQB.1993.058.01.075>
- Haering, C.H., Farcas, A.-M., Arumugam, P., Metson, J., Nasmyth, K., 2008. The cohesin ring concatenates sister DNA molecules. *Nature* 454, 297–301. <https://doi.org/10.1038/nature07098>
- Haering, C.H., Löwe, J., Hochwagen, A., Nasmyth, K., 2002. Molecular Architecture of SMC Proteins and the Yeast Cohesin Complex. *Mol. Cell* 9, 773–788. [https://doi.org/10.1016/S1097-2765\(02\)00515-4](https://doi.org/10.1016/S1097-2765(02)00515-4)
- Haering, C.H., Schoffnegger, D., Nishino, T., Helmhart, W., Nasmyth, K., Löwe, J., 2004. Structure and Stability of Cohesin's Smc1-Kleisin Interaction. *Mol. Cell* 15, 951–964. <https://doi.org/10.1016/j.molcel.2004.08.030>
- Hara, K., Kinoshita, K., Migita, T., Murakami, K., Shimizu, K., Takeuchi, K., Hirano, T., Hashimoto, H., 2019. Structural basis of HEAT-kleisin interactions in the human condensin I subcomplex. *EMBO Rep.* 20, e47183. <https://doi.org/10.15252/embr.201847183>
- Hassler, M., Shaltiel, I.A., Kschonsak, M., Simon, B., Merkel, F., Thärichen, L., Bailey, H.J., Macošek, J., Bravo, S., Metz, J., Hennig, J., Haering, C.H., 2019. Structural Basis of an Asymmetric Condensin ATPase Cycle. *Mol. Cell* 74, 1175-1188.e9. <https://doi.org/10.1016/j.molcel.2019.03.037>
- Higashi, T.L., Eickhoff, P., Sousa, J.S., Locke, J., Nans, A., Flynn, H.R., Snijders, A.P., Papageorgiou, G., O'Reilly, N., Chen, Z.A., O'Reilly, F.J., Rappsilber, J., Costa, A., Uhlmann, F., 2020. A Structure-Based Mechanism for DNA Entry into the Cohesin Ring. *Mol. Cell*. <https://doi.org/10.1016/j.molcel.2020.07.013>
- Hirano, T., 2012. Condensins: universal organizers of chromosomes with diverse functions. *Genes Dev.* 26, 1659–1678. <https://doi.org/10.1101/gad.194746.112>
- Hirano, T., Kobayashi, R., Hirano, M., 1997. Condensins, Chromosome Condensation Protein Complexes Containing XCAP-C, XCAP-E and a Xenopus Homolog of the Drosophila Barren Protein. *Cell* 89, 511–521. [https://doi.org/10.1016/S0092-8674\(00\)80233-0](https://doi.org/10.1016/S0092-8674(00)80233-0)

- Hirano, T., Mitchison, T.J., 1994. A heterodimeric coiled-coil protein required for mitotic chromosome condensation in vitro. *Cell* 79, 449–458. [https://doi.org/10.1016/0092-8674\(94\)90254-2](https://doi.org/10.1016/0092-8674(94)90254-2)
- Hirota, T., Gerlich, D., Koch, B., Ellenberg, J., Peters, J.-M., 2004. Distinct functions of condensin I and II in mitotic chromosome assembly. *J. Cell Sci.* 117, 6435–6445. <https://doi.org/10.1242/jcs.01604>
- Holm, C., 1994. Coming undone: How to untangle a chromosome. *Cell* 77, 955–957. [https://doi.org/10.1016/0092-8674\(94\)90433-2](https://doi.org/10.1016/0092-8674(94)90433-2)
- Holm, C., Goto, T., Wang, J.C., Botstein, D., 1985. DNA topoisomerase II is required at the time of mitosis in yeast. *Cell* 41, 553–563. [https://doi.org/10.1016/S0092-8674\(85\)80028-3](https://doi.org/10.1016/S0092-8674(85)80028-3)
- Hons, M.T., Huis in 't Veld, P.J., Kaesler, J., Rombaut, P., Schleiffer, A., Herzog, F., Stark, H., Peters, J.-M., 2016. Topology and structure of an engineered human cohesin complex bound to Pds5B. *Nat. Commun.* 7, 12523. <https://doi.org/10.1038/ncomms12523>
- Hopfner, K.-P., 2016. Invited review: Architectures and mechanisms of ATP binding cassette proteins. *Biopolymers* 105, 492–504. <https://doi.org/10.1002/bip.22843>
- Hopfner, K.-P., Tainer, J.A., 2003. Rad50/SMC proteins and ABC transporters: unifying concepts from high-resolution structures. *Curr. Opin. Struct. Biol.* 13, 249–255. [https://doi.org/10.1016/s0959-440x\(03\)00037-x](https://doi.org/10.1016/s0959-440x(03)00037-x)
- Houlard, M., Godwin, J., Metson, J., Lee, J., Hirano, T., Nasmyth, K., 2015. Condensin confers the longitudinal rigidity of chromosomes. *Nat. Cell Biol.* 17, 771–781. <https://doi.org/10.1038/ncb3167>
- Juan, G., Pan, W., Darzynkiewicz, Z., 1996. DNA Segments Sensitive to Single-Strand-Specific Nucleases Are Present in Chromatin of Mitotic Cells. *Exp. Cell Res.* 227, 197–202. <https://doi.org/10.1006/excr.1996.0267>
- Kagawa, R., Montgomery, M.G., Braig, K., Leslie, A.G.W., Walker, J.E., 2004. The structure of bovine F1-ATPase inhibited by ADP and beryllium fluoride. *EMBO J.* 23, 2734–2744. <https://doi.org/10.1038/sj.emboj.7600293>
- Kania, A., Salzberg, A., Bhat, M., D'Evelyn, D., He, Y., Kiss, I., Bellen, H.J., 1995. P-element mutations affecting embryonic peripheral nervous system development in *Drosophila melanogaster*. *Genetics* 139, 1663–1678.
- Käshammer, L., Saathoff, J.-H., Lammens, K., Gut, F., Bartho, J., Alt, A., Kessler, B., Hopfner, K.-P., 2019. Mechanism of DNA End Sensing and Processing by the Mre11-Rad50 Complex. *Mol. Cell* 76, 382–394.e6. <https://doi.org/10.1016/j.molcel.2019.07.035>
- Katoh, K., Misawa, K., Kuma, K., Miyata, T., 2002. MAFFT: a novel method for rapid multiple sequence alignment based on fast Fourier transform. *Nucleic Acids Res.* 30, 3059–3066. <https://doi.org/10.1093/nar/gkf436>

- Keenholtz, R.A., Dhanaraman, T., Palou, R., Yu, J., D'Amours, D., Marko, J.F., 2017. Oligomerization and ATP stimulate condensin-mediated DNA compaction. *Sci. Rep.* 7, 1–13. <https://doi.org/10.1038/s41598-017-14701-5>
- Kim, Y., Shi, Z., Zhang, H., Finkelstein, I.J., Yu, H., 2019. Human cohesin compacts DNA by loop extrusion. *Science* 366, 1345–1349. <https://doi.org/10.1126/science.aaz4475>
- Kimura, K., Hirano, T., 1997. ATP-Dependent Positive Supercoiling of DNA by 13S Condensin: A Biochemical Implication for Chromosome Condensation. *Cell* 90, 625–634. [https://doi.org/10.1016/S0092-8674\(00\)80524-3](https://doi.org/10.1016/S0092-8674(00)80524-3)
- King, T.D., Leonard, C.J., Cooper, J.C., Nguyen, S., Joyce, E.F., Phadnis, N., 2019. Recurrent Losses and Rapid Evolution of the Condensin II Complex in Insects. *Mol. Biol. Evol.* 36, 2195–2204. <https://doi.org/10.1093/molbev/msz140>
- Kreuzer, K.N., Cozzarelli, N.R., 1980. Formation and resolution of DNA catenanes by DNA gyrase. *Cell* 20, 245–254. [https://doi.org/10.1016/0092-8674\(80\)90252-4](https://doi.org/10.1016/0092-8674(80)90252-4)
- Kschonsak, M., Merkel, F., Bisht, S., Metz, J., Rybin, V., Hassler, M., Haering, C.H., 2017. Structural Basis for a Safety-Belt Mechanism That Anchors Condensin to Chromosomes. *Cell* 171, 588–600.e24. <https://doi.org/10.1016/j.cell.2017.09.008>
- Lee, B.-G., Merkel, F., Allegretti, M., Hassler, M., Cawood, C., Lecomte, L., O'Reilly, F.J., Sinn, L.R., Gutierrez-Escribano, P., Kschonsak, M., Bravo, S., Nakane, T., Rappsilber, J., Aragon, L., Beck, M., Löwe, J., Haering, C.H., 2020. Cryo-EM structures of holo condensin reveal a subunit flip-flop mechanism. *Nat. Struct. Mol. Biol.* 27, 743–751. <https://doi.org/10.1038/s41594-020-0457-x>
- Lewis, C.D., Laemmli, U.K., 1982. Higher order metaphase chromosome structure: Evidence for metalloprotein interactions. *Cell* 29, 171–181. [https://doi.org/10.1016/0092-8674\(82\)90101-5](https://doi.org/10.1016/0092-8674(82)90101-5)
- Lieberman-Aiden, E., Berkum, N.L. van, Williams, L., Imakaev, M., Ragozy, T., Telling, A., Amit, I., Lajoie, B.R., Sabo, P.J., Dorschner, M.O., Sandstrom, R., Bernstein, B., Bender, M.A., Groudine, M., Gnirke, A., Stamatoyannopoulos, J., Mirny, L.A., Lander, E.S., Dekker, J., 2009. Comprehensive Mapping of Long-Range Interactions Reveals Folding Principles of the Human Genome. *Science* 326, 289–293. <https://doi.org/10.1126/science.1181369>
- Liu, Y., Sung, S., Kim, Y., Li, F., Gwon, G., Jo, A., Kim, A.-K., Kim, T., Song, O., Lee, S.E., Cho, Y., 2016. ATP-dependent DNA binding, unwinding, and resection by the Mre11/Rad50 complex. *EMBO J.* 35, 743–758. <https://doi.org/10.15252/embj.201592462>
- Luger, K., Mäder, A.W., Richmond, R.K., Sargent, D.F., Richmond, T.J., 1997. Crystal structure of the nucleosome core particle at 2.8 Å resolution. *Nature* 389, 251–260. <https://doi.org/10.1038/38444>
- Maeshima, K., Laemmli, U.K., 2003. A Two-Step Scaffolding Model for Mitotic Chromosome Assembly. *Dev. Cell* 4, 467–480. [https://doi.org/10.1016/S1534-5807\(03\)00092-3](https://doi.org/10.1016/S1534-5807(03)00092-3)

- Manalastas-Cantos, K., Kschonsak, M., Haering, C.H., Svergun, D.I., 2019. Solution structure and flexibility of the condensin HEAT-repeat subunit Ycg1. *J. Biol. Chem.* 294, 13822–13829. <https://doi.org/10.1074/jbc.RA119.008661>
- Marko, J.F., 2008. Micromechanical studies of mitotic chromosomes. *Chromosome Res.* 16, 469–497. <https://doi.org/10.1007/s10577-008-1233-7>
- Mastronarde, D.N., 2005. Automated electron microscope tomography using robust prediction of specimen movements. *J. Struct. Biol.* 152, 36–51. <https://doi.org/10.1016/j.jsb.2005.07.007>
- McDowell, A.W., Smith, J.M., Dubochet, J., 1986. Cryo-electron microscopy of vitrified chromosomes in situ. *EMBO J.* 5, 1395–1402. <https://doi.org/10.1002/j.1460-2075.1986.tb04373.x>
- Melby, T.E., Ciampaglio, C.N., Briscoe, G., Erickson, H.P., 1998. The Symmetrical Structure of Structural Maintenance of Chromosomes (SMC) and MukB Proteins: Long, Antiparallel Coiled Coils, Folded at a Flexible Hinge. *J. Cell Biol.* 142, 1595–1604. <https://doi.org/10.1083/jcb.142.6.1595>
- Meselson, M., Stahl, F.W., 1958. THE REPLICATION OF DNA IN *ESCHERICHIA COLI**. *Proc. Natl. Acad. Sci. U. S. A.* 44, 671–682.
- Muir, K.W., Li, Y., Weis, F., Panne, D., 2020. The structure of the cohesin ATPase elucidates the mechanism of SMC–kleisin ring opening. *Nat. Struct. Mol. Biol.* 27, 233–239. <https://doi.org/10.1038/s41594-020-0379-7>
- Nasmyth, K., 2001. Disseminating the Genome: Joining, Resolving, and Separating Sister Chromatids During Mitosis and Meiosis. *Annu. Rev. Genet.* 35, 673–745. <https://doi.org/10.1146/annurev.genet.35.102401.091334>
- Naumova, N., Imakaev, M., Fudenberg, G., Zhan, Y., Lajoie, B.R., Mirny, L.A., Dekker, J., 2013. Organization of the Mitotic Chromosome. *Science* 342, 948–953. <https://doi.org/10.1126/science.1236083>
- Naydenova, K., Russo, C.J., 2017. Measuring the effects of particle orientation to improve the efficiency of electron cryomicroscopy. *Nat. Commun.* 8, 629. <https://doi.org/10.1038/s41467-017-00782-3>
- Noble, A.J., Dandey, V.P., Wei, H., Brasch, J., Chase, J., Acharya, P., Tan, Y.Z., Zhang, Z., Kim, L.Y., Scapin, G., Rapp, M., Eng, E.T., Rice, W.J., Cheng, A., Negro, C.J., Shapiro, L., Kwong, P.D., Jeruzalmi, D., des Georges, A., Potter, C.S., Carragher, B., 2018. Routine single particle CryoEM sample and grid characterization by tomography. *eLife* 7, e34257. <https://doi.org/10.7554/eLife.34257>
- Nora, E.P., Lajoie, B.R., Schulz, E.G., Giorgetti, L., Okamoto, I., Servant, N., Piolot, T., Berkum, N.L. van, Meisig, J., Sedat, J., Gribnau, J., Barillot, E., Blüthgen, N., Dekker, J., Heard, E., 2012. Spatial partitioning of the regulatory landscape of the X-inactivation centre. *Nature* 485, 381–385. <https://doi.org/10.1038/nature11049>

- Olins, A.L., Olins, D.E., 1974. Spheroid Chromatin Units (v Bodies). *Science* 183, 330–332. <https://doi.org/10.1126/science.183.4122.330>
- Onn, I., Aono, N., Hirano, M., Hirano, T., 2007. Reconstitution and subunit geometry of human condensin complexes. *EMBO J.* 26, 1024–1034. <https://doi.org/10.1038/sj.emboj.7601562>
- Ono, T., Losada, A., Hirano, M., Myers, M.P., Neuwald, A.F., Hirano, T., 2003. Differential Contributions of Condensin I and Condensin II to Mitotic Chromosome Architecture in Vertebrate Cells. *Cell* 115, 109–121. [https://doi.org/10.1016/S0092-8674\(03\)00724-4](https://doi.org/10.1016/S0092-8674(03)00724-4)
- Ou, H.D., Phan, S., Deerinck, T.J., Thor, A., Ellisman, M.H., O'Shea, C.C., 2017. ChromEMT: Visualizing 3D chromatin structure and compaction in interphase and mitotic cells. *Science* 357. <https://doi.org/10.1126/science.aag0025>
- Paulson, J.R., Laemmli, U.K., 1977. The structure of histone-depleted metaphase chromosomes. *Cell* 12, 817–828. [https://doi.org/10.1016/0092-8674\(77\)90280-X](https://doi.org/10.1016/0092-8674(77)90280-X)
- Peter, B.J., Ullsperger, C., Hiasa, H., Mariani, K.J., Cozzarelli, N.R., 1998. The Structure of Supercoiled Intermediates in DNA Replication. *Cell* 94, 819–827. [https://doi.org/10.1016/S0092-8674\(00\)81740-7](https://doi.org/10.1016/S0092-8674(00)81740-7)
- Peterson, C.L., 1994. The SMC family: Novel motor proteins for chromosome condensation? *Cell* 79, 389–392. [https://doi.org/10.1016/0092-8674\(94\)90247-X](https://doi.org/10.1016/0092-8674(94)90247-X)
- Pettersen, E.F., Goddard, T.D., Huang, C.C., Couch, G.S., Greenblatt, D.M., Meng, E.C., Ferrin, T.E., 2004. UCSF Chimera—a visualization system for exploratory research and analysis. *J. Comput. Chem.* 25, 1605–1612. <https://doi.org/10.1002/jcc.20084>
- Piazza, I., Rutkowska, A., Ori, A., Walczak, M., Metz, J., Pelechano, V., Beck, M., Haering, C.H., 2014. Association of condensin with chromosomes depends on DNA binding by its HEAT-repeat subunits. *Nat. Struct. Mol. Biol.* 21, 560–568. <https://doi.org/10.1038/nsmb.2831>
- Piovesan, A., Pelleri, M.C., Antonaros, F., Strippoli, P., Caracausi, M., Vitale, L., 2019. On the length, weight and GC content of the human genome. *BMC Res. Notes* 12, 106. <https://doi.org/10.1186/s13104-019-4137-z>
- Poirier, M.G., Marko, J.F., 2002. Mitotic chromosomes are chromatin networks without a mechanically contiguous protein scaffold. *Proc. Natl. Acad. Sci. U. S. A.* 99, 15393–15397. <https://doi.org/10.1073/pnas.232442599>
- Promonet, A., Padiou, I., Liu, Y., Sanz, L., Biernacka, A., Schmitz, A.-L., Skrzypczak, M., Sarrazin, A., Mettling, C., Rowicka, M., Ginalska, K., Chedin, F., Chen, C.-L., Lin, Y.-L., Pasero, P., 2020. Topoisomerase 1 prevents replication stress at R-loop-enriched transcription termination sites. *Nat. Commun.* 11, 3940. <https://doi.org/10.1038/s41467-020-17858-2>

- Punjani, A., Rubinstein, J.L., Fleet, D.J., Brubaker, M.A., 2017. cryoSPARC: algorithms for rapid unsupervised cryo-EM structure determination. *Nat. Methods* 14, 290–296. <https://doi.org/10.1038/nmeth.4169>
- Rattner, J.B., Hamkalo, B A, 1978. Higher order structure in metaphase chromosomes. *Chromosoma* 69, 373–379.
- Riggs, A.D., Holliday, R., Monk, M., Pugh, J.E., 1990. DNA methylation and late replication probably aid cell memory, and type I DNA reeling could aid chromosome folding and enhancer function. *Philos. Trans. R. Soc. Lond. B Biol. Sci.* 326, 285–297. <https://doi.org/10.1098/rstb.1990.0012>
- Robinson, P.J.J., Fairall, L., Huynh, V.A.T., Rhodes, D., 2006. EM measurements define the dimensions of the “30-nm” chromatin fiber: Evidence for a compact, interdigitated structure. *Proc. Natl. Acad. Sci.* 103, 6506–6511. <https://doi.org/10.1073/pnas.0601212103>
- Rojowska, A., Lammens, K., Seifert, F.U., Drenth, C., Feldmann, H., Hopfner, K.-P., 2014. Structure of the Rad50 DNA double-strand break repair protein in complex with DNA. *EMBO J.* 33, 2847–2859. <https://doi.org/10.15252/embj.201488889>
- Rosenthal, P.B., Henderson, R., 2003. Optimal Determination of Particle Orientation, Absolute Hand, and Contrast Loss in Single-particle Electron Cryomicroscopy. *J. Mol. Biol.* 333, 721–745. <https://doi.org/10.1016/j.jmb.2003.07.013>
- Ryu, J., Katan A.J., van der Sluis E.O., Wisse T., de Groot R., Haering C., Dekker C. 2019. AFM images of open and collapsed states of yeast condensin suggest a scrunching model for DNA loop extrusion. *BioArchive*. <https://doi.org/10.1101/2019.12.13.867358>
- Saitoh, N., Goldberg, I.G., Wood, E.R., Earnshaw, W.C., 1994. ScII: An Abundant Chromosome Scaffold Protein Is a Member of a Family of Putative ATPases with an Unusual Predicted Tertiary Structure. *J. Cell Biol.* 127, 16.
- Sakai, A., Hizume, K., Sutani, T., Takeyasu, K., Yanagida, M., 2003a. Condensin but not cohesin SMC heterodimer induces DNA reannealing through protein–protein assembly. *EMBO J.* 22, 2764–2775. <https://doi.org/10.1093/emboj/cdg247>
- Sakai, A., Hizume, K., Sutani, T., Takeyasu, K., Yanagida, M., 2003b. Condensin but not cohesin SMC heterodimer induces DNA reannealing through protein–protein assembly. *EMBO J.* 22, 2764–2775. <https://doi.org/10.1093/emboj/cdg247>
- Schindelin, J., Arganda-Carreras, I., Frise, E., Kaynig, V., Longair, M., Pietzsch, T., Preibisch, S., Rueden, C., Saalfeld, S., Schmid, B., Tinevez, J.-Y., White, D.J., Hartenstein, V., Eliceiri, K., Tomancak, P., Cardona, A., 2012. Fiji: an open-source platform for biological-image analysis. *Nat. Methods* 9, 676–682. <https://doi.org/10.1038/nmeth.2019>
- Schmiesing, J.A., Ball, A.R., Gregson, H.C., Alderton, J.M., Zhou, S., Yokomori, K., 1998. Identification of two distinct human SMC protein complexes involved in

- mitotic chromosome dynamics. *Proc. Natl. Acad. Sci. U. S. A.* 95, 12906–12911.
- Shi, Z., Gao, H., Bai, X., Yu, H., 2020. Cryo-EM structure of the human cohesin-NIPBL-DNA complex. *Science* 368, 1454–1459. <https://doi.org/10.1126/science.abb0981>
- Shintomi, K., Takahashi, T.S., Hirano, T., 2015. Reconstitution of mitotic chromatids with a minimum set of purified factors. *Nat. Cell Biol.* 17, 1014–1023. <https://doi.org/10.1038/ncb3187>
- Soh, Y.-M., Bürmann, F., Shin, H.-C., Oda, T., Jin, K.S., Toseland, C.P., Kim, C., Lee, H., Kim, S.J., Kong, M.-S., Durand-Diebold, M.-L., Kim, Y.-G., Kim, H.M., Lee, N.K., Sato, M., Oh, B.-H., Gruber, S., 2015. Molecular Basis for SMC Rod Formation and Its Dissolution upon DNA Binding. *Mol. Cell* 57, 290–303. <https://doi.org/10.1016/j.molcel.2014.11.023>
- Spell, R.M., Holm, C., 1994. Nature and distribution of chromosomal intertwinings in *Saccharomyces cerevisiae*. *Mol. Cell. Biol.* 14, 1465–1476. <https://doi.org/10.1128/MCB.14.2.1465>
- Staynov, D.Z., 2000. DNase I digestion reveals alternating asymmetrical protection of the nucleosome by the higher order chromatin structure. *Nucleic Acids Res.* 28, 3092–3099. <https://doi.org/10.1093/nar/28.16.3092>
- Stray, J.E., Lindsley, J.E., 2003. Biochemical Analysis of the Yeast Condensin Smc2/4 Complex AN ATPase THAT PROMOTES KNOTTING OF CIRCULAR DNA. *J. Biol. Chem.* 278, 26238–26248. <https://doi.org/10.1074/jbc.M302699200>
- Strick, T.R., Kawaguchi, T., Hirano, T., 2004. Real-Time Detection of Single-Molecule DNA Compaction by Condensin I. *Curr. Biol.* 14, 874–880. <https://doi.org/10.1016/j.cub.2004.04.038>
- Strunnikov, A.V., Hogan, E., Koshland, D., 1995. SMC2, a *Saccharomyces cerevisiae* gene essential for chromosome segregation and condensation, defines a subgroup within the SMC family. *Genes Dev.* 9, 587–599. <https://doi.org/10.1101/gad.9.5.587>
- Sundin, O., Varshavsky, A., 1981. Arrest of segregation leads to accumulation of highly intertwined catenated dimers: Dissection of the final stages of SV40 DNA replication. *Cell* 25, 659–669. [https://doi.org/10.1016/0092-8674\(81\)90173-2](https://doi.org/10.1016/0092-8674(81)90173-2)
- Takata, H., Madung, M., Katoh, K., Fukui, K., 2018. Cdk1-dependent phosphorylation of KIF4A at S1186 triggers lateral chromosome compaction during early mitosis. *PLoS ONE* 13. <https://doi.org/10.1371/journal.pone.0209614>
- Tan, Y.Z., Baldwin, P.R., Davis, J.H., Williamson, J.R., Potter, C.S., Carragher, B., Lyumkis, D., 2017. Addressing preferred specimen orientation in single-particle cryo-EM through tilting. *Nat. Methods* 14, 793–796. <https://doi.org/10.1038/nmeth.4347>
- Taylor, K.A., Glaeser, R.M., 2008. Retrospective on the early development of cryoelectron microscopy of macromolecules and a prospective on opportunities

- for the future. *J. Struct. Biol.*, JSB 50th Anniversary Issue 163, 214–223. <https://doi.org/10.1016/j.jsb.2008.06.004>
- Tegunov, D., Cramer, P., 2019. Real-time cryo-electron microscopy data preprocessing with Warp. *Nat. Methods* 16, 1146–1152. <https://doi.org/10.1038/s41592-019-0580-y>
- Terakawa, T., Bisht, S., Eeftens, J.M., Dekker, C., Haering, C.H., Greene, E.C., 2017. The condensin complex is a mechanochemical motor that translocates along DNA. *Science* 358, 672–676. <https://doi.org/10.1126/science.aan6516>
- Tsao, Y.-P., Wu, H.-Y., Liu, L.F., 1989. Transcription-driven supercoiling of DNA: Direct biochemical evidence from in vitro studies. *Cell* 56, 111–118. [https://doi.org/10.1016/0092-8674\(89\)90989-6](https://doi.org/10.1016/0092-8674(89)90989-6)
- Tuduri, S., Crabbé, L., Conti, C., Tourrière, H., Holtgreve-Grez, H., Jauch, A., Pantesco, V., De Vos, J., Thomas, A., Theillet, C., Pommier, Y., Tazi, J., Coquelle, A., Pasero, P., 2009. Topoisomerase I suppresses genomic instability by preventing interference between replication and transcription. *Nat. Cell Biol.* 11, 1315–1324. <https://doi.org/10.1038/ncb1984>
- Uemura, T., Ohkura, H., Adachi, Y., Morino, K., Dr. Mubarak Abu Mraheil, Shiozaki, K., Yanagida, M., 1987. DNA topoisomerase II is required for condensation and separation of mitotic chromosomes in *S. pombe*. *Cell* 50, 917–925. [https://doi.org/10.1016/0092-8674\(87\)90518-6](https://doi.org/10.1016/0092-8674(87)90518-6)
- Vagnarelli, P., Hudson, D.F., Ribeiro, S.A., Trinkle-Mulcahy, L., Spence, J.M., Lai, F., Farr, C.J., Lamond, A.I., Earnshaw, W.C., 2006. Condensin and Repo-Man–PP1 co-operate in the regulation of chromosome architecture during mitosis. *Nat. Cell Biol.* 8, 1133–1142. <https://doi.org/10.1038/ncb1475>
- Vazquez Nunez, R., Ruiz Avila, L.B., Gruber, S., 2019. Transient DNA Occupancy of the SMC Interarm Space in Prokaryotic Condensin. *Mol. Cell* 75, 209–223.e6. <https://doi.org/10.1016/j.molcel.2019.05.001>
- Walther, N., Hossain, M.J., Politi, A.Z., Koch, B., Kueblbeck, M., Ødegård-Fougner, Ø., Lampe, M., Ellenberg, J., 2018. A quantitative map of human Condensins provides new insights into mitotic chromosome architecture. *J. Cell Biol.* 217, 2309–2328. <https://doi.org/10.1083/jcb.201801048>
- Wang, B.-D., Eyre, D., Basrai, M., Lichten, M., Strunnikov, A., 2005. Condensin Binding at Distinct and Specific Chromosomal Sites in the *Saccharomyces cerevisiae* Genome. *Mol. Cell. Biol.* 25, 7216–7225. <https://doi.org/10.1128/MCB.25.16.7216-7225.2005>
- Waterhouse, A., Bertoni, M., Bienert, S., Studer, G., Tauriello, G., Gumienny, R., Heer, F.T., de Beer, T.A.P., Rempfer, C., Bordoli, L., Lepore, R., Schwede, T., 2018. SWISS-MODEL: homology modelling of protein structures and complexes. *Nucleic Acids Res.* 46, W296–W303. <https://doi.org/10.1093/nar/gky427>
- Wells, J.N., Gligoris, T.G., Nasmyth, K.A., Marsh, J.A., 2017. Evolution of condensin and cohesin complexes driven by replacement of Kite by Hawk proteins. *Curr. Biol.* 27, R17–R18. <https://doi.org/10.1016/j.cub.2016.11.050>

- Wischnitzer, S., 1973. The Submicroscopic Morphology of the Interphase Nucleus, in: *International Review of Cytology*. Elsevier, pp. 1–48. [https://doi.org/10.1016/S0074-7696\(08\)61933-6](https://doi.org/10.1016/S0074-7696(08)61933-6)
- Xu, Y.-X., Manley, J.L., 2007. The Prolyl Isomerase Pin1 Functions in Mitotic Chromosome Condensation. *Mol. Cell* 26, 287–300. <https://doi.org/10.1016/j.molcel.2007.03.020>
- Yeong, F.M., Hombauer, H., Wendt, K.S., Hirota, T., Mudrak, I., Mechtler, K., Loregger, T., Marchler-Bauer, A., Tanaka, K., Peters, J.-M., Ogris, E., 2003. Identification of a Subunit of a Novel Kleisin- β /SMC Complex as a Potential Substrate of Protein Phosphatase 2A. *Curr. Biol.* 13, 2058–2064. <https://doi.org/10.1016/j.cub.2003.10.032>
- Yuen, K.C., Slaughter, B.D., Gerton, J.L., 2017. Condensin II is anchored by TFIIIC and H3K4me3 in the mammalian genome and supports the expression of active dense gene clusters. *Sci. Adv.* 3, e1700191. <https://doi.org/10.1126/sciadv.1700191>
- Zhang, K., 2016. Gctf: Real-time CTF determination and correction. *J. Struct. Biol.* 193, 1–12. <https://doi.org/10.1016/j.jsb.2015.11.003>
- Zheng, S.Q., Palovcak, E., Armache, J.-P., Verba, K.A., Cheng, Y., Agard, D.A., 2017. MotionCor2: anisotropic correction of beam-induced motion for improved cryo-electron microscopy. *Nat. Methods* 14, 331–332. <https://doi.org/10.1038/nmeth.4193>
- Zivanov, J., Nakane, T., Forsberg, B.O., Kimanius, D., Hagen, W.J., Lindahl, E., Scheres, S.H., n.d. New tools for automated high-resolution cryo-EM structure determination in RELION-3. *eLife* 7. <https://doi.org/10.7554/eLife.42166>

7. Supplementary Information

7.1 Abbreviations

3C	chromosome conformation capture
ABC	ATP binding cassette
AFM	atomic force microscopy
AMP-PNP	adenyl imidodiphosphate
ATP	adenosine triphosphate
bp	base pairs
BPA	p-benzoyl-L-phenylalanine
ChIP-Seq	chromatin immunoprecipitation followed by sequencing
Cryo-EM	cryogenic electron microscopy
<i>Ct</i>	<i>Chaetomium thermophilum</i>
CTF	contrast transfer function
DNA	deoxyribonucleic acid
dsDN	double stranded DNA
DTT	dithiothreitol
<i>E. coli</i>	<i>Escherichia coli</i>
FCS	fluorescence correlated spectroscopy
FRAP	Fluorescence recovery after photobleaching
FSC	fourier shell correlation
HEAT	huntingtin, elongation factor 3F, PP2A, Tor1
Hi-C	high throughput sequencing 3C
<i>Hs</i>	<i>Homo sapiens</i>
HTH	helix-turn-helix
kb	kilo base pairs
LECA	last eukaryote common ancestor
NEBD	nuclear envelope breakdown
<i>Sc</i>	<i>Saccharomyces cerevisiae</i>
SDS-PAGE	sodium dodecyl sulfate polyacrylamide gel electrophoresis
SMC	structural maintenance of chromosomes
Smc2 ^{hd}	Smc2 head domain
SPA	single particle analysis
ssDNA	single stranded DNA
tRNA	transfer ribonucleic acid
WHD	winged helix domain

7.2 List of Figures

Figure 1.1: 3D organization of chromosomes.....	3
Figure 1.2: The condensin complex.	8
Figure 1.3: Subunit composition of condensin.....	14
Figure 1.4: Architecture of the condensin holo complex.....	16
Figure 2.1: Purification of the <i>S. cerevisiae</i> condensin holo complex.....	20
Figure 2.2: Cryo-EM of <i>S. cerevisiae</i> holo condensin.....	22
Figure 2.3: Processing workflow and structure of the entire particle.	24
Figure 2.4: Focused refinement of the arm segment.....	25
Figure 2.5: Focused refinement of the head segment.....	27
Figure 2.6: Angular distribution of the particles.	28
Figure 2.7: The effect of stage tilting.	29
Figure 2.8: Processing workflow after stage tilting in absence of ATP..	30
Figure 2.9: Entire particle after stage tilting.	32
Figure 2.10: Arm segment after stage tilting.....	33
Figure 2.11: Head segment of the zipped apo state after stage tilting.	35
Figure 2.12: Head segment of the bridged apo state after stage tilting.	36
Figure 2.13: High resolution cryo-EM maps of the apo state.....	37
Figure 2.14: Comparison of the bridged and zipped apo states.	38
Figure 2.15: Heterogeneity of condensin particles upon addition of ATP.....	40
Figure 2.16: Processing workflow of the +ATP datasets after stage tilting.....	41
Figure 2.17: Arm segment of condensin in presence of ATP..	43
Figure 2.18: Head segment of <i>Sc</i> condensin in presence of ATP.....	46
Figure 2.19: Comparison of the condensin head segment in presence and absence of ATP.....	46
Figure 2.20: Physiological relevance of the Smc2-Ycg1 interface.....	47
Figure 2.21: <i>In vivo</i> crosslinking of Smc2 and Ycg1.....	48
Figure 2.22: Steric clashes between the apo and the +ATP states.....	49
Figure 2.23: Binding of Ycg1 and Ycs4 is mutually exclusive.....	51
Figure 2.24: Crosslinking mass spectrometry of the condensin holo complex.	53
Figure 3.1: Head conformations in SMC complexes..	59
Figure 3.2: DNA in SMC and SMC-like complexes.	63
Figure 3.3: Model for the condensin reaction cycle.....	65

7.3 List of Tables

Table 1: Software	68
Table 2: <i>E. coli</i> strains	69
Table 3: <i>S. cerevisiae</i> strains	69
Table 4: <i>E. coli</i> and <i>Sf21</i> expression plasmids	71
Table 5: Primary and secondary antibodies	72

8. Acknowledgements

I would like to thank Christian Haering for believing in a biologist with zebrafish fin development background to solve the structure of condensin. While challenging in the beginning, I learned to greatly appreciate the freedom of developing and following my own ideas.

I would also like to thank my TAC members Martin Beck, Sylvia Erhardt and Alba Diz-Muñoz for their guidance and support as well as my defense committee members Sylvia Erhardt, Alba Diz-Muñoz, Frauke Melchior and Sebastian Eustermann.

I am grateful for a smoothly running EM pipeline maintained by Wim Hagen, Felix Weiss and Thomas Hoffmann. I am fairly sure, remote support on weekends and during the night is not part of their contracts. The support was invaluable.

Further, this project would not have been possible without Martin Beck and Matteo Allegretti who introduced me to the world of cryo-EM and patiently answered countless questions. I would also like to thank Grant Jensen for investing his time to create ~17 h of impressively instructive cryo-EM lectures.

My gratitude extends to former and current members of the Haering Lab for providing not only a pleasant work environment but also valuable scientific input and hilarious conDANCING sessions. I am exceedingly thankful to Sol Bravo, Marc Kschonsak and Markus Hassler for great collaborations, many scientific and non-scientific conversations and for emotional support after a thousand failed cryo-EM grids.

During my PhD, I got to make wonderful friends at EMBL from all around the world. Together, we celebrated victories, weathered hardship, cooked delicious meals, watched movies, played board games and drank gin. I will look back to this time sentimentally and hope to stay in touch once our ways separate again. Likewise, friends from outside of EMBL, especially Thorsten Suckert, brought many joyful diversions to my life over hours of bouldering, running, discussing football (Go Pack Go) and Gloomhaven which allowed me to distance myself (1.5 m) from my project every now and then.

Zuletzt und am wichtigsten, möchte ich meinen tief empfundenen Dank meiner Familie gegenüber ausdrücken. Ohne die bedingungslose Unterstützung und das Vertrauen darauf, dass ich meinen Weg finde, wäre diese ganze Reise nicht möglich gewesen. Danke, Corinna, für deine unendliche Geduld, deine Liebe und deine gute Laune nach langen Tagen. Danke, Kjell, für dein Lachen und deine fürsorgliche Art, uns alle 2 Stunden aufzuwecken, um sicherzustellen, dass es allen gut geht.

